Joule

Article

Electro-biodiesel empowered by co-design of microorganism and electrocatalysis

Graphical abstract

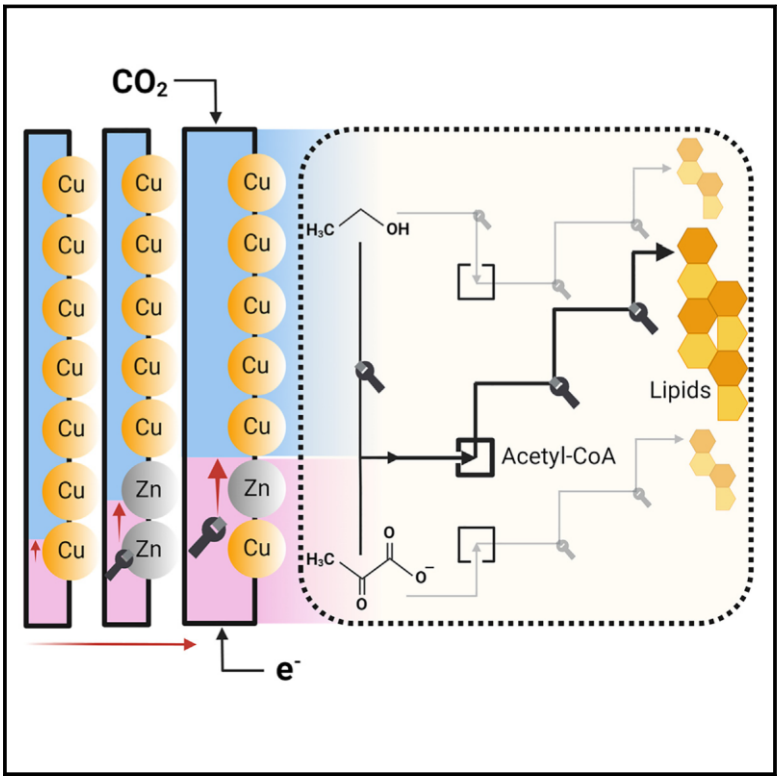

Highlights

- Electro-biodiesel with 4.5% solar-to-molecule energy efficiency and 1/45 biodiesel land use
- Co-design of microbes and catalysts to improve electron-tomolecule efficiency from CO_2
- Discover and overcome metabolic and bioenergetic limits of C2 intermediates bioconversion
- Electro-biodiesel platform with competitive economics and substantial carbon reduction

January 15, 2025 ª 2024 Published by Elsevier Inc.
https://doi.org/10.1016/j.joule.2024.10.001

Authors

Kainan Chen, Peng Zhang, Yayun Chen, ..., Sisi Xiang, Susie Y. Dai, Joshua S. Yuan

Correspondence

sydai@exchange.tamu.edu (S.Y.D.), joshua.yuan@wustl.edu (J.S.Y.)

In brief

A new electro-biodiesel concept was demonstrated by integrating electrocatalytic CO_2 reduction reaction (CO_2RR) and bioconversion through biocompatible C2+ intermediates. We have achieved high efficiency through understanding and overcoming the bioenergetic and metabolic limits for microbial bioconversion of C2 intermediates and capitalizing on the cosubstrate effects through the co-design of catalysts and microbes. The new route achieves 4.3% solar-to-fuel efficiency for the conversion of CO_2-to-fatty acid methyl esters, which is 45 times higher than that of current biodiesel.

Please cite this article in press as: Chen et al., Electro-biodiesel empowered by co-design of microorganism and electrocatalysis, Joule (2024), https://doi.org/10.1016/j.joule.2024.10.001

Joule

CellPress

CellPress

Article

Electro-biodiesel empowered by co-design of microorganism and electrocatalysis

Kainan Chen,[1,5,6] Peng Zhang,[1,6] Yayun Chen,[2,3] Chengcheng Fei,[2,3] Jiali Yu,[1,3] Jiahong Zhou,[1] Yuanhao Liang,[1,3] Weiwei Li,[5] Sisi Xiang,[4] Susie Y. Dai,[1,3,*] and Joshua S. Yuan[1,5,7,*]

[1]Synthetic and Systems Biology Innovation Hub and Department of Plant Pathology and Microbiology, Texas A&M University, College Station, TX 77843, USA

[2]Department of Agricultural Economics, Texas A&M University, College Station, TX 77843, USA

[3]Carbon Utilization Redesign through Biomanufacturing-Empowered Decarbonization (CURB) Engineering Research Center, Texas A&M University, College Station, TX 77845, USA

[4]Department of Materials Science and Engineering, Texas A&M University, College Station, TX 77840, USA

[5]Carbon Utilization Redesign through Biomanufacturing-Empowered Decarbonization (CURB) Engineering Research Center and Department of Energy, Environmental, and Chemical Engineering, McKelvey School of Engineering, Washington University in St. Louis, St. Louis, MO 63130-4899, USA

[6]These authors contributed equally

[7]Lead contact

*Correspondence: sydai@exchange.tamu.edu (S.Y.D.), joshua.yuan@wustl.edu (J.S.Y.) https://doi.org/10.1016/j.joule.2024.10.001

CONTEXT&SCALE Long-range heavy-duty vehicles and industries such as mining, shipping, and construction heavily rely on energy-dense diesel fuels, which cannot be defossilized by electric vehicles. Biofuels can fill the gap, yet biodiesel productivity is limited by low photosynthesis efficiency. It is unrealistic to defossilize diesel consumption by a large percentage with biodiesel, considering the substantial land usage. Similarly, the fundamental limit in human civilization lies in the efficient utilization of renewable energy to produce sufficient fuels, chemicals, materials, and food with limited natural resources. Herein, we developed a new electro-biodiesel concept to manufacture diesel from CO_2 by integrating electrocatalytic CO_2 reduction reaction (CO_2RR) to produce biocompatible C2+ intermediates, with subsequent microbial conversion of these intermediates into lipids as biodiesel feedstock. This new concept can be broadly applied to the circular economy for manufacturing emission-negative fuels, chemicals, materials, and food ingredients at a much higher efficiency than photosynthesis and lower carbon emissions than petrochemicals. We have systemically addressed the challenges in electro-biomanufacturing by identifying the metabolic and biochemical limits of C2 utilization and overcame these limits by balancing the reducing equivalent and enhancing ATP production. Furthermore, we have revealed co-substrate effects for ethanol and acetate and designed catalysts to produce an optimal ratio of acetate and ethanol to achieve higher bioconversion efficiency. The synergistic microbial and catalyst design empowered electro-biodiesel to achieve 4.5% solar-to-molecule efficiency for converting CO_2 into lipid, which is much more efficient than biodiesel and other competing platforms. Techno-economic and life cycle analyses revealed competitive minimal selling prices, substantial carbon emissions, and substantially less land use compared with current biodiesels. The electro-bioconversion of CO_2 could alleviate the biodiesel feedstock shortage and transform the renewable fuel industry. The new concept can be broadly applied to chemical, material, and fuel manufacturing to create a circular carbon economy for mitigating global climate change.

SUMMARY

Efficient and sustainable energy production is essential for climate change mitigation, yet current approaches like biofuels or electro-fuels have limitations in efficiency and product profile. We advanced a new electro-biodiesel route via integrating electrocatalysis and bioconversion to produce lipids from CO_2 for biodiesel. We first revealed bioenergetic and metabolic limits in C2+ intermediate utilization through simulations and metabolomics, guiding the synthetic biology

design to achieve reductant balance, more ATP production, efficient lipid conversion, and higher lipid yield. Furthermore, we discovered specific ratios of

Joule 9, 1–16, January 15, 2025 ª 2024 Published by Elsevier Inc.

ethanol and acetate to achieve co-substrate synergy, empowering bimetallic catalyst design to improve bioconversion efficiency. The microbial and catalyst co-design achieved a solar-energy-to-molecule conversion efficiency of 4.5% for CO_2-to-lipid conversion. Electro-biodiesel leverages the high efficiency of electrocatalysis and longer-carbon-chain products from microbial lipid synthesis, overcoming the limitations for both electrocatalysis and bioconversion. Electro-biodiesel achieved 45 times less land usage than soybean biodiesel, competitive economics, and substantial carbon emission reduction.

INTRODUCTION

Most fuels are generated from sunlight by photosynthesis, either by directly converting plant products from CO_2 (e.g., soybean biodiesel and corn ethanol) or by processing the petroleum generated from photosynthesis millions of years ago (e.g., fossil fuels). The fundamental limits of human civilization lie in the energy-efficient CO_2 conversion into sufficient chemicals, fuels, materials, and food to achieve fossil-fuel independence. In particular, it is critical to advance new routes to convert CO_2 into long-range heavy-duty vehicle fuels and aviation fuels, as both are challenging to defossilize with electric vehicles.[1] However, the current platforms all have their limitations.

Biodiesel has been explored as an alternative to fossil diesel. Biofuel production can effectively harness complex biological pathways to produce diverse chemicals for different types of fuels, including longer-carbon-chain products like lipids for diesel (Figure 1). However, the overall solar-to-chemical energy conversion efficiency of biofuels remains constrained by photosynthesis efficiency (Figure 1).[2] Photosynthesis efficiency is typically limited to around 1% in terrestrial plants, which makes it impossible to fulfill the transportation needs with biofuels on limited arable lands.[3] To fulfill the current US diesel demand of 3.7 million barrels with soybean biodiesel, it will need 747 million acres of arable land, accounting for two times the US arable land and 37% of the total land area of the continental 48 states of the US (Table S1). While algal biodiesel has been proposed as an alternative with better land-use efficiency, algal biofuel faces commercialization challenges due to the inherent limitation on light penetration and harvesting cost.[4] Energy-efficient pathways need to be developed to substantially surpass the photosynthesis energy conversion efficiency for the production of renewable diesel and aviation fuels.

Considering the biofuel limitations, electro-fuels and solar fuels have been proposed as alternative approaches. However, electrocatalysis and photocatalysis have inherent limits in producing longer-carbon-chain products, hindering the direct production of sustainable aviation and diesel fuels.[5,6] Electrocatalysis has achieved high efficiency in CO_2 reduction reactions (CO_2RRs) to produce C1 products like CO, formate, and methanol.[7–9] Recent advancements have substantially improved Faradaic efficiency for CO_2RR to C2 products like ethanol, acetate, and ethylene and even C4 products like butanol.[10–14] However, achieving high catalyst selectivity, product yield, and titer for longer-carbon-chain products relevant to the diesel and aviation fuel series remains challenging.[5]

Here, we present an electro-biodiesel approach to efficiently produce the biodiesel precursor, lipids, from CO_2, leveraging the integration of electrocatalysis and bioconversion and overcoming all aforementioned challenges (Figure 1). Electro-biodiesel combines the high efficiency and conversion rate of electrocatalysis and the diverse product profile of microbial conversion.[15] Previous work has explored the possibility of integrating electrocatalytic CO_2RR with downstream bioconversion using C1 intermediates (formate, methanol, CO, and such).[16] However, the C1 intermediates (formate and methanol) and gas intermediates (CO and hydrogen) have limited microorganism selection for downstream bioconversion. It causes cell toxicity in many microbial species, needs multiple steps to enter primary metabolism, and often has gas-to-liquid transfer limitations, all of which translate to low conversion efficiency, rate, and titer. Recent breakthroughs leveraged advancements in electrocatalysis to generate C2+ intermediates for bioconversion, overcoming the challenges of inefficient intermediates for chem-bio interfacing and achieving the record productivity of bioplastics.[15]

Despite the progress, a substantial fundamental understanding of bioenergetic and metabolic limits is needed to achieve efficient conversion of CO_2 into broader products, including lipids. First, can C2 compounds fulfill the energy and carbon requirements for lipid biosynthesis? Second, what are the moleculand systems-level metabolic responses of microorganisms to these C2 compounds? Especially, are there any metabolic repressions and bioenergetic limits associated with their utilization? Third, is there a co-substrate effect of ethanol and acetate that enables more efficient lipid production? In this study, we conducted a comparative modeling simulation and systems biology analysis of a model oleaginous bacterium R. jostii RHA1 to reveal the bioenergetic, metabolic, and biochemical limits for bioconversion of C2 intermediates to lipids. The fundamental understanding guided microbial design to overcome these limitations and leverage our previously discovered pivotal fatty acid synthase I (FASI) mechanism to achieve rapid lipid conversion.[17] Using the designed strain, we also discovered new cosubstrate synergy, guiding the co-design of microorganisms and catalysts to achieve an even more efficient conversion of intermediates into lipids. This co-design approach enabled the electro-biodiesel system to achieve superior lipid productivity and energy conversion efficiency compared with prior studies.

RESULTS AND DISCUSSION

Please cite this article in press as: Chen et al., Electro-biodiesel empowered by co-design of microorganism and electrocatalysis, Joule (2024), https://doi.org/10.1016/j.joule.2024.10.001

Metabolic responses to C2 intermediates during microbial lipid biosynthesis indicate potential bioenergetic and metabolic limits

To evaluate the potential of C2 intermediates for supporting lipid biosynthesis, theoretical yields of fatty acid (FA) synthesis from different C2 intermediates were calculated based on their energy

Please cite this article in press as: Chen et al., Electro-biodiesel empowered by co-design of microorganism and electrocatalysis, Joule (2024), https://doi.org/10.1016/j.joule.2024.10.001

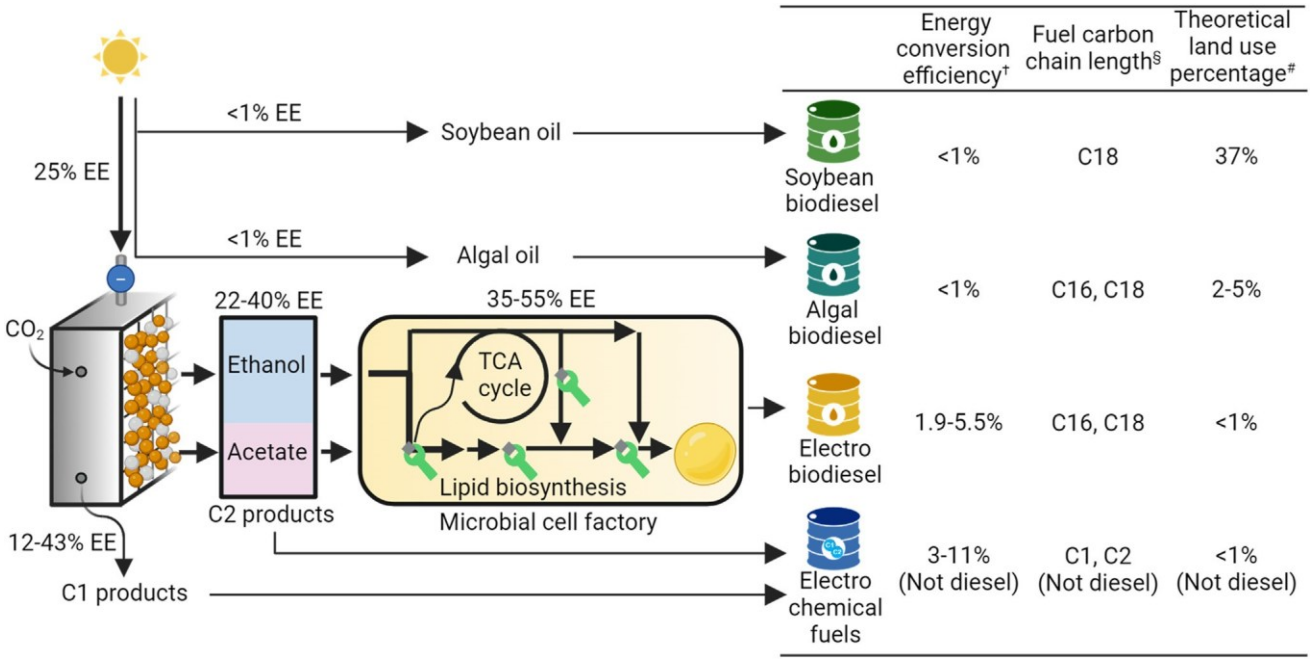

Figure 1. The schematic of routes to produce different types of diesel and fuels, with the comparisons in energy conversion efficiency, fuel carbon chain length, and land use

The arrows indicate the energy conversion direction. The values along the arrows represent the energy conversion efficiency (EE), which is referenced from literature (see supplemental information). ʸ The values are based on calculation by multiplying the efficiencies of each individual stage of the energy conversion processes. ˣ The indicators refer to the carbon chain length of the primary fatty acids comprising different fuels. # The values denote the land area required to sustain the annual total diesel consumption in the USA using these fuel types (Table S1). Illustration is created with BioRender.com.

contents as 0.62 g FA/g ethanol, 0.29 g FA/g acetate, and 0.37 g FA/g glucose, respectively (Figure S1).[18] This calculation shows that the energy content of C2 intermediates could sustain a comparable FA yield to that of glucose, particularly ethanol carrying high energy and more electrons. Nevertheless, microbial FA synthesis not just depends on substrate energy content but is also impacted by substrate metabolism. We, therefore, carried out genome-scale metabolic (GSM) modeling to evaluate the potential FA yield in an ideal microbial metabolic process.

Rhodoccocci are known engineerable oleaginous microbial species that produce high lipid content under stress conditions from diverse substrates.[17,19–21] We first carried out an experimental evaluation of multiple oleaginous species and strains for their capacity to grow in C2 intermediates. R. jostii RHA1 has shown superior performance when growing on both acetate and ethanol substrates, as compared with R. opacus PD630 and DSM1069 (Figure S2). To investigate the bioenergetic and metabolic capacity of FA synthesis from C2 intermediates in R. jostii, we constructed a draft GSM model based on the KBase platform to evaluate the utilization of ethanol or acetate as the sole carbon source (Tables S2 and S3).[22,23] Results of the flux balance analysis (FBA) show that ethanol supports a higher FA biosynthesis yield than acetate, which is consistent with the theoretical FA yield calculation (Figures 2A and S1). These results could be established from simulated metabolism (Figure 2B; Tables S4 and S5). First, ethanol assimilation does not consume a significant amount of ATP like acetate assimilation (rxn00225).[24] Correspondingly, metabolism simulation with ethanol exhibits lower energy metabolism including ATP synthesis, tricarboxylic acid (TCA) cycle, and CO_2 release in the simulation (Figure 2B). This represents a significant advantage over acetate as a substrate because low energy metabolism can reduce the diversion of carbon flux away from FA biosynthesis, as shown in the simulation.[25] Second, ethanol assimilation generates NADH, which can power NADPH generation, and other cellular activities. Specifically, the GSM simulation shows a higher pentose phosphate (PP) pathway and glyoxylate cycle (rxn01280 and rxn01281 in Table S5; Figure 2B) in the ethanol substrate than those in acetate, resulting in more NADPH to drive FA biosynthesis in Rhodococcus[26] (rxn10954 in Table S5). Overall, the GSM simulation reveals that ethanol could be bioenergetically and metabolically more efficient in supporting FA synthesis than acetate in an optimal metabolic scenario. However, the GSM model includes 56 gap-filling reactions[23] and could misrepresent the C2 intermediate metabolism in the RHA1 strain (Table S3). To validate the modeling outcome, we carried out the experimental analysis of lipid synthesis from C2 intermediates.

The experimental validation revealed surprising contradictory results to modeling. Specifically, the cell growth, lipid accumulation, and substrate consumption of RHA1 in ethanol are all significantly lower than those in acetate (Figure S3). In particular, the actual FA accumulation rate in ethanol is calculated to be merely 3.60 ± 0.02 mg/gDCW/h, significantly lower than the rate of 4.46 ± 0.17 mg/gDCW/h in acetate, contrasting with the simulation results based on the C2 consumption rates (Figure 2C). These results indicate the presence of bioenergetic and

Please cite this article in press as: Chen et al., Electro-biodiesel empowered by co-design of microorganism and electrocatalysis, Joule (2024), https://doi.org/10.1016/j.joule.2024.10.001

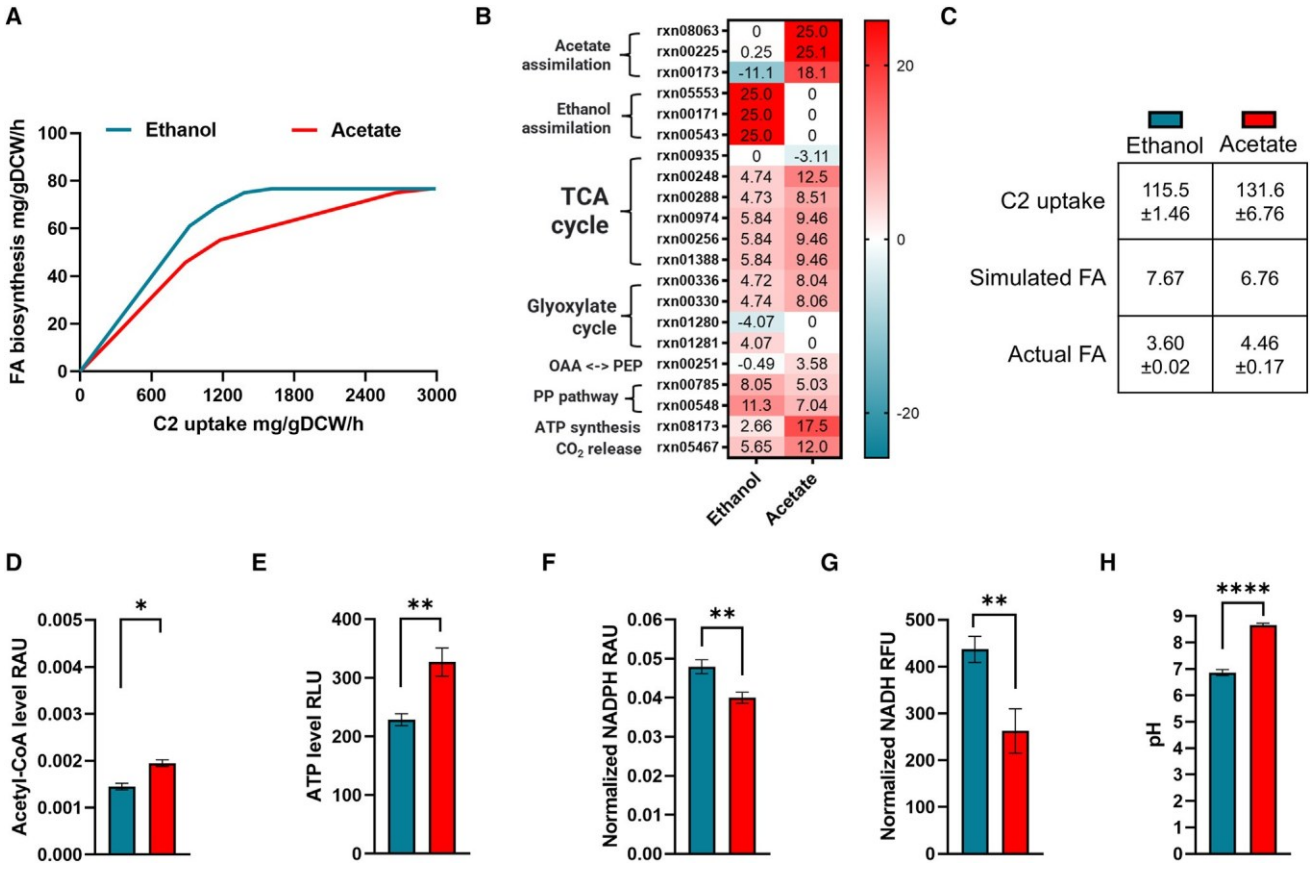

Figure 2. Computational simulation and experimental results of lipid fermentation using R. jostii RHA1 strain with ethanol or acetate as sole carbon source

(A) Stimulated FA biosynthesis fluxes of the R. jostii RHA1 GSM model under various carbon uptake rates for ethanol and acetate.

(B) Reactions that exhibit flux differences larger than 3 mmol/g DCW/h between ethanol and acetate in the FA biosynthesis simulation. The ''rxn'' stands forreaction, and the number in each well represents the magnitude of the flux of the reaction. The negative sign '''' indicates that the reaction goes in the reverse direction. A higher absolute value is masked by darker color, indicating a higher reaction flux. OAA, oxaloacetate; PEP, phosphoenolpyruvate; PP, pentose phosphate. The FBA analysis was conducted under the carbon uptake rate at 25 mmol/g DCW/h (Table S5).

(C) Comparison of experimental and simulated FA accumulation of R. jostii RHA1 strain using ethanol or acetate as sole carbon source. C2 uptake: experimental C2 uptake rate (mg/gDCW/h) = C2 consumption (mg/L)/DCW titer (g/L)/time (h); actual FA (mg/gDCW/h) = lipid content (mg/gDCW)/time (h); simulated FA: simulated FA accumulation rate (mg/gDCW/h) with experimental C2 uptakes, using the simulation curve in (A). Data used for the calculation can be found in Figure S3. The legends are shared with (D)–(F).

(D–F) Experimental lipid fermentation and physiological analysis of R. jostii RHA1 strain using ethanol or acetate as sole carbon source; (D) cellular acetyl-CoA level; (E) cellular ATP level; and (F) cellular NADPH level.

(G) Cellular NADH level.

(H) The pH of culture after fermentation; RAU means relative absorbance units, RLU means relative luminescence units, and RFU means relative fluorescenceunits. All the data were collected with biological triplicates. All the values are presented in the form of mean ± standard error of the mean. t test was used to assess the significance of difference between the two groups. The * denotes a significant difference with $p < 0.05$, ** for $p < 0.01$, *** for $p < 0.001$, and **** for $p < 0.0001$.

metabolic limits impeding the conversion of ethanol into lipids and the need for substantial engineering to realize the metabolic potential of the C2 compounds, in particular for ethanol utilization.

To identify these limits, we hence investigated the levels of substrate consumption, cellular acetyl-coenzyme A (CoA) level, ATP production, and NADH and NADPH generation, which are the critical factors to affect lipid biosynthesis.[26] First, RHA1 strain exhibits a significantly lower ethanol consumption rate at 4.74 ± 0.24 g/L than that of acetate at 8.25 ± 0.54 g/L within a 54-h period (Figure S3C). This result is consistent with the lower acetyl-CoA levels on the ethanol substrate, as compared with those on the acetate substrate (Figure 2D). The lower ethanol consumption and acetyl-CoA level suggested a limited carbon flux entering lipid biosynthesis. Second, the RHA1 cellular ATP level on the ethanol substrate was significantly lower than that on the acetate substrate (Figure 2E). This could be because the low ethanol uptake has limited the ATP production via energy metabolism.[27] Third, the levels of NADPH and NADH on the ethanol substrate are both significantly higher than those on the acetate substrate (Figures 2F and 2G). However, the imbalance between the high NAD(P)H level and the low ATP level suggested an inefficient conversion of NAD(P)H into ATP. Fourth, there is a significant decrease in culture media pH (Figure 2H), which aligns

Please cite this article in press as: Chen et al., Electro-biodiesel empowered by co-design of microorganism and electrocatalysis, Joule (2024), https://doi.org/10.1016/j.joule.2024.10.001

with the observed acetic acid secretion of RHA1 on the ethanol substrate. The result suggested that ethanol utilization could cause intracellular acidification stress. It could have impacted the cellular metabolism and lipid biosynthesis.

Metabolomics analysis revealed the need to rebalance ATP and reductant generation as well as to overcome acidification

To gain a deeper insight into the cellular metabolism related to the acetic acid accumulation and imbalance of ATP and reducing equivalents, we carried out metabolomics analysis to analyze the complex lipid species and primary metabolites from RHA1 growing on ethanol and acetate substrates. Lipidomic analysis identified 253 lipid species, revealing a significantly lower production level for 195 species under ethanol conditions, predominantly comprising triacylglycerols (TAGs) and phospholipids (Table S6; Figure S4A). These results highlighted that the lower ATP level and the lower pH of the cell may have caused impaired lipid synthesis on ethanol substrates. Metabolomic analysis reveals that out of 27 differential metabolites, 24 exhibit significantly higher levels when utilizing ethanol as the substrate (Figure 3). These upregulated metabolites included a range of amino acids, nucleotides, and carbohydrate metabolites (Figures 3 and S5; Tables S6 and S7). These results notably unveiled the systemic metabolic response of RHA1 to acidification and the imbalance of reducing equivalents associated with ethanol utilization.

First, the higher levels of amino acids and tRNA charging indicate an increased synthesis of proteins in RHA1 in response to enhance cellular acid tolerance (Figure 3).[28,29] These amino acids can also undergo decarboxylation to consume intracellular protons (e.g., serine [Ser] in Figure 3) or undergo deamination to generate NH_3^+ (e.g., glutamate in Figure 3), in order to reduce cellular acidification.[29–31] To verify the potential mechanism, we have carried out a supplementing assay with amino acids including Ser and glutamate. The Ser and glutamate supplementation both increased cell growth and pH of RHA1 culture on the ethanol substrate, supporting that the increase of amino acid could be cellular responses to acidification (Figure S6). Since they are not basic amino acids, the pH increase is not due to their dissolution but is rather due to their metabolism contributing to cell growth and acidification alleviation. Furthermore, the conversion of Ser-derived ethanolamine into diethanolamine (DEA) could also potentially generate more NH_3^+ for an acidification response, and DEA can also promote cell growth of RHA1 with the ethanol substrate as a carbon source (Figure S6). Second, despite the overall decrease levels in lipid species under ethanol conditions, there are significant activities in the synthesis and degradation of the amino lipid ceramides (Cer), indicated by the significantly high levels of Ser, D-erythro-sphingosine (Sph), DEA, and FAs (Figure 3). These corroborate the previous findings that Cer metabolism in Solibacter usitatus shifts with pH change, highlighting RHA1's cellular response to acidification stress during ethanol utilization.[32] Third, the trehalose accumulation in carbohydrate metabolism can enhance microorganisms' tolerance to acidification.[33,34] The trehalose supplementation significantly improved RHA1 growth on ethanol without changing the pH of the media, supporting that trehalose might have increased tolerance to acidification rather than alleviating it (Figure S6). Fourth, the relatively low level of pantothenic acid (VB5) together with the accumulation of b-alanine on the ethanol substrate underscores a suboptimal activity of pantoate-b-alanine ligase, which prefers an alkaline pH for the catalysis to generate VB5 (Figure 3). As the precursor of CoA, the low level of VB5 correlates with the observed low acetyl-CoA level on the ethanol substrate (Figure 2D). Supplementing VB5 thus improved RHA1 growth (Figure S6). Overall, metabolomics revealed general stress responses to combat acidification, highlighting the necessity of synthetic biology to mitigate acidification for engineering electro-biodiesel production.

Besides acidification, metabolomics analysis revealed a crucial need to balance reductant and ATP. There is a broad accumualtion of sugar alcohols, including maltotriitol, erythritol, and ribitol, that occurs from the carbonyl reduction of diverse sugar substrates, alongside squalene genration via methylerythritol phosphate (MEP) pathway (Figure 3). This carbonyl reduction and isoprenoid biosynthesis could be a strategy for RHA1 to consume excess reducing equivalents generated from ethanol assimilation. Collectively, the acidification and reducing equivalent imbalance issues of ethanol utilization cause the carbon diversion away from lipid biosynthesis to other metabolisms. Moreover, the concomitant low ATP level also needs to be addressed to drive lipid biosynthesis.[35]

Metabolic engineering to enhance lipid biosynthesis from C2

Based on the modeling and metabolomics results, we designed the synthetic biology strategy for more efficient lipid conversion from C2 intermediates. The simulation showed that ethanol carries more electrons and energy and thus could lead to more lipid generation and could enhance lipid production under a scenario where ethanol's energy is effectively utilized for lipid precursor synthesis. However, the simulation does not reflect the challenges of acidification and reducing equivalent imbalance of ethanol utilization. The comparison between the simulated and real metabolic scenarios guides our metabolic engineering strategy development. First, the simulation shows that more carbon uptake can increase FA biosynthesis (Figure 2A). However, RHA1 exhibited relatively low carbon uptake when utilizing C2 as a substrate, particularly for ethanol (Figure S3C). Second, the simulation suggests the ethanol-to-acetaldehyde-to-acetylCoA pathway as a primary pathway for ethanol assimilation, which neither costs ATP nor generates acetic acid (Figure 2B). However, in real cellular metabolism, it appears that ethanol was quickly oxidized into acetic acid and caused the acidification and reductant imbalance (Figures 2F–2H). This has prompted us to externally adjust the pH during cell culturing on the ethanol substrate to test whether it could alleviate acidification and improve lipid production. The pH adjustment significantly alleviated acidification, leading to significant improvements in cell growth and cellular ATP levels (Figures S7A and S7B). However, the effect on lipid production was limited (Figure S7A). This may be because pH adjustment did not significantly enhance carbon consumption, failing to increase carbon flux and

Please cite this article in press as: Chen et al., Electro-biodiesel empowered by co-design of microorganism and electrocatalysis, Joule (2024), https://doi.org/10.1016/j.joule.2024.10.001

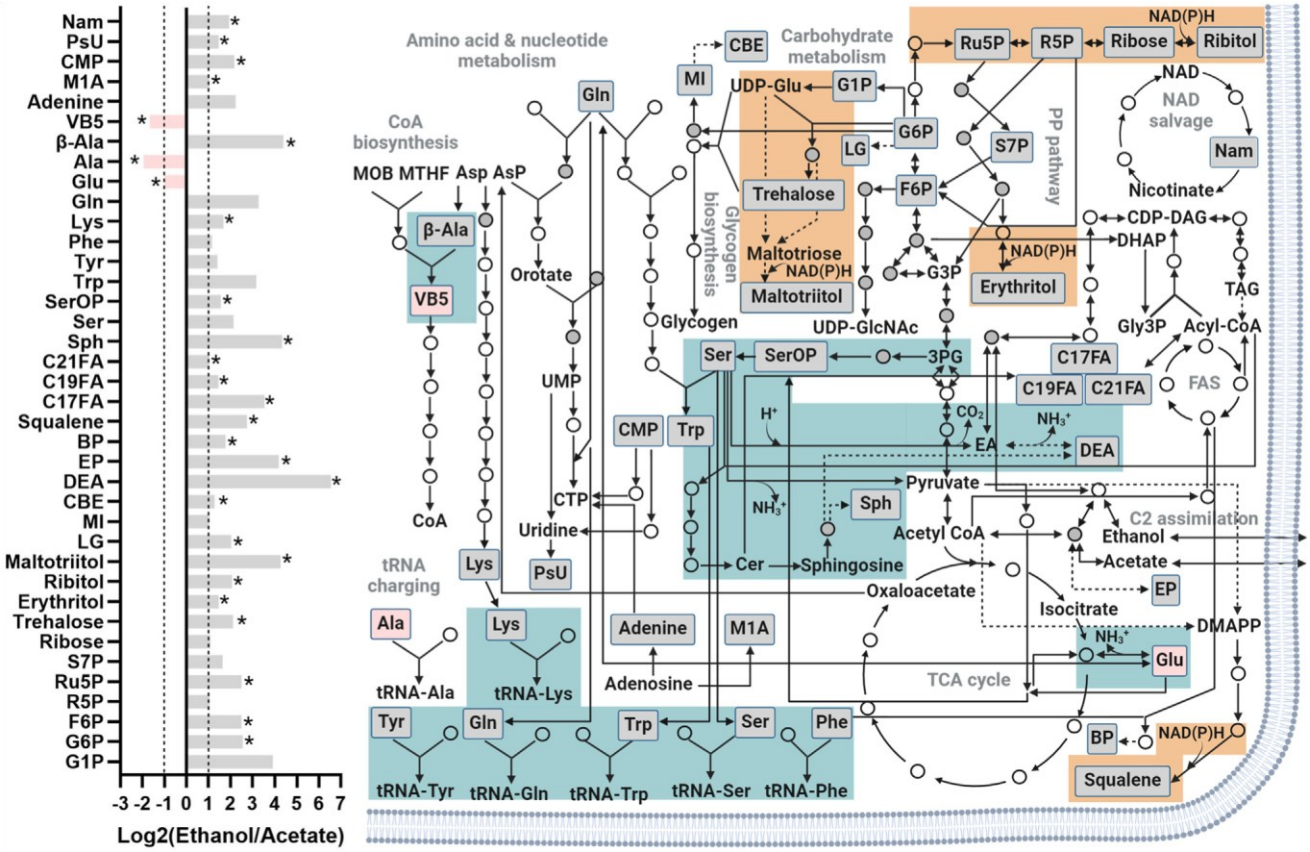

Figure 3. Visualization of the metabolic pathways based on differential primary metabolites of R. jostii RHA1 strains between the ethanol and acetate conditions

The metabolomic data were mapped onto R. jostii RHA1 genome using the pathway tools in Biocyc to get the metabolic pathways.

The intermediates in the pathways are represented as circles, where gray circles specifically indicate phosphate intermediates. Arrows indicate the metabolic reactions; dashed lines mean uncertain or simplified reactions. The reactions in green indicate potential metabolism involved in cellular acidification response, and the reactions in yellow indicate potential metabolism involved in combating reducing equivalent imbalance. G1P, glucose 1-phosphate; G6P, glucose 6-phosphate; F6P, fructose 6-phosphate; R5P, ribose 5-phosphate; Ru5P, ribulose 5-phosphate; S7P, sedoheptulose 7-phosphate; LG, levoglucosan; MI, myoinositol; CBE, conduritol-beta-epoxide; EP, ethanol phosphate; BP, biphenyl; DEA, diethanolamine; EA, ethanolamine; PEA, phosphoethanolamine; C17FA, cis10-heptadecenoic acid; C19FA, nonadecanoic acid; C21FA, behenic acid; Sph, D-erythro-sphingosine; G3P, glucose 3-phosphate; UDP-glu, uridine diphosphate glucose; UDP-GlcNAc, uridine diphosphate N-acetylglucosamine; 3PG: 3-phosphoglycerate; DHAP, dihydroxyacetone phosphate; Gly3P, glycerol 3-phosphate; CDP-DAG, cytidine diphosphate diacylglycerol; TAG, triacylglycerol; Cer, ceramides; DMAPP, dimethylallyl pyrophosphate; Ser, serine; SerOP, phosphoserine; Trp, tryptophan; Tyr, tyrosine; Phe, phenylalanine; Lys, lysine; Gln, glutamine; Glu, glutamate; Ala, alanine; Asp, aspartate; PP pathway, pentose phosphate pathway; FAS, fatty acid synthesis; TCA cycle, tricarboxylic acid cycle; VB5, pantothenic acid; M1A, 1-methyladenosine; CMP, cytidine-monophosphate; PsU, pseudouridine; Nam, nicotinamide; NAD, nicotinamide adenine dinucleotide; CTP, cytidine triphosphate; UMP, uridine monophosphate; MOB, 3-methyl-2-oxobutanoate; MTHF, 5,10-methylenetetrahydrofolate. All metabolite levels were measured in biological triplicates and normalized for comparison. Fold change analysis and unpaired two-samples Wilcoxon test were used for analysis. t test was used to assess the significance of difference between the two groups. The * denotes metabolites significantly different with $p < 0.05$.

reducing equivalents into lipid production, which highlights the necessity of metabolic engineering (Figures S7C and S7D).

We thus hypothesize that redirecting carbon from acetic acid generation to lipid biosynthesis can improve ethanol conversion into lipid. To verify the hypothesis, we overexpressed fasI operon coding FASI and atf2 gene coding diacylglycerol acyltransferase (DGAT) in RHA1 to channel more acetyl-CoA into FA and lipid biosynthesis(Figure 4A).[17] FASI is a single large, multiunit, and multifunctional enzyme complex that can conduct the condensation and elongation of FAs with high efficiency.[36] DGAT catalyzes the final step in the biosynthesis of TAGs.[17] Previous studies indicated that the co-expression of the two enzymes can lead to a significant increase in lipid productivity, whereas single gene overexpression will not achieve this effect. The overexpression of both genes significantly improved the ethanol uptake of RHA1 by 45.4% ± 12.5%, decreased the acetic acid accumulation by 63.8% ± 0.8%, and resulted in an 18.0% ± 2.3% increase in lipid accumulation (Figures 4B, 4C, and S8). Consistently, the engineered strain also showed a trend of improved lipid content when using acetate as a carbon source (Figure S9A). These results suggest that the upregulation of FASI and DGAT effectively enhanced carbon flow from C2 to

Please cite this article in press as: Chen et al., Electro-biodiesel empowered by co-design of microorganism and electrocatalysis, Joule (2024), https://doi.org/10.1016/j.joule.2024.10.001

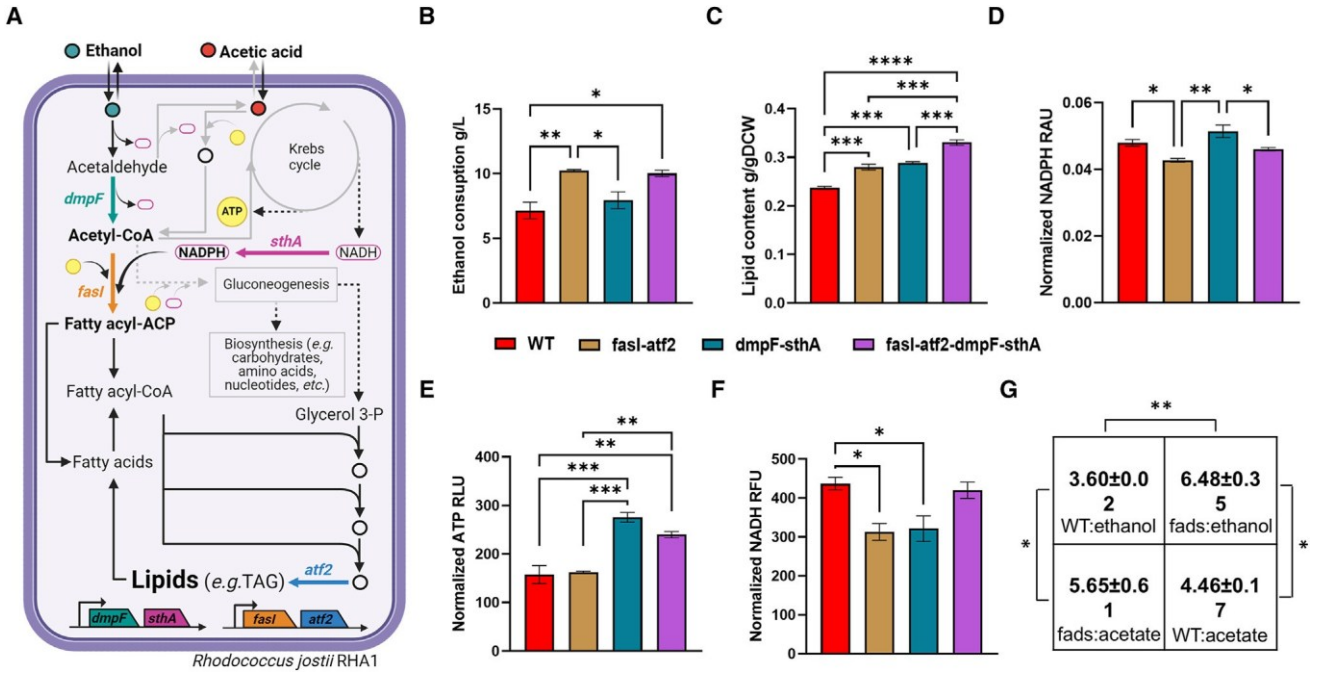

Figure 4. Genetic engineering to enhance lipid biosynthesis from ethanol in R. jostii RHA1

(A) Schematic of the lipid biosynthetic pathway from ethanol. Genes of fasI, atf2, dmpF, and sthA were overexpressed with the recombinant plasmid method. dmpF, a gene coding acetaldehyde dehydrogenase; sthA, coding soluble pyridine nucleotide transhydrogenase; fasI, coding type I fatty acid synthase; atf2, coding diacylglycerol acyltransferase. Arrows in color indicate the reactions that are upregulated by genetic manipulation. Illustration is created with BioRender.com.

(B–F) Experimental lipid fermentation results using the WT and engineering R. jostii RHA1 strains with ethanol as sole carbon source. The legends are shared.

(B) Ethanol consumption.

(C) Lipid content in DCW(D) Cellular NADPH level.

(E) Cellular ATP level.

(F) Cellular NADH level. RAU means relative absorbance units, RFU means relative fluorescence units, and RLU means relative luminescence units.

(G) The actual fatty acid (actual FA) accumulation rate-based experimental data. Actual FA (mg/gDCW/h) = lipid content (mg/gDCW)/time. WT:ethanol indicates WT strain using ethanol as sole carbon source; fads:ethanol indicates fads strain using ethanol as sole carbon source; WT:acetate indicates WT strain using acetate as sole carbon source; fads:acetate indicates fads strain using acetate as sole carbon source. Data used for the calculation can be found in Figures 5A, 5B, and S3.

Data were collected using biological triplicates, and all values are presented as mean ± standard error of the mean. Tukey's multiple comparisons test was used to assess the significance of difference between the two groups. The * denotes a significant difference with $p < 0.05$, ** for $p < 0.01$, *** for $p < 0.001$, and **** for $p < 0.0001$. Only the significant difference in mean is shown in the figure.

lipid biosynthesis. Interestingly, the fasI-atf2 strain exhibited significantly lower levels of NADPH, compared with the wildtype (WT) strain, suggesting that a higher level of NADPH is needed for FA biosynthesis (Figure 4D).[26]

We further explored strategies to balance reducing equivalents and to reduce acidification. The gene sthA coding soluble pyridine nucleotide transhydrogenase was selected to increase NADPH supply to boost lipid production (Figure 4A).[37] Simultaneously, the gene dmpF encoding the acetaldehyde dehydrogenase was overexpressed to convert acetaldehyde into acetylCoA, mitigate the acetaldehyde-to-acetic acid oxidation, and to supply NADH for sthA (Figure 4A).[38] As a result, overexpression of dmpF and sthA significantly improved the ATP level of WT RHA1 by 78.4% ± 15.9% (Figure 4E). Since the overexpression significantly mitigated the medium acidification (Figure S8A), the ATP improvement could be attributed to the less ATP cost on proton expelling for mitigating acidification stress.[31,39] The slight increase in NADPH level and significant decrease in NADH level indicate the conversion from NADH to NADPH by the transhydrogenase (sthA) (Figures 4D and 4F). Additionally, the lipid content in the dmpF-sthA strain increased by 21.6% ± 0.7%, compared with WT RHA1 (Figure 4C). These results highlighted the importance of ATP and NADPH supply for lipid biosynthesis from ethanol. Additionally, when this engineered strain uses acetate as carbon source, it also shows a significant increase in lipid content and acetate consumption, indicating that the metabolic engineering also improves acetate to lipid conversion (Figures S9A and S9B). There exists a trend of ATP level improvement, compared with the WT strain, on the acetate substrate, but the NADPH was not improved as on the ethanol substrate, likely due to the relatively low cellular NADH on the acetate substrate. The low reductant level makes it insufficient to drive the catalytic reaction of the transhydrogenase (sthA) to generate NADPH (Figures S9C–S9E). These results prompted us to consider leveraging the reducing equivalent produced from ethanol to drive the acetate conversion into lipid.

To improve NADPH and ATP supply for lipid biosynthesis in fasI-atf2 strain, we overexpressed dmpF and sthA in fasI-atf2 strain. The overexpression of dmpF and sthA improved the NADPH and ATP levels in fasI-atf2 strain by 7.8% ± 0.5% and 47.6% ± 2.0%, respectively

Please cite this article in press as: Chen et al., Electro-biodiesel empowered by co-design of microorganism and electrocatalysis, Joule (2024), https://doi.org/10.1016/j.joule.2024.10.001

(Figures 4D and 4E). Moreover, the lipid content in the fasI-atf2-dmpF-sthA (fads) strain reached 33.1% ± 0.6% in dry cell weight (DCW), which was a 39.4% ± 0.9% increase, compared with the WT strain (Figure 4C). Consistently, the lipid content reached 31.5% ± 2.1% in the fads strain when using acetate as the sole carbon source, with an increase of about 36.2% ± 1.2%, compared with the WT strain (Figure S9A). However, the NADPH and NADH levels are significantly lower than those of WT strain, indicating the insufficient energy content of acetate to effectively drive lipid biosynthesis, as compared with ethanol in the fads strain (Figures S9D and S9E). The results highlighted that reducing acidification and balancing reductant and ATP production achieved more efficient conversion of C2 compounds, especially ethanol, into lipids, verifying the metabolic capacity as revealed in the simulation.

To verify the mechanism, metabolomics analysis of the fads strain was conducted. The primary metabolism and lipid profiles in the fads strain are changed by metabolic engineering. Primary metabolites involved in carbohydrate metabolism, amino acid, and nucleoside biosynthesis were broadly decreased while levels of lipid species were increased in the fads strain under the ethanol condition, suggesting a carbon partition redirection into lipid biosynthesis by the metabolic engineering (Figures S10 and S4B). Notably, the decrease in the levels of trehalose and amino acids is consistent with the observation of mitigated acidification of fads under the ethanol condition (Figures S10 and S8). The metabolic engineering also improved lipid levels under acetate conditions (Figure S4C). Interestingly, more lipid species are observed at higher levels when sourced from ethanol, compared with acetate (Figure S4D), which is consistent with the lipid production results of this strain, showing a higher FA biosynthesis rate in ethanol than in acetate (Figure 4G). Additionally, the strain exhibited a significantly higher FA synthesis rate than the WT strain in both ethanol and acetate substrates (Figure 4G), highlighting that metabolic engineering has overcome the metabolic and bioenergetic limits and enabled RHA1 to use C2 substrates, in particular ethanol, more effectively for lipid production. Our findings highlighted that balancing the cellular levels of reductant, ATP, and pH is critical for improving biosynthesis efficiency in metabolic engineering. Further research on ^{13}C metabolic flux analysis and fine-tuning co-factor usage could help to confirm the molecular mechanisms.

Catalyst design to tune acetate/ethanol ratio to improve electro-biodiesel efficiency

Synthetic biology data indicated that sthA-dmpF design could substantially increase ATP and NADPH production (Figures 4D and 4E). The engineered strain also unleashed the metabolic potential of ethanol. Considering that ethanol carries more electrons and has a higher energy efficiency, it is probable that the reductant produced from ethanol can drive acetate conversion into lipid to increase the overall carbon conversion efficiency.

Another impact is that the co-substrate synergy could balance the acidification effect of ethanol (Figure 2H). The verification of this co-substrate effect will lead to a new strategy to improve electro-biodiesel productivity through the co-design of electrocatalysts and microbial engineering. We therefore investigate the synergetic effect on lipid production with mixed ethanol and acetate substrates at various ratios to verify the hypothesis using the fads strain (Figure 5). The results showed that with a total C2 substrate concentration of 180 mmol/L, when the acetate/ ethanol ratio reached 0.5 or higher, the acidification of culture could be significantly relieved (Figure 5A). Consequently, the lipid content and titer of the fads strain using the mixed substrates reached 0.36 ± 0.02 mg/mg DCW and 573.4 ± 32.7 mg/L, respectively, both higher than that using pure ethanol or acetate substrates (Figures 5B and 5C). Although the lipid titer of the fads strain peaked at the acetate/ethanol ratio of 1.0, there was no significant difference compared with that at the ratio of 0.5 (Figures 5B and 5C). Notably, the carbon consumption at this ratio is significantly lower than under the sole acetate condition, suggesting the co-substrate drives carbon into lipid production more efficiently (Figure 5D). This phenomenon implies that ethanol in the mixed substrate could have enhanced acetate conversion into lipids by providing reductants from its assimilation. Considering acetate assimilation requires ATP, future studies on converting ethanol-derived reductants into ATP could further enhance lipid biosynthesis from these co-substrates. Collectively, a mixed C2 with the acetate/ethanol ratio ranging from 0.5 to 1.0 supports a higher lipid production than sole ethanol or acetate. Notably, similar lipid production responses were also observed when mixed C2 substrates were used to support the growth of WT RHA1, highlighting that the co-substrate synergetic effect of ethanol and acetate could be an effective strategy to achieve higher lipid production titer (Figure S11). Our previous work has established that copper catalysts can efficiently produce ethanol as its main soluble C2 product in a biocompatible phosphate solution.[15] Based on the co-substrate effect of ethanol and acetate on the fads, we seek to tune the soluble C2 product profile from CO_2RR to facilitate C2-to-lipid conversion. The bimetallic design could improve C2+ product Faradaic efficiency in strong alkaline solutions.[40] We have adapted the principle in designing a new bimetallic catalyst for phosphate buffer. The doped secondary metal could promote the synthesis of CO from CO_2, improve the adsorption of key intermediate *CO on the surface, and could regulate the pathway of C–C coupling in C2 synthesis.[40–44] Zn was chosen as the doping metal species, considering its low toxicity to microorganisms, high selectivity toward CO, and excellent compatibility with copper species. We hence developed a series of Zn-doped Cu catalysts (Cu_xZn_y, x:y stands for the ratio between Cu and Zn; Figure 5E) to tune the ratios between acetate and ethanol generated from CO_2RR, and we used them to conduct CO_2RR in our three-chamber flow electrolyzer with phosphate electrolyte (Figure 5F).[15] The Cu_6Zn_1 bimetallic catalysts were prepared by co-sputtering Cu and Zn on the PTFE substrate with controlling the power of copper and zinc. The coexistence of Cu and Zn on the substrate was proved by X-ray photoelectron spectroscopy (Figure S12), scanning electron microscopy (SEM), and energy-dispersive X-ray spectroscopy (EDS) (Figure S13).

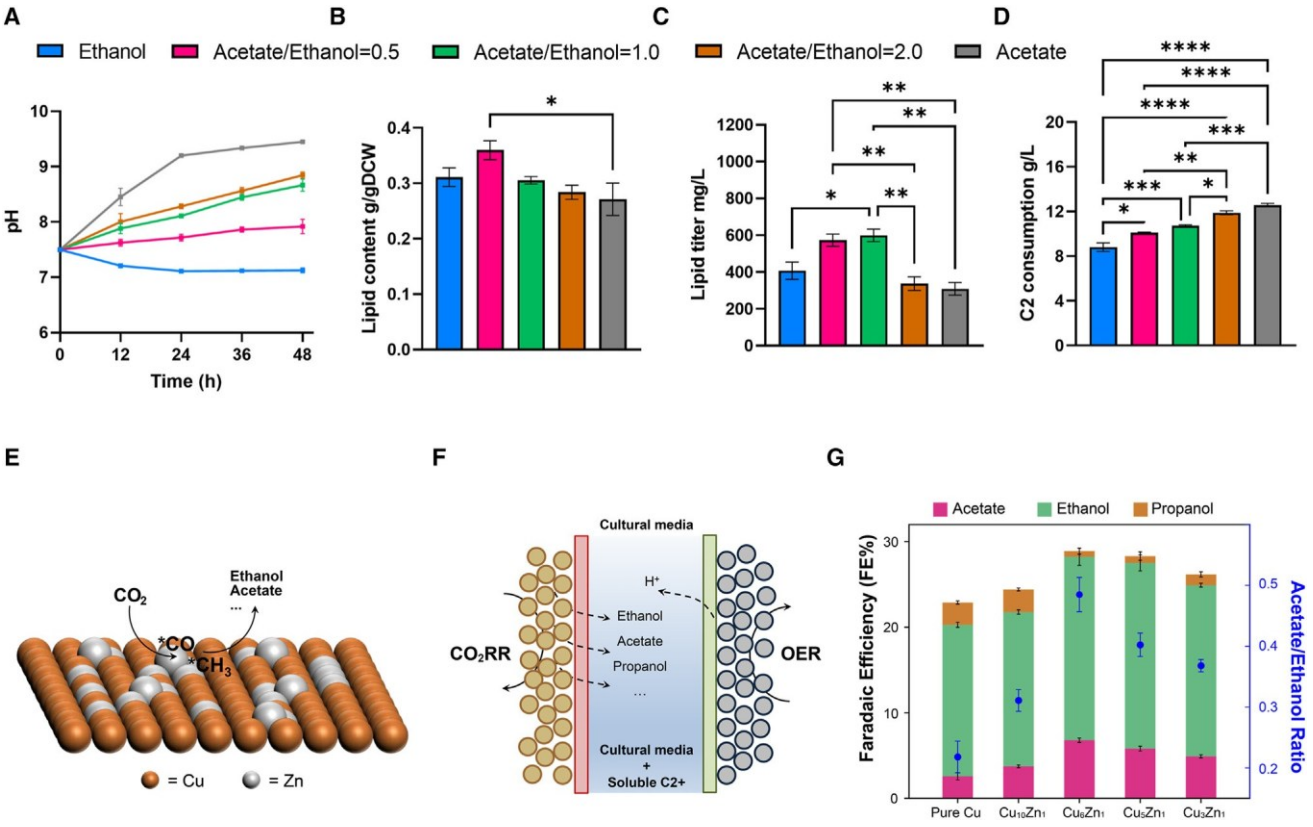

Figure 5. Bimetallic design for optimal ratio of C2 substrates in RHA1 fads lipid production

(A) The pH of the culture media.

(B–D) lipid contents (B), lipid titers (C), and C2 consumption (D) of the engineered fads strain when using ethanol, acetate, and mixed C2 as carbon sources with total concentration of 180 mmol/L. Ethanol means ethanol as used as the sole carbon source; acetate/ethanol = x denotes a mixed C2 carbon source with an x:1 mole ratio of acetate and ethanol; acetate indicates a sole acetate carbon source. The legends are shared with (B)–(D). The fads cells were prepared in LB broth to reach OD_{600} at 1.0 and then transferred into the Rhodococcus media with the C2 as the sole carbon source for lipid production (see experimental procedures). (E) Bimetallic Cu/Zn catalysts for producing ethanol and acetate as main soluble C2 products.

(F) Schematic illustration of the customized three-chamber flow electrolyzer. The microbial cultural solution was used as the electrolyte solution to elute the generated soluble C2+ products.

(G) Faradaic efficiencies of soluble C2+ products (left y axis, the bar chart with black confidence interval) and the acetate-to-ethanol ratios (right y axis, blue dot chart with confidence interval) from Cu and Cu/Zn catalysts in cultural medium. The electroreduction was conducted under a total current of 500 mA, with electrode area 4 cm^2. All data were collected using experimental triplicates, and values are presented as mean ± standard error of the mean. Tukey's multiple comparisons test was used to assess the significance of difference among the groups. The * denotes a significant difference with $p < 0.05$, ** for $p < 0.01$, *** for $p < 0.001$, and **** for $p < 0.0001$. Only the significant difference in mean is shown in the figure.

Among our Cu/Zn catalysts, the Cu_6Zn_1 achieved the highest acetate-to-ethanol ratio of 48.5% at 125 mA cm^2 (Figures 5G, S14, and S15). Notably, this ratio of zinc doping also achieved a maximum Faradaic efficiency of soluble C2+ at 28.9% ± 0.5% (Figure 5G). These results corroborate previous studies showing that introducing Zn into Cu lowers the energy barrier for C–C coupling on copper surfaces, promoting C2+ product formation.[45] Further density functional theory (DFT) calculations and in situ attenuated total reflectance Fourier transform infrared (ATR-FTIR) spectroscopy analysis would help to elucidate shifts in the C2+ generation pathway due to the co-sputtered zinc. Despite the unclear mechanism, the Zn-doped Cu catalyst design managed to generate an optimal acetate/ethanol ratio for lipid production with our fads strain. The approach is very different from previous research focusing on catalyst design to produce acetate alone, which could not deliver the ethanol/acetate ratio needed for co-substrate synergy to promote microbial conversion.[46] Additionally, the Cu_6Zn_1 catalyst maintained its performance for over 70 h (Figure S16), demonstrating excellent stability, and thus was used for integrated bioconversion.

Integrated electro-biodiesel enabling rapid and efficient CO_2-to-lipid conversion

With the successful design of the catalyst and microorganism, we managed to integrate the CO_2RR and bioconversion processes into a continuous compatible system to produce lipids from CO_2 (Figures 6A and S17).[15] The system is composed of a CO_2 electrolysis unit and a bioconversion unit. In the bioconversion unit, a two-chamber design was implemented. Part of the medium is circulated between the CO_2 electrolyzer and the

Please cite this article in press as: Chen et al., Electro-biodiesel empowered by co-design of microorganism and electrocatalysis, Joule (2024), https://doi.org/10.1016/j.joule.2024.10.001

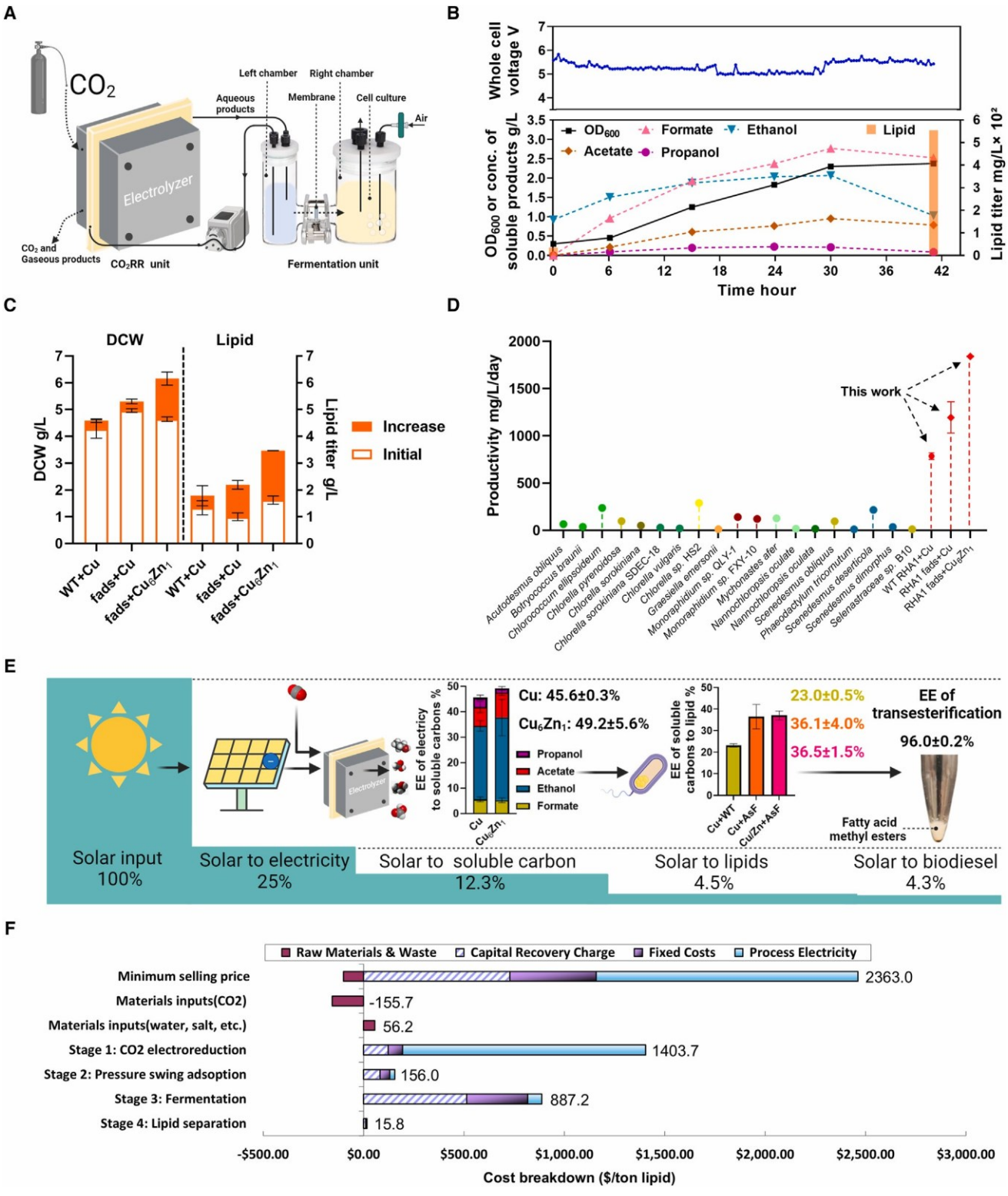

Figure 6. System integration, performance evaluation, energy efficiency estimation, and economic assessment

Please cite this article in press as: Chen et al., Electro-biodiesel empowered by co-design of microorganism and electrocatalysis, Joule (2024), https://doi.org/10.1016/j.joule.2024.10.001

(A) Schematic illustration of the integrated electro-biofuel system mainly consists of a CO_2 supplier, electrolyzer, pump, and bioreactor (asymmetric dualchamber with a 15 mL left chamber and a 45 mL of right chamber). CO_2RR products include ethanol, acetate, propanol, and formate.

(legend continued on next page)

left chamber to accumulate CO_2RR products, while the microbes are kept in the right chamber. A non-selective filter membrane was placed between the two chambers, which allows the CO_2RR products to diffuse to the right chamber, while efficiently blocking the microbes from entering the left chamber and the electrolyzer.

We first inoculated WT RHA1 into the integrated system to evaluate the biocompatibility and biomass conversion performance of the electro-biodiesel system (Figures 6A and 6B). The WT RHA1 cells in the right chamber utilized the soluble carbon sources diffused from the left chamber to support their growth and lipid biosynthesis effectively. The whole system maintained a stable C2 concentration level and rapid cell growth for 42 h. Specifically, the voltage of electrolyzer remained constant between 5 and 6 V across the time, and the concentrations of ethanol and acetate kept increasing in the first 30 h, indicating that the catalyst produced sufficient C2 substrates for RHA1 to use. A rapid RHA1 growth is observed, indicated by the optical density at 600 nm (OD_{600}) increasing from 0.3 to 2.2 (Figure 6B). Moreover, the lipid titer increased from 32.4 to 562.1 mg/L within 42 h, equivalent to a lipid productivity rate of 302.7 mg/L/day, which is comparable to the lipid productivity of high lipid-producing algae and microalgae (Figure 6D).[47–49]

To further enhance the lipid production from CO_2 in this integrated system, RHA1 strains were introduced at a relatively high cell density and with controlling of the high carbon/nitrogen ratio.[26] Different combinations of RHA1 strains and catalysts are tested in the integrated system to evaluate the lipid production (Figure 6C). First, with 4.3 ± 0.2 g/L of WT RHA1 cell density, the system equipped with Cu catalyst achieves 785.2 ± 20.1 mg/L lipid titer from CO_2 (Figure 6C). When a comparable load (4.9 ± 0.0 g/L) of fads was inoculated, the lipid titer from CO_2 increased to 1,194.8 ± 95.5 mg/L (Figure 6C), demonstrating the better C2 utilization and lipid productivity of fads in the system. When the Cu_6Zn_1 catalyst is used, the fads strain (4.6 ± 0.1 g/L cell density) increases the lipid titer to 1,840.2 ± 1.9 mg/L (Figure 6C), indicating the effectiveness of codesigning the strain and catalysts. Notably, aside from C2 substrates, formate and propanol are also present in the CO_2RR products, in which formate could be catabolized to generate reducing equivalents to drive bioconversion, and propanol serves as the carbon source to support both cell growth and lipid production of RHA1 (Figures S18 and S19). Overall, the lipid productivity of the integrated system with the Cu_6Zn_1+fads combination can produce 1,840.2 ± 1.9 mg/L/day of lipids, which is about 6-fold the highest lipid productivity achieved by algae (Chlorella sp. HS2, 289.6 mg/L/day) through photosynthesis (Figure 6D),[47–49] highlighting that the electro-biodiesel system and co-design of catalyst and microorganism can produce lipid from CO_2 faster than natural systems. Despite the progress, the research remains at a bench scale. Further scale-up of the integrated electro-biodiesel platform will help to refine the technoeconomic and life cycle implications for commercialization.

To evaluate the energy conversion efficiency of the integrated electro-biodiesel system, we decomposed the conversion into four stages: solar to electricity, electricity to soluble carbon sources,soluble carbonsources to lipid,and lipid tobiodiesel.For conversion at the first stage, we estimated the efficiency using maturing photovoltaic technology, indicating an energy efficiency of 25% (Figure 6E).[50] The energy efficiency of the second-stage electrocatalysis was calculated based on enthalpy gains for specific CO_2RR products.[51] Considering that gaseous products, such as ethylene and hydrogen, from electrocatalysis were not utilized by the bioconversion, we calculated the energy efficiency by dividing the energy content of all soluble products (energy output) by the electricity energy input used to produce these soluble products (see experimental procedures).[15,51] The Cu_6Zn_1 catalyst reached an energy efficiency of 49.2% ± 5.6% for the conversion of electricity into soluble products (Figure 6E). Third, the energy efficiency of bioconversion is calculated by dividing the energy content of the produced lipid by the

(B) The biocompatibility and stability of the integrated system demonstrated by the cell growth of WT RHA1 and the performance of the copper catalyst. The WT RHA1 was inoculated into the system to achieve rapid cell growth or biomass generation from CO_2.The blue curve in the upper box indicates the voltage of CO_2 electrocatalysis, and the curves in the lower box indicate cell growth, concentrations of carbon substrates, and lipid titer during fermentation. The lipid contents in the inoculated and harvested RHA1 cells are 0.13 g/g DCW and 0.28 g/g DCW, respectively.

(C) Lipid production of different combinations of catalysts and strains in the integrated system. RHA1 cells with a high cell density, with an OD_{600} of approximately 4 to 5, are inoculated to serve as the whole-cell catalyst for lipid production from CO_2. The WT+Cu represents a combination of copper-based catalyst and WT RHA1 strain. The fads+Cu represents a combination of copper-based catalyst and engineered strain fads. The fads+Cu_6Zn_1 represents a combination of copper/ zinc bimetallic catalyst and engineered strain fads. Cell density was indicated by dry cell weight (DCW), and lipid production was calculated by deducting the initial lipid accumulation from the final lipid titer. Data were collected using biological triplicates, and all values are presented as mean ± standard error of the mean.

(D) Comparison of lipid productivity of the electro-biofuel system with high lipid-producing algae and microalgae studies. High lipid productivity cases wereextracted from three recent reviews that focused on lipid-producing microalgae and algae to assess our electro-biofuel system. WT RHA1+Cu indicates that the integrated system operates with WT RHA1 as lipid producer and copper catalyst for CO_2RR reduction; RHA1 fads+Cu indicates the integrated system operates with fads strain as lipid producer and copper catalyst for CO_2RR reduction; RHA1 fads+Cu_6Zn_1 indicates the integrated system operates with fads strain as lipid producer and Cu_6Zn_1 catalyst for CO_2RR reduction. Data on the lipid productivity of algae were reported in high lipid productivity cases that were obtained from three recent reviews focused on lipid-producing microalgae and algae.

(E) Calculation of overall energy efficiency of the electro-biofuel system. Data were collected using biological triplicates, and all values are presented as mean ± standard error of the mean.

(F) Economic contribution of process stages to an upscaled electro-biodiesel system for lipid production at a scale of 8,000 tons/year.

Please cite this article in press as: Chen et al., Electro-biodiesel empowered by co-design of microorganism and electrocatalysis, Joule (2024), https://doi.org/10.1016/j.joule.2024.10.001

total energy of consumed soluble products, resulting in an average efficiency of 36.5% ± 1.5% for the fads strain in the integrated system (Figure 6E). Fourth, the energy efficiency of transesterification is calculated by dividing the energy content of theoretically obtained FA methyl ester by the energyof 1 kg oflipidsand the requiredmethanol, thenmultiplying by the experimentally determined reaction yield of 98.8% ± 0.5%, resulting in an efficiency of 96.0% ± 0.2% (see supplemental information). Overall, the electro-biodiesel system achieves an overall energy efficiency of 4.5% for converting CO_2 into lipids and

4.3% for converting CO_2 into biodiesel (Figure 6E). This result approaches the theoretical maximum achievable efficiency of 5.5%, which is calculated by combining the current highest energy efficiency of CO_2 electroreduction for C2 production with the highest energy efficiency observed in microbial fermentation using C2 substrates (Figure 1).

The solar-to-molecule efficiency of 4.5% by this study surpassed competitive platforms such as soybean biodiesel and algal biodiesel and exceeded the solar-to-biomass efficiency achieved in recent studies (see supplemental information). The remarkable efficiency indicates that one acre of land can theoretically yield 502,319 MJ of electro-biodiesel annually, approximately 45 times higher than soybean biodiesel and 3 times the achievable algal biodiesel energy production (Table S1; Figure 1). A major advantage of electro-biodiesel over phototrophic and mixotrophic algal cultivation is overcoming the dilemma of mutual shading at high cell density in algal cultivation.[4] Our previous study has highlighted that light penetration began to limit cell growth at OD about 2 in cyanobacteria, when mutual shading will block the light and limit the growth. However, in our electrobio integrated system, we operated at OD 4.5 to 5 to achieve high productivity and titer. Even higher productivity can be achieved when high-density cell cultivation is used. High productivity and titer are critical as they will drive better economics and efficiency. Compared with the plant- and algal-based biodiesel, where solar-to-molecule efficiency is limited by both photosynthesis efficiency and low carbon partition into energydense storage carbon for lipid production, resulting in low peracre yields, the electro-biodiesel overcomes the low efficiency, kinetics, and carbon partition through both electrocatalytic CO_2RR to produce biocompatible high energy content electron carrier and engineering of energy and reductant balance in a highly efficient oleaginous bacteria. As compared with the previous platforms focusing on acetate production from CO and CO_2,[46,52] the mechanism-driven synthetic biological engineering and unique co-design of microorganisms and catalyst empowered the optimal composition of C2 intermediates and, consequently, highly efficient conversion. In particular, the reductant and ATP from ethanol assimilation can improve the bioenergetic and metabolic efficiency of acetate conversion. The overall bioconversion efficiency for the C2 intermediate mixture to the highly reduced lipid molecule can achieve 37%. The fundamental discoveries and the engineering designs opened new avenues for substantially improving energy and carbon conversion efficiency in both microbes and the integrated electro-bio system, providing a path for efficient electron-to-molecule conversion. The high energy conversion efficiency and lipid productivity also translate into less land usage for electro-biodiesel production. Specifically, the electro-biodiesel production requires only 1/3 of the land required for algal biodiesel, 1/45 of the land required by soybean biodiesel, and 1/10 of the land required by palm biodiesel, amounting to only 0.83% of land to sustain the entire US diesel consumption (Table S1).

Environmental and economic impacts of the electrobiodiesel approach

The life cycle analysis (LCA) was conducted to evaluate the global warming impact of the electro-biodiesel approach, considering the three primary processes: electrolysis, fermentation, and lipid extraction. The functional unit, system boundaries, and inventory analysis are provided in Figure S20 and Tables S8 and S9. The electricity utilization for CO_2 electroreduction and microorganism culturing are the primary contributors to the CO_2 emissions (CO_2e) from electro-biodiesel life cycle (Figure S21). Scenario analysis further examined the climate impact of different electricity sources and by-product allocation, identifying the former as the primary factor to affect the carbon emission. By substituting conventional electricity with renewable sources, the electro-biodiesel approach could achieve a reduction of 1.57 g of CO_2 per gram of electro-biodiesels produced together with the by-products such as biomass, ethylene, and others (Figure S21; Tables S10 and S11). Both lipid and by-products are of commercial value and contribute to the emission reduction by electro-biodiesel. The results highlight the potential for electro-biodiesel to achieve negative emission, in contrast to diesel produced from petroleum fractionation (0.52 g CO_2e/g) and other biodiesel production methods, which typically have positive CO_2e ranging from 2.5 to 9.9 g CO_2e/g per gram of lipids produced (Table S12).[53]

To assess the economic performance of a scaled-up electrobiodiesel system, a techno-economic analysis (TEA) was performed utilizing the experimental data and an annual output of approximately 8,000 tons, which was used in a previous TEA analysis on a heterotrophic microbial lipid production process.[54] The results for the LCA case of renewable energy source with byproduct offset credit are integrated into the TEA (Figure S22).[55] Our base case analysis revealed a minimum lipid selling price at $2.36/kg with the current electro-biodiesel system's performance and the assumed production capacity (Figure 6F). This selling price outcompeted the previous estimate of $2.5/kg for microbial lipid production at the same annual scale, using glucose as feedstock.[54] This estimated price also demonstrates the electro-biodiesel approach's competitiveness regarding costs in relation to microalgae lipid production in both photobioreactors ($20.53/gal) and open pounds ($9.84/gal).[56] It highlighted the superior performance of the electro-biodiesel approach as compared with the traditional biorefinery-based biofuel and photosynthetic biofuel approaches.[2] The sensitivity analysis identified several key parameters that would further impact the minimum lipid selling price (Figure S22). It shows potential for electro-biodiesel prices to compete with plant oil prices, which range from $0.5 to $1.9/kg.[57]

Conclusions

We have taken a systemic approach to designing the electrobiodiesel route, identifying the fundamental limits, and improving the system

Please cite this article in press as: Chen et al., Electro-biodiesel empowered by co-design of microorganism and electrocatalysis, Joule (2024), https://doi.org/10.1016/j.joule.2024.10.001

efficiency, economics, and emission impacts. The new route leverages the high efficiency of electrocatalysis and synthesis of long-chain fuels from microorganisms. In order to achieve high system efficiency and kinetics, we first investigated the biochemical and metabolic limits for C2+ intermediate conversion and found that ethanol conversion is unexpectedly low in experimental data as compared with the modeling. We then identified the acidification stress, reducing equivalent imbalance, and low ATP production as the metabolic limits to prevent efficient ethanol conversion into lipid in a model oleaginous microorganism R. jostii RHA1. To overcome the metabolic limits, metabolic engineering was carried out to mitigate cellular acidification, balance reductant generation, and increase ATP production, all of which enhanced carbon flux to lipids using C2 intermediates. Using the engineered strain, we further explored the co-substrate synergy for acetate and ethanol, considering that ethanol conversion in the engineered strain could render more reducing equivalents and higher ATP to drive carbon conversion. The study revealed the synergistic effects and identified proper ratio for ethanol and acetate to achieve maximized lipid conversion. Based on co-substrate effect, we designed a new Zn-Cu bimetallic catalyst that efficiently produces C2 intermediates in biocompatible electrolyte at an optimal acetate/ethanol ratio for lipid synthesis in engineered RHA1 strain. The co-design of Zn-Cu catalyst and RHA1 strain enabled a highly efficient electro-microbial integrated system to achieve 1,840.2 ± 1.9 mg/L/ day lipid productivity from CO_2 with a 4.3% solar-to-fuel overall energy efficiency, significantly surpassing the photosynthesisbased biofuel production strategy. Additionally, the utilization of C2 intermediates in electro-biodiesel route imparts the versatility to allow for the incorporation of various microorganisms to achieve diverse fuel chemical production. Moreover, the electro-biodiesel can achieve substantial emission impact reduction at 1.57 g CO_2/g electro-biodiesel produced, and a market competitive price under large-scale production is US$2.36/kg lipids. This study thus establishes a highly productive, efficient, cost-friendly, and carbon-negative electro-biodiesel route that directly uses CO_2 as feedstock to fulfill all the US diesel demands with less than 1% of land. Such land usage does not have to be arable lands, which thus substantially alleviates food-energy competition and the shortage of biodiesel feedstock. The study further proves the concept for a broad platform for highly efficient conversion of renewable energy into chemicals, fuels, and materials to address the fundamental limits of human civilization.

EXPERIMENTAL PROCEDURES

Methods

Rhodococcus growth under ethanol and acetate conditions and physiological assay

A single colony of Rhodococcus strain on an LB agar plate was inoculated into a 10 mL LB medium and incubated overnight at 30C and 180 rpm. The cells were washed twice with phosphate buffered saline (PBS) and transferred to 50 mL Rhodococcus growth medium with an initial OD_{600} at about 0.26 to carry out the cell growth assay. The Rhodococcus growth medium contains (per liter of deionized water): 1.7 g KH_2PO_4, 9.8 g Na_2HPO_4, 0.1 g $MgSO_4$, 0.95 mg $FeSO_4$,$7H_2O$, 10.75 mg MgO, 2.0 mg/L $CaCO_3$, 1.2 mg $ZnSO_4$, 0.2 mg $CuSO_4$, 0.15 mg $CoSO_4$,$7H_2O$, 0.06 mg H_3BO_4, and 51.3 mL HCl.[58] 24 mmol/L $(NH4)_2SO_4$ was added for the nitrogen source supply. To investigate the potential of C2 substrates for lipid production, ethanol or acetate were added into the Rhodococcus growth medium as the sole carbon sources. Considering high concentration of ethanol or acetate can be toxic to microorganisms,[59,60] and to mimic the electro-bio system, a feeding method of 45 mmol/L ethanol or acetate per 12 h was adopted to supply carbon source. The cell culture was incubated at 30C and 200 rpm for 54 h. The OD_{600} and pH of the Rhodococcus culture were measured every 12 h to monitor the cell growth and pH change. At the endpoint of cell growth, cells were harvested from the culture by centrifugation. The cell pellets are then lyophilized for 24 h for DCW and lipid measurement (see supplemental information). The supernatant from the culture was collected for soluble CO_2RR substrate concentration measurement by ^{1}H NMR (Bruker AVANCE NEO 400) with D_2O as the solvent and DMSO as the internal standard.[15]

For lipid production, the washed R. jostii RHA1 cells were transferred into Rhodococcus growth medium with an OD_{600} about 1.0. A feeding method of 90 mmol/L ethanol or acetate per 12 h was adopted to supply carbon source with a limited 2 mmol/L $(NH4)_2SO_4$ supplementation to enhance lipid accumulation.[26] The fermentation process was carried out for 36 h followed by cell harvest and lyophilization.

As for the ATP, NAD(P)H, and acetyl-CoA assay measurement, R. jostii RHA1 cells suspended in the PBS were adjusted to the concentration with OD_{600} at about 1.0 and then inoculated into 10 mL of the Rhodococcus growth medium supplemented with 45 mmol/L ethanol or acetate and 24 mmol/L $(NH_4)_2SO_4$, at a 1% (v/v) inoculation ratio. The culture was incubated at 30C and 200 rpm. When OD_{600} reached about 0.4, the cells were sampled for ATP, NAD(P)H, and acetyl-CoA assay (see supplemental information).

GSM model and FBA

The KBase web-tool[23,61] was employed to conduct the GSM model construction and FBA analysis. Briefly, the complete genome of R. jostii RHA1 was obtained from the KBase database and was annotated by means of the rapid annotation subsystem technology (RAST) tool in the platform. The annotated genome was used to generate a draft GSM model of RHA1 with standard parameters including an in-built gap-filling algorithm in the KBase. Additionally, the customized Rhodococcus medium with either ethanol or acetate as sole carbon source was used as the media file for construction of the model, RHA1modelPos_Ethanol1Acetate1 (Table S3). The tool of Run FBA was used to predict metabolite fluxes in the metabolic model of RHA1 grown on the customized Rhodococcus medium. FA biosynthesis was set as objective function for the FBA with a series of carbon uptake rates to simulate FA production under different carbon inputs (Figures 2A and 2B). R. jostii RHA1 strain construction for improved lipid production To improve the capacity of the RHA1 to convert ethanol to lipid, three plasmids were used to genetically modify the lipid biosynthesis pathway. The Rhodococcus engineering followed a previously established protocol with some modifications.[17] The plasmids, strains, and primers used in the study are listed in Tables S13 and S14.

The first plasmid is PBSNC9031-Pben-FAS[17] for overexpression of fasI and atf2 (genes coding FASI and DGAT from Rhodococcus opacus PD630) in the RHA1 strain.

The second plasmid is PDD-120-dmpF-sthA for overexpression of dmpF (gene coding acetaldehyde hydrogenase from R. jostii RHA1) and sthA (gene coding hydrogen transferase from Escherichia coli str. K-12 sub-strain MG1655) in the strain. Specifically, dmpF and sthA were amplified by PCR from R. jostii RHA1 genomic DNA and E. coli str. K-12 sub-strain MG1655 genomic DNA, respectively. PDD120 vector was produced by PCR amplification to remove Che9c60 and Che9c61 gene fragments from the PDD120 plasmid.[62] The PDD120 vector, dmpF, and sthA containing ribosomal binding sites (RBSs) were fused by overlapping PCR to produce the PDD120-dmpFsthA plasmid (Table S13).

The third plasmid is PBSNC9031-fads. Specifically, the fused gene fragment dmpF-sthA containing the constitutive promoter and RBSs was amplified from the PDD120-dmpF-sthA plasmid via PCR and then cloned into the PBSNC9031-Pben-FAS plasmid[17] by inserting it between XbaI and MfeI restriction sites through a digestion-ligation method.

Both plasmids underwent thorough verification by undergoing full plasmid sequencing conducted by Primordium Labs in the USA. Subsequently, engineered strains were created by introducing these plasmids into the RHA1 WT strain through the electroporation method.

Cu/Zn catalyst manufacturing

Please cite this article in press as: Chen et al., Electro-biodiesel empowered by co-design of microorganism and electrocatalysis, Joule (2024), https://doi.org/10.1016/j.joule.2024.10.001

The Cu catalyst was prepared by sputtering copper onto a porous PTFE membrane (0.45 mm, Tisch Scientific) using Kurt J. Lesker PRO line PVD 75.[15] The Cu/Zn bimetallic catalysts were prepared by co-sputtering copper and zinc simultaneously. The thickness of the catalyst layer was about 200 nm by controlling the deposition time at 1,041 s. After sputter deposition, we tested the conductivity of the catalyst layer by pinning any two points on the surface using a multimeter and making sure all the values were less than 1 U. The bimetallic samples were denoted as Cu_xZn_y, where x:y represents the actual atomic ratios between Cu and Zn measured by SEM-EDS (Figure S13).

Operation of the integrated electro-biodiesel system

In the integrated EBF system operation, the electrolyzer, where the CO_2 electroreduction takes place, was connected to a customized bioreactor consisting of two chambers. A phosphate-based minimal solution (the Rhodococcus growth medium,) was used as electrolyte for CO_2RR and buffer solution for microbial processes. The left chamber (L) had a liquid loading volume of 15 mL, while the right chamber (R) had a liquid loading volume of 35 mL. The CO_2RR liquid products were circulated between the meddle chamber of the electrolyzer and left chamber of the bioreactor by a pump. The CO_2RR liquid products were allowed to diffuse through a membrane (grade 1, Whatman) from the left chamber to the right chamber, where the RHA1 cells use the CO_2RR products for bioconversion (Figures 6A and S17). The bioreactor was maintained at 30C with 200 rpm shaking and 50 mL/min air bubbling for RHA1 culturing. The detailed conditions for electrochemical CO_2 reduction can be found in the supplemental information. The copper catalyst operates at a current density of 100 mA/cm^2, while the Cu/Zn catalysts operate at a current density of 125 mA/cm^2. The RHA1 cells are grown in the integrated system in two ways. First, we inoculate WT RHA1 cells in the integrated system at a low cell density with a nitrogen rich media (24 mmol/L $(NH_4)_2SO_4$) and monitor the growth curve to demonstrate the biocompatibility and biomass conversion performance of the system (Figure 6B). Second, we introduce a relatively high cell density of RHA1 strains with a controlled high C/N ratio (2 mmol/L $(NH_4)_2SO_4$) to rapidly and efficiently produce lipid from CO_2 in the integrated system (Figures 6C–6E).

Specifically, in the first way, WT RHA1 was inoculated into the right chamber of the fermentation unit (initial OD_{600} at about 0.3, Figure 6B). The cell culture compartment was put under 300 rpm, 30C for 42 h. Cell density indicated by the OD_{600} was monitored during the whole process using SpectraMax iD5. At the endpoint of time, the cells in the right chamber were collected by centrifuge (3,000 3 g, 10 min), washed, and lyophilized to measure DCW and lipid content. The media in both chamber A and B was sampled across the 42-h process to quantify the product profiles via ^{1}H NMR (Figure 6B). The normalized concentration of the product profiles was calculated using the following formula:

$$\text{Normalized conc.}_{\text{product}} = \frac{\text{15mL} \times \text{conc.}_{\text{product}} \text{ in L} + \text{35mL} \times \text{conc.}_{\text{product}} \text{ in R}}{\text{50 mL}}$$

In the second way, WT or engineered fads was utilized as a whole-cell catalyst to convert CO_2RR products to lipid. Specifically, RHA1 cells prepared from overnight LB culturing were inoculated into the right chamber of the bioreactor with an initial OD_{600} at a range around 3.5 or 4.5 to achieve high cell density fermentation (Figures 6C and S23). The system operated for 24 h, with the lipid fermentation process carried out throughout this period, while the CO_2RR process was performed only during the first 15 h. This approach was adopted to align the CO_2RR product productivity and consumption rate, considering the relatively slow diffusion rate from the left chamber to the right chamber of the bioreactor. By performing the CO_2RR process in the initial 15 h, it allowed sufficient time for the CO_2RR products to diffuse and reach the right chamber where the microorganisms were present for bioconversion. At the beginning (0-h) and after 24 h, the cells were harvested for measuring DCW and lipid content (Figure 6C). Additionally, the media was collected at these time points to measure the concentration of CO_2RR products, which was essential for calculating the energy efficiency.

RESOURCE AVAILABILITY

Lead contact

Further information and requests for resources should be directed to the lead contact, Dr. Joshua S. Yuan (joshua.yuan@wustl.edu).

Materials availability

All chemicals were purchased from commercial resources and used as received. Strains and plasmids used in this study are available upon request.

Data and code availability

This study did not generate/analyze datasets or code.

ACKNOWLEDGMENTS

The authors would like to acknowledge the material characterization facility at Texas A&M University for the material characterization instruments and acknowledge the financial support received from Texas A&M AgriLife Research and NSF 2229160.

AUTHOR CONTRIBUTIONS

K.C., P.Z., S.Y.D., and J.S.Y. conceived the project. K.C. and Y.L. conducted biological assays and genetic engineering. P.Z. established CO_2 electroreduction system and conducted catalyst design. K.C. and J.Y. conducted metabolic modeling. K.C. and J.Z. conducted the metabolomic data analysis.
Y.C. and C.F. conducted the techno-economic analysis and life cycle analysis. W.L. and S.X. conducted catalyst characterization. K.C., P.Z., Y.C., C.F.,
S.Y.D., and J.S.Y. wrote the manuscript with critical input from all authors.

DECLARATION OF INTERESTS

The authors declare no competing interests.

DECLARATION OF GENERATIVE AI AND AI-ASSISTED TECHNOLOGIES IN THE WRITING PROCESS

During the preparation of this work the author(s) used Chat-GPT in order to improve language and readability. After using this tool/service, the author(s) reviewed and edited the content as needed and take(s) full responsibility for the content of the publication.

SUPPLEMENTAL INFORMATION

Supplemental information can be found online at https://doi.org/10.1016/j.joule.2024.10.001.

Received: May 11, 2024
Revised: August 23, 2024
Accepted: October 1, 2024
Published: October 31, 2024

REFERENCES

1. Mertens, J., Breyer, C., Arning, K., Bardow, A., Belmans, R., Dibenedetto,A., Erkman, S., Gripekoven, J., Le´ onard, G., Nizou, S., et al. (2023). Carbon capture and utilization: more than hiding CO_2 for some time. Joule 7, 442–449. https://doi.org/10.1016/j.joule.2023.01.005.
2. Zhou, Y.J., Kerkhoven, E.J., and Nielsen, J. (2018). Barriers and opportunities in bio-based production of hydrocarbons. Nat. Energy 3, 925–935. https://doi.org/10.1038/s41560-018-0197-x.
3. Blankenship, R.E., Tiede, D.M., Barber, J., Brudvig, G.W., Fleming, G.,Ghirardi, M., Gunner, M.R., Junge, W., Kramer, D.M., Melis, A., et al. (2011). Comparing

Photosynthetic and Photovoltaic Efficiencies and Recognizing the Potential for Improvement. Science 332, 805–809. https://doi.org/10.1126/science.1200165.

4. Long, B., Fischer, B., Zeng, Y., Amerigian, Z., Li, Q., Bryant, H., Li, M., Dai,S.Y., and Yuan, J.S. (2022). Machine learning-informed and synthetic biology-enabled semi-continuous algal cultivation to unleash renewable fuel productivity. Nat. Commun. 13, 541. https://doi.org/10.1038/ s41467-021-27665-y.
5. Sun, Z., Ma, T., Tao, H., Fan, Q., and Han, B. (2017). Fundamentalsand Challenges of Electrochemical CO_2 Reduction Using TwoDimensional Materials. Chem 3, 560–587. https://doi.org/10.1016/j. chempr.2017.09.009.
6. Zhang, Q., Yang, C., Guan, A., Kan, M., and Zheng, G. (2022). Photocatalytic CO_2 conversion: from C1 products to multi-carbon oxygenates. Nanoscale 14, 10268–10285. https://doi.org/10.1039/D2NR02588D.
7. Liu, M., Pang, Y., Zhang, B., De Luna, P., Voznyy, O., Xu, J., Zheng, X.,Dinh, C.T., Fan, F., Cao, C., et al. (2016). Enhanced electrocatalytic CO_2 reduction via field-induced reagent concentration. Nature 537, 382–386. https://doi.org/10.1038/nature19060.
8. Klinkova, A., De Luna, P., Dinh, C.-T., Voznyy, O., Larin, E.M., Kumacheva,E., and Sargent, E.H. (2016). Rational Design of Efficient Palladium Catalysts for Electroreduction of Carbon Dioxide to Formate. ACS Catal. 6, 8115–8120. https://doi.org/10.1021/acscatal.6b01719.
9. Zhang, G., Wang, T., Zhang, M., Li, L., Cheng, D., Zhen, S., Wang, Y., Qin,J., Zhao, Z.-J., and Gong, J. (2022). Selective CO_2 electroreduction to methanol via enhanced oxygen bonding. Nat. Commun. 13, 7768. https://doi.org/10.1038/s41467-022-35450-8.
10. Li, F., Li, Y.C., Wang, Z., Li, J., Nam, D.-H., Lum, Y., Luo, M., Wang, X., Ozden, A., Hung, S.-F., et al. (2020). Cooperative CO_2-to-ethanol conversion via enriched intermediates at molecule–metal catalyst interfaces. Nat. Catal. 3, 75–82. https://doi.org/10.1038/s41929-019-0383-7.
11. Hann, E.C., Overa, S., Harland-Dunaway, M., Narvaez, A.F., Le, D.N., Orozco-Ca´rdenas, M.L., Jiao, F., and Jinkerson, R.E. (2022). A hybrid inorganic–biological artificial photosynthesis system for energy-efficient food production. Nat. Food 3, 461–471. https://doi.org/10.1038/s43016022-00530-x.
12. Chen, X., Chen, J., Alghoraibi, N.M., Henckel, D.A., Zhang, R., Nwabara,U.O., Madsen, K.E., Kenis, P.J.A., Zimmerman, S.C., and Gewirth, A.A. (2021). Electrochemical CO_2-to-ethylene conversion on polyamine-incorporated Cu electrodes. Nat. Catal. 4, 20–27. https://doi.org/10.1038/ s41929-020-00547-0.
13. Choi, M., Bong, S., Kim, J.W., and Lee, J. (2021). Formation of 1-Butanolfrom CO_2 without *CO Dimerization on a Phosphorus-Rich Copper Cathode. ACS Energy Lett. 6, 2090–2095. https://doi.org/10.1021/acsenergylett.1c00723.
14. Cronin, S.P., Dulovic, S., Lawrence, J.A., Filsinger, K.A., Hernandez-Gonzalez, A.P., Evans, R., Stiles, J.W., Morris, J., Pelczer, I., and Bocarsly, A.B. (2023). Direct Synthesis of 1-Butanol with High Faradaic Efficiency from CO_2 Utilizing Cascade Catalysis at a Ni-Enhanced (Cr2O3)3Ga2O3 Electrocatalyst. J. Am. Chem. Soc. 145, 6762–6772. https://doi.org/10.1021/jacs.2c12251.
15. Zhang, P., Chen, K., Xu, B., Li, J., Hu, C., Yuan, J.S., and Dai, S.Y. (2022). Chem-Bio interface design for rapid conversion of CO_2 to bioplastics in an integrated system. Chem 8, 3363–3381. https://doi.org/10.1016/j. chempr.2022.09.005.
16. Li, H., Opgenorth, P.H., Wernick, D.G., Rogers, S., Wu, T.Y., Higashide,W., Malati, P., Huo, Y.X., Cho, K.M., and Liao, J.C. (2012). Integrated electromicrobial conversion of CO_2 to higher alcohols. Science 335, 1596. https://doi.org/10.1126/science.1217643.
17. Xie, S., Sun, S., Lin, F., Li, M., Pu, Y., Cheng, Y., Xu, B., Liu, Z., da CostaSousa, L., Dale, B.E., et al. (2019). Mechanism-Guided Design of Highly Efficient Protein Secretion and Lipid Conversion for Biomanufacturing and Biorefining. Adv. Sci. Adv. Sci. (Weinh) 6, 1801980. https://doi.org/ 10.1002/advs.201801980.
18. Xiao, Y., Ruan, Z., Liu, Z., Wu, S.G., Varman, A.M., Liu, Y., and Tang, Y.J.(2013). Engineering Escherichia coli to convert acetic acid to free fatty acids. Biochem. Eng. J. 76, 60–69. https://doi.org/10.1016/j.bej.2013. 04.013.
19. Round, J.W., Roccor, R., and Eltis, L.D. (2019). A biocatalyst for sustainable wax ester production: re-wiring lipid accumulation in Rhodococcus to yield high-value oleochemicals. Green Chem. 21, 6468–6482. https://doi.org/10.1039/C9GC03228B.
20. Round, J.W., Robeck, L.D., and Eltis, L.D. (2021). An Integrative Toolboxfor Synthetic Biology in Rhodococcus. ACS Synth. Biol. 10, 2383–2395. https://doi.org/10.1021/acssynbio.1c00292.
21. Liang, Y., and Yu, H. (2021). Genetic toolkits for engineering Rhodococcusspecies with versatile applications. Biotechnol. Adv. 49, 107748. https://doi.org/10.1016/j.biotechadv.2021.107748.
22. Henry, C.S., DeJongh, M., Best, A.A., Frybarger, P.M., Linsay, B., and Stevens, R.L. (2010). High-throughput generation, optimization and analysis of genome-scale metabolic models. Nat. Biotechnol. 28, 977–982. https://doi.org/10.1038/nbt.1672.
23. Arkin, A.P., Cottingham, R.W., Henry, C.S., Harris, N.L., Stevens, R.L.,Maslov, S., Dehal, P., Ware, D., Perez, F., Canon, S., et al. (2018). KBase: The United States Department of Energy Systems Biology Knowledgebase. Nat. Biotechnol. 36, 566–569. https://doi.org/10.1038/nbt.4163.
24. Sun, S., Ding, Y., Liu, M., Xian, M., and Zhao, G. (2020). Comparison of Glucose, Acetate and Ethanol as Carbon Resource for Production of Poly(3-Hydroxybutyrate) and Other Acetyl-CoA Derivatives. Front. Bioeng. Biotechnol. 8, 833. https://doi.org/10.3389/fbioe.2020.00833.
25. Miao, Y., Liu, J., Wang, X., Liu, B., Liu, W., and Tao, Y. (2022). Fatty acidfeedstocks enable a highly efficient glyoxylate-TCA cycle for high-yield production of b-alanine. mLife 1, 171–182. https://doi.org/10.1002/mlf2.12006.
26. Alvarez, H.M., Herrero, O.M., Silva, R.A., Herna´ ndez, M.A., Lanfranconi, M.P., and Villalba, M.S. (2019). Insights into the Metabolism of Oleaginous Rhodococcus spp. Appl. Environ. Microbiol. 85, e00498-00419. https://doi.org/10.1128/AEM.00498-19.
27. Mori, M., Marinari, E., and De Martino, A. (2019). A yield-cost tradeoff governs Escherichia coli's decision between fermentation and respiration in carbon-limited growth. npj Syst. Biol. Appl. 5, 16. https://doi.org/10.1038/s41540-019-0093-4.
28. De Angelis, M., Bini, L., Pallini, V., Cocconcelli, P.S., and Gobbetti, M.(2001). The acid-stress response in Lactobacillus sanfranciscensis CB1. Microbiology (Reading) 147, 1863–1873. https://doi.org/10.1099/ 00221287-147-7-1863.
29. Bearson, S., Bearson, B., and Foster, J.W. (1997). Acid stress responses inenterobacteria. FEMS Microbiol. Lett. 147, 173–180. https://doi.org/10.1111/j.1574-6968.1997.tb10238.x.
30. Wei, H., Shan, X., Wu, L., Zhang, J., Saleem, M., Yang, J., Liu, Z., andChen, X. (2023). Microbial cell membrane properties and intracellular metabolism regulate individual level microbial responses to acid stress. Soil Biol. Biochem. 177, 108883. https://doi.org/10.1016/j.soilbio.2022. 108883.
31. Lund, P., Tramonti, A., and De Biase, D. (2014). Coping with low pH: molecular strategies in neutralophilic bacteria. FEMS Microbiol. Rev. 38, 1091–1125. https://doi.org/10.1111/1574-6976.12076.
32. Halamka, T.A., Garcia, A., Evans, T.W., Schubert, S., Younkin, A., Hinrichs, K.-U., and Kopf, S. (2024). Occurrence of ceramides in the Acidobacterium Solibacter usitatus: implications for bacterial physiology and sphingolipids in soils. Front. Geochem. 2, 1400278. https://doi.org/10.3389/fgeoc.2024.1400278.
33. Yoshiyama, Y., Tanaka, K., Yoshiyama, K., Hibi, M., Ogawa, J., and Shima,J. (2015). Trehalose accumulation enhances tolerance of Saccharomyces cerevisiae to acetic acid. J. Biosci. Bioeng. 119, 172–175. https://doi.org/10.1016/j.jbiosc.2014.06.021.
34. Carvalho, A.L., Cardoso, F.S., Bohn, A., Neves, A.R., and Santos, H.(2011). Engineering Trehalose Synthesis in Lactococcus lactis for Improved Stress

Tolerance. Appl. Environ. Microbiol. 77, 4189–4199. https://doi.org/10.1128/AEM.02922-10.

35. Mu, X., Evans, T.D., and Zhang, F. (2024). ATP biosensor reveals microbialenergetic dynamics and facilitates bioproduction. Nat. Commun. 15, 5299. https://doi.org/10.1038/s41467-024-49579-1.

36. Schweizer, E., and Hofmann, J. (2004). Microbial type I fatty acid synthases (FAS): major players in a network of cellular FAS systems. Microbiol. Mol. Biol. Rev. 68, 501–517. https://doi.org/10.1128/MMBR.68.3.501-517.2004.

37. Long, C.P., Gonzalez, J.E., Feist, A.M., Palsson, B.O., and Antoniewicz,M.R. (2018). Dissecting the genetic and metabolic mechanisms of adaptation to the knockout of a major metabolic enzyme in Escherichia coli. Proc. Natl. Acad. Sci. USA 115, 222–227. https://doi.org/10.1073/ pnas.1716056115.

38. Shingler, V., Powlowski, J., and Marklund, U. (1992). Nucleotide sequenceand functional analysis of the complete phenol/3,4-dimethylphenol catabolic pathway of Pseudomonas sp. strain CF600. J. Bacteriol. 174, 711–724. https://doi.org/10.1128/jb.174.3.711-724.1992.

39. Papapetridis, I., van Dijk, M., Dobbe, A.P.A., Metz, B., Pronk, J.T., and vanMaris, A.J.A. (2016). Improving ethanol yield in acetate-reducing Saccharomyces cerevisiae by cofactor engineering of 6-phosphogluconate dehydrogenase and deletion of ALD6. Microb. Cell Fact. 15, 67. https://doi.org/ 10.1186/s12934-016-0465-z.

40. Chen, C., Yu, S., Yang, Y., Louisia, S., Roh, I., Jin, J., Chen, S., Chen, P.C., Shan, Y., and Yang, P. (2022). Exploration of the bio-analogous asymmetric C–C coupling mechanism in tandem CO_2 electroreduction. Nat. Catal. 5, 878–887. https://doi.org/10.1038/s41929-022-00844-w.

41. Zhou, Y., Che, F., Liu, M., Zou, C., Liang, Z., De Luna, P., Yuan, H., Li, J.,Wang, Z., Xie, H., et al. (2018). Dopant-induced electron localization drives CO_2 reduction to C2 hydrocarbons. Nat. Chem. 10, 974–980. https://doi. org/10.1038/s41557-018-0092-x.

42. Ren, D., Ang, B.S.-H., and Yeo, B.S. (2016). Tuning the Selectivity of Carbon Dioxide Electroreduction toward Ethanol on Oxide-Derived CuxZn Catalysts. ACS Catal. 6, 8239–8247. https://doi.org/10.1021/acscatal.6b02162.

43. Wang, P., Yang, H., Tang, C., Wu, Y., Zheng, Y., Cheng, T., Davey, K.,Huang, X., and Qiao, S.-Z. (2022). Boosting electrocatalytic CO_2-toethanol production via asymmetric C–C coupling. Nat. Commun. 13, 3754. https://doi.org/10.1038/s41467-022-31427-9.

44. Li, Y., Shan, W., Zachman, M.J., Wang, M., Hwang, S., Tabassum, H.,Yang, J., Yang, X., Karakalos, S., Feng, Z., et al. (2022). Atomically Dispersed Dual-Metal Site Catalysts for Enhanced CO_2 Reduction: Mechanistic Insight into Active Site Structures. Angew. Chem. Int. Ed. Engl. 61, e202205632. https://doi.org/10.1002/anie.202205632.

45. Jia, Y., Ding, Y., Song, T., Xu, Y., Li, Y., Duan, L., Li, F., Sun, L., and Fan, K.(2023). Dynamic Surface Reconstruction of Amphoteric Metal (Zn, Al) Doped Cu2O for Efficient Electrochemical CO_2 Reduction to C2+ Products. Adv. Sci. (Weinh) 10, e2303726. https://doi.org/10.1002/advs.202303726.

46. Zheng, T., Zhang, M., Wu, L., Guo, S., Liu, X., Zhao, J., Xue, W., Li, J., Liu,C., Li, X., et al. (2022). Upcycling CO_2 into energy-rich long-chain compounds via electrochemical and metabolic engineering. Nat. Catal. 5, 388–396. https://doi.org/10.1038/s41929-022-00775-6.

47. Yang, Y., Ge, S., Pan, Y., Qian, W., Wang, S., Zhang, J., and Zhuang, L.-L.(2023). Screening of microalgae species and evaluation of algal-lipid stimulation strategies for biodiesel production. Sci. Total Environ. 857, 159281. https://doi.org/10.1016/j.scitotenv.2022.159281.

48. Song, X., Liu, B.-F., Kong, F., Ren, N.-Q., and Ren, H.-Y. (2022). Overviewon stress-induced strategies for enhanced microalgae lipid production: Application, mechanisms and challenges. Resour. Conserv. Recy. 183, 106355. https://doi.org/10.1016/j.resconrec.2022.106355.

49. Singh, P., Kumari, S., Guldhe, A., Misra, R., Rawat, I., and Bux, F. (2016). Trends and novel strategies for enhancing lipid accumulation and quality in microalgae. Renew. Sustain. Energy Rev. 55, 1–16. https://doi.org/10.1016/j.rser.2015.11.001.

50. Ahmad, L., Khordehgah, N., Malinauskaite, J., and Jouhara, H. (2020). Recent advances and applications of solar photovoltaics and thermal technologies. Energy 207, 118254. https://doi.org/10.1016/j.energy.2020.118254.

51. Liu, C., Colo´ n, B.C., Ziesack, M., Silver, P.A., and Nocera, D.G. (2016). Water splitting–biosynthetic system with CO_2 reduction efficiencies exceeding photosynthesis. Science 352, 1210–1213. https://doi.org/10.1126/science.aaf5039.

52. Bi, H., Wang, K., Xu, C., Wang, M., Chen, B., Fang, Y., Tan, X., Zeng, J.,and Tan, T. (2023). Biofuel synthesis from carbon dioxide via a bio-electrocatalysis system. Chem. Catalysis. 3, 100557. https://doi.org/10.1016/j.checat.2023.100557.

53. Parsons, S., Allen, M.J., Abeln, F., McManus, M., and Chuck, C.J. (2019). Sustainability and life cycle assessment (LCA) of macroalgae-derived single cell oils. J. Clean. Prod. 232, 1272–1281. https://doi.org/10.1016/j.jclepro.2019.05.315.

54. Bonatsos, N., Marazioti, C., Moutousidi, E., Anagnostou, A., Koutinas, A.,and Kookos, I.K. (2020). Techno-economic analysis and life cycle assessment of heterotrophic yeast-derived single cell oil production process. Fuel 264, 116839. https://doi.org/10.1016/j.fuel.2019.116839.

55. Shin, H., Hansen, K.U., and Jiao, F. (2021). Techno-economic assessmentof low-temperature carbon dioxide electrolysis. Nat. Sustain. 4, 911–919. https://doi.org/10.1038/s41893-021-00739-x.

56. Davis, R., Aden, A., and Pienkos, P.T. (2011). Techno-economic analysisof autotrophic microalgae for fuel production. Appl. Energy 88, 3524– 3531. https://doi.org/10.1016/j.apenergy.2011.04.018.

57. Karamerou, E.E., Parsons, S., McManus, M.C., and Chuck, C.J. (2021). Using techno-economic modelling to determine the minimum cost possible for a microbial palm oil substitute. Biotechnol. Biofuels 14, 57. https://doi.org/10.1186/s13068-021-01911-3.

58. Seto, M., Kimbara, K., Shimura, M., Hatta, T., Fukuda, M., and Yano, K.(1995). A Novel Transformation of Polychlorinated Biphenyls by Rhodococcus sp. Strain RHA1. Appl. Environ. Microbiol. 61, 3353–3358. https://doi.org/10.1128/aem.61.9.3353-3358.1995.

59. Trcek, J., Mira, N.P., and Jarboe, L.R. (2015). Adaptation and tolerance of bacteria against acetic acid. Appl. Microbiol. Biotechnol. 99, 6215–6229. https://doi.org/10.1007/s00253-015-6762-3.

60. Ingram, L.O. (1990). Ethanol Tolerance in Bacteria. Crit. Rev. Biotechnol. 9, 305–319. https://doi.org/10.3109/07388558909036741.

61. Allen, B.H., Gupta, N., Edirisinghe, J.N., Faria, J.P., and Henry, C.S. (2022). Microbial Systems Biology: Methods and Protocols, A. Navid, ed. (Springer), pp. 291–320.

62. DeLorenzo, D.M., Rottinghaus, A.G., Henson, W.R., and Moon, T.S.(2018). Molecular Toolkit for Gene Expression Control and Genome Modification in Rhodococcus opacus PD630. ACS Synth. Biol. 7, 727–738. https://doi.org/10.1021/acssynbio.7b00416.

Joule, Volume 9

Supplemental information

Electro-biodiesel empowered by co-design of microorganism and electrocatalysis

Kainan Chen, Peng Zhang, Yayun Chen, Chengcheng Fei, Jiali Yu, Jiahong Zhou, Yuanhao Liang, Weiwei Li, Sisi Xiang, Susie Y. Dai, and Joshua S. Yuan

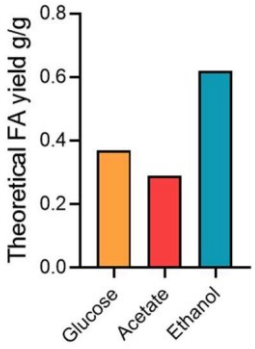

Figure S1. Comparison of theoretical fatty acid yields from ethanol, acetate and glucose as sole carbo source
The previously reported calculation method, which is based on the stoichiometry of glycolysis, ethanol and acetate metabolism, tricarboxylic acid cycle and fatty acid synthesis (8 acetyl-CoA + 7 ATP + 14 NADPH → C16 palmitic acid), was adopted to calculate the yiled.[1]

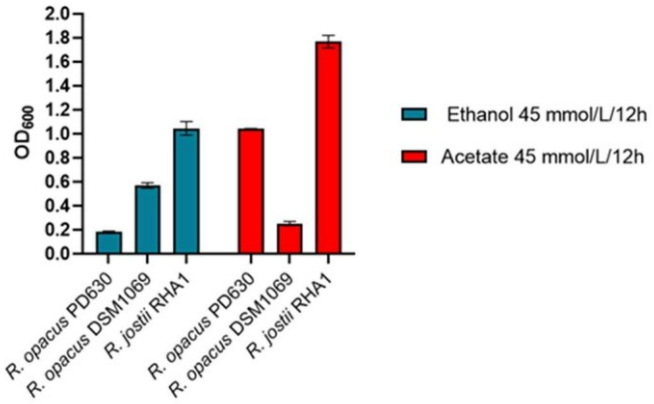

Figure S2: Comparison of cell growth among Rhodococcus species and strains
Each strain was inoculated (2% v/v) in the minimal medium supplemented with 45mmol/L ethanol or acetate as the sole carbon source per 12 hours to cultivate the growth. The OD_{600} data was collected 48 hours after inoculation using biological triplicates. All values are presented as mean ± standard error of the mean.

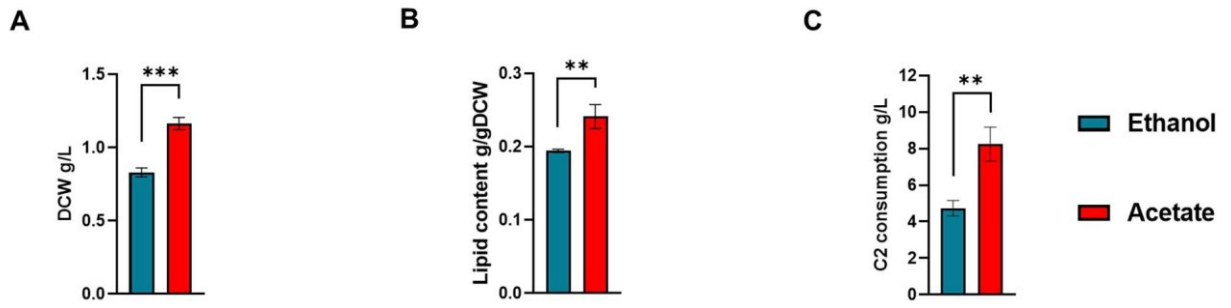

Figure S3. Experimental cell growth and lipid accumulation of R. jostii RHA1 strain with C2 substrates
The RHA1 strain was inoculated in the minimal medium with 225 mmol/L ethanol or acetate as sole carbon source in a 54-hour cell growth assay at a supplementation rate of 45 mmol/L per 12 hours. (A) DCW production; (B) Lipid content in DCW (Dry Cell Weight); (C) C2 consumption. All the data was collected with biological triplicates. All the values are presented in the form of mean ± standard error of the mean. T-test was used to assess the significance of difference between the two groups. The * denotes a significantly difference with $p < 0.05$, ** for $p < 0.01$, *** for $p < 0.001$, and **** for $p < 0.0001$.

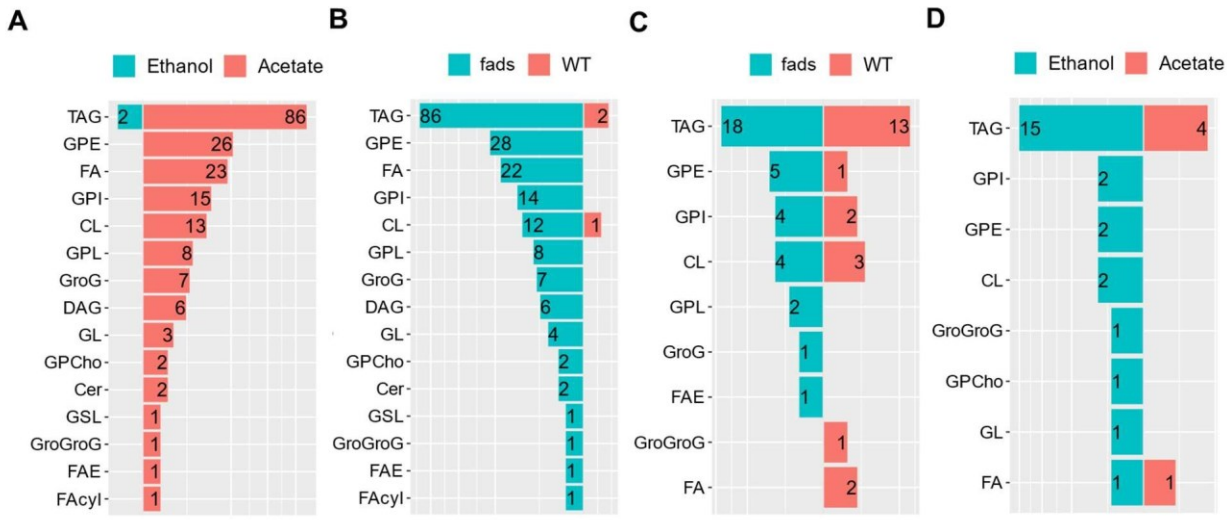

Figure S4. Visualization of the differential (t-test, $p<0.05$) lipid species of R. jostii RHA1 strains between different comparisons

Categorization and comparison of complex lipid species accumulated in R. jostii RHA1 in the conditions with ethanol or acetate as the sole carbon source (45 mmol/L per 12 hours for 54 hours). (A) comparison between ethanol and acetate conditions with WT (Wild-Type) strain (WT_ethnoal vs WT_acetate); (B) comparison between WT and fads strains under ethanol condition (fads_ethanol vs WT_ethanol); (C) comparison between WT and fads strains under acetate condition (fads_acetate vs WT_acetate); (D) comparison between ethanol and acetate conditions with fads strain (fads_ethanol vs fads_acetate). WT indicates the wild-type RHA1 strain. The fads represents fasI-atf2-dmpF-sthA strain in which genes of dmpF, sthA, fasI, and atf2 were overexpressed.

On the left side of each plot, the lipid category is indicated. The color of the bars represents different strains or conditions, and the number within each bar indicates the counts of the significantly higher lipids under that condition. TAG: triradylglycerols; FA: Fatty Acids and Conjugates; GPE: Glycerophosphoethanolamines; GPI: Glycerophosphoinositols; GroG: Glycerophosphoglycerols; DAG:

Diradylglycerols; GroGroG: Glycerophosphoglycerophosphoglycerols; FAcyl: Fatty Acyls; FAE: Fatty esters; GPCho: Glycerophosphocholines; Cer: Ceramides; GSL: Glycosphingolipids; GPL: Glycerophospholipids; GL: Glycerolipids. All the data was collected with biological triplicates.

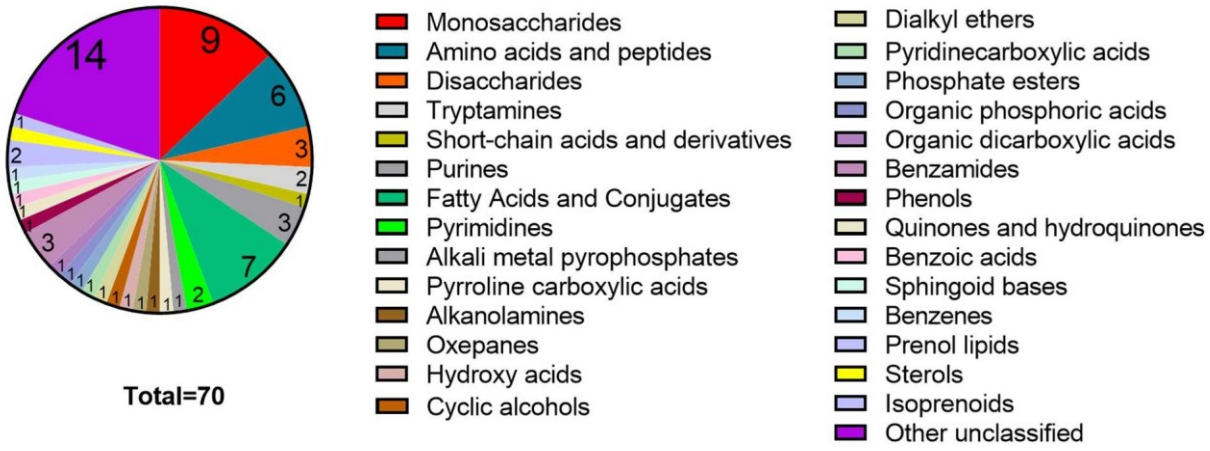

Figure S5. Categorization of the 70 primary metabolites showing significantly higher levels (fold change (FC) > 2) in the WT RHA1 cells on ethanol substrate compared to acetate substrate The 70 primary metabolites are provided in Table S7. The categorization is conducted on MetaboAnalyst 5.0.[2]

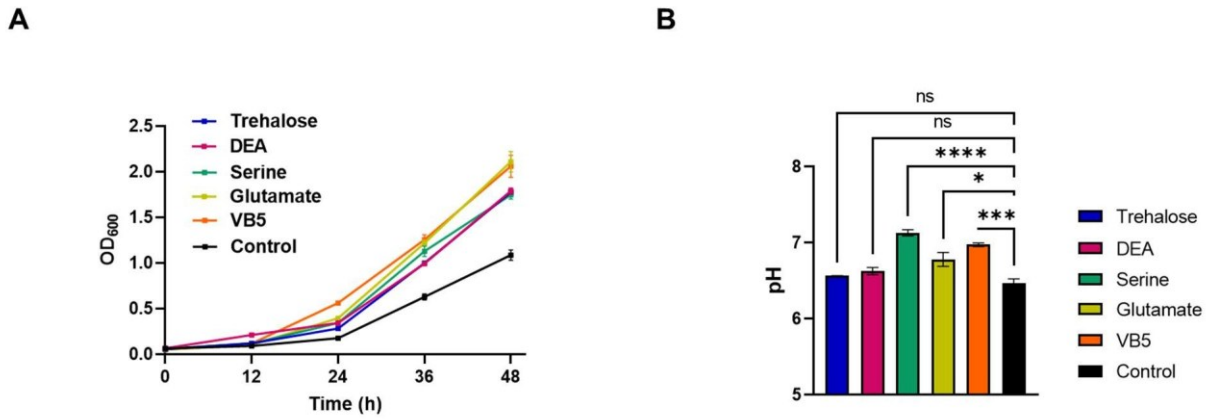

Figure S6. The impact of metabolomics-identified metabolites on cell growth and pH of WT RHA1 culture
(A) Cell growth of RHA1 on 45 mmol/L/12 h ethanol as carbon source with supplementation of different metabolites with a rate of 0.1g/L/12 h. (B) The pH of culture media after 48-hour culturing. Control indicates RHA1 cell growth without supplementation of metabolites. DEA indicates diethanolamine, VB5 indicates Vitamin B5 or pantothenic acid. The * denotes a significant difference with $p < 0.05$, ** for $p < 0.01$, *** for $p < 0.001$, and **** for $p < 0.0001$.

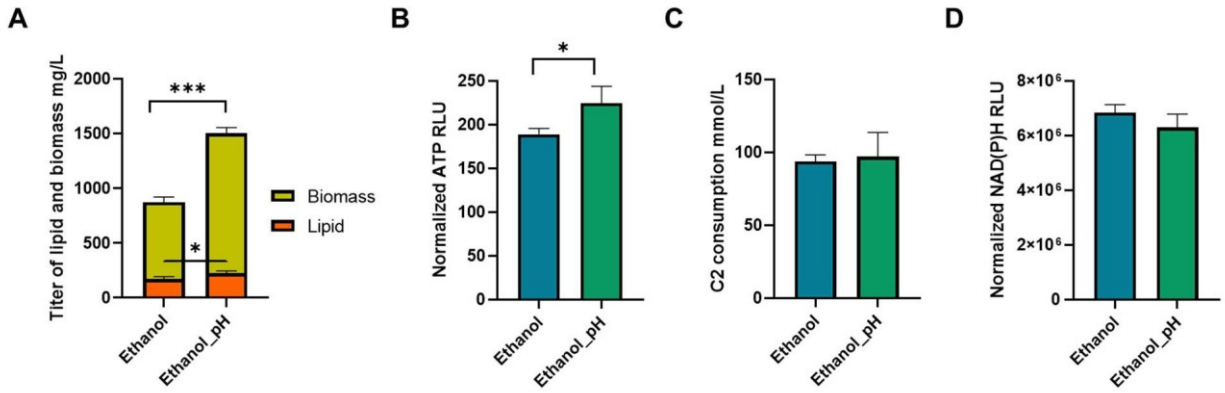

Figure S7. Cell growth, lipid production, and physiological assay of RHA1 strains on ethanol substrate with and without pH adjustment

(A) Lipid and biomass in total DCW; (B) Lipid content. (C) Cellular ATP level. (D) C2 consumption. (E) Cellular NAD(P)H level. Data was collected with biological triplicates, and all values are presented as mean ± standard error of the mean. T-test was used to assess the significance of difference between the two groups. The * denotes a significant difference with $p < 0.05$, ** for $p < 0.01$, *** for $p < 0.001$, and **** for $p < 0.0001$.

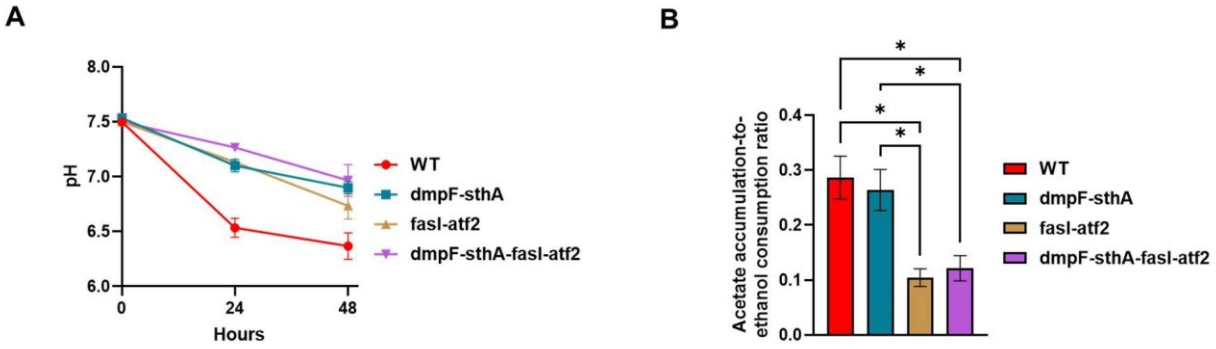

Figure S8. The pH changes of the culture media (A) and the acetate ambulation-to-ethanol consumption ratio of WT and engineered RHA1 strains (B) when using ethanol as the sole carbon source

WT indicates the wild type RHA1 strain. The dmpF-sthA indicates the RHA1 strain with gene overexpression of dmpF and sthA. The fasI-atf2 indicates the RHA1 strain with gene overexpression of fasI and atf2. The dmpF-sthA-fasI-atf2 indicates the RHA1 strain with gene overexpression of dmpF, sthA, fasI, and atf2. Data was collected using biological triplicates, and all values are presented as mean ± standard error of the mean. Turkey's multiple comparisons test was used to assess the significance of difference between the two groups. The * denotes a significant difference with $p < 0.05$, ** for $p < 0.01$, *** for $p < 0.001$, and **** for $p < 0.0001$. Only the significant difference in mean is shown in the figure.

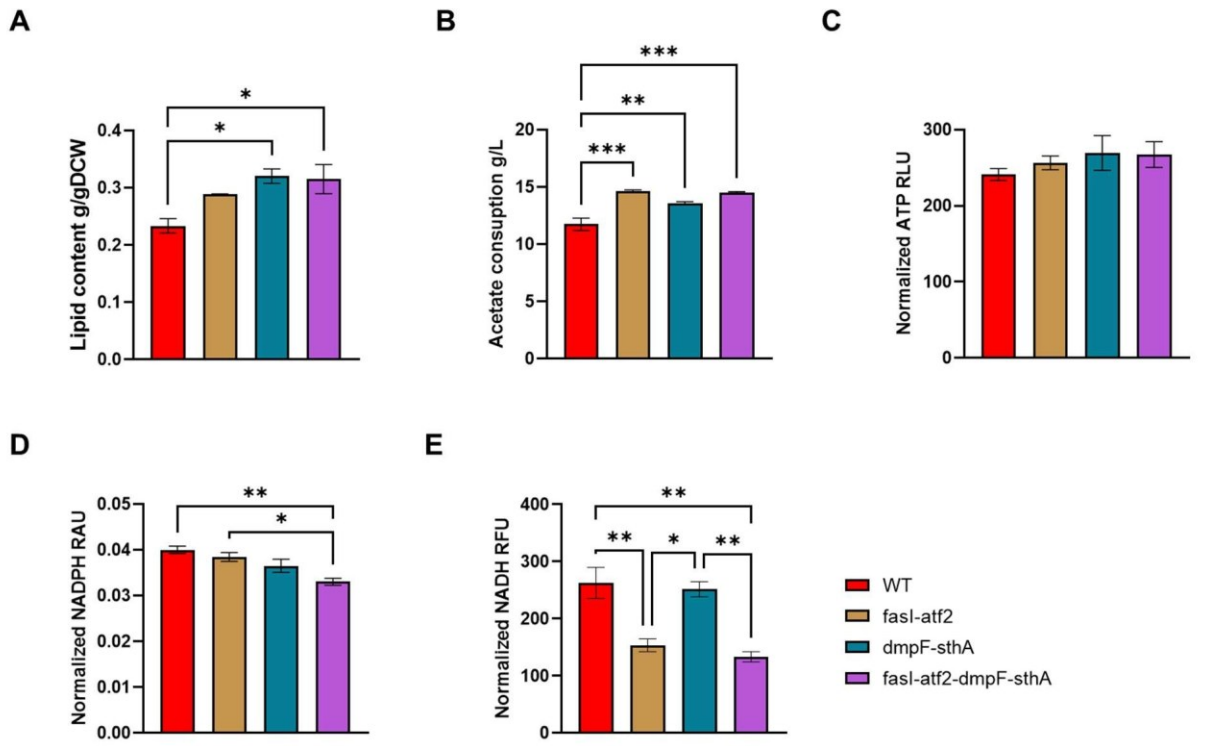

Figure S9. Experimental lipid fermentation results using the WT and engineering R. jostii RHA1 strains with acetate as sole carbon source

(A) Lipid content in DCW; (B) Acetate consumption; (C) Cellular ATP level; (D) Cellular NADPH level; (E) Cellular NADH level. RAU means relative absorbance units, RFU means relative fluorescence units, RLU means relative luminescence units. The legends are shared. Data was collected with biological triplicates, and all values are presented as mean ± standard error of the mean. T-test was used to assess the statistical significance of the difference between the two groups. The * denotes a significant difference with $p < 0.05$, ** for $p < 0.01$, *** for $p < 0.001$, and **** for $p < 0.0001$.

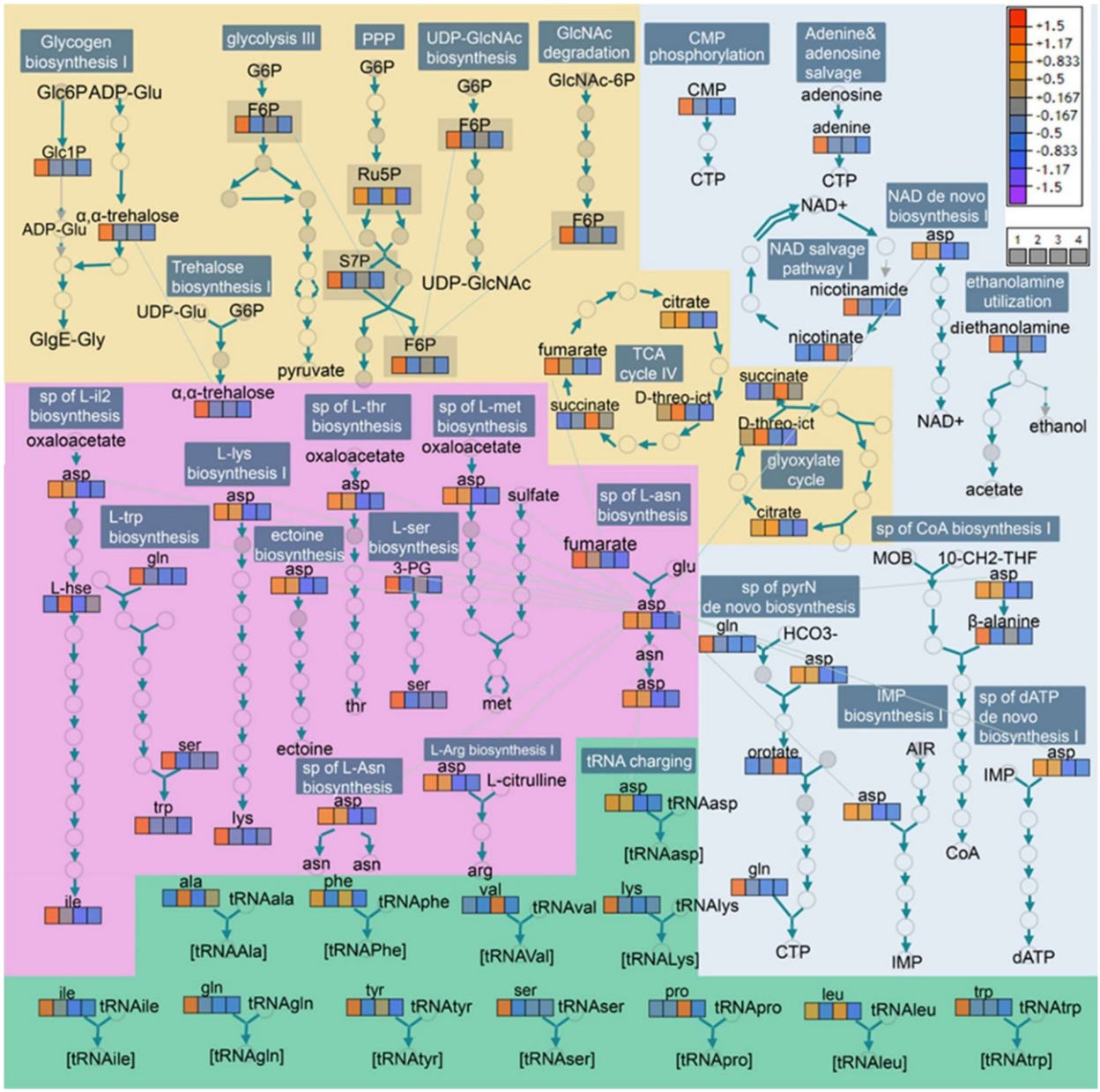

Figure S10. Visualization of the differential (Abslog2(FC)>1) primary metabolites of RHA1 strains between the ethanol and acetate conditions

The involved metabolic pathways based on the differential metabolite profile of the R. jostii RHA1 strains between conditions with ethanol or acetate as sole carbon source. The order of the box in the legend bar stands for 4 groups: (1) WT strain in ethanol (WT_ehtanol); (2) WT strain in acetate (WT_acetate); (3) fads strain in ethanol (fads_ethanol); and (4) fads strain in acetate (fads_acetate). The color of each box indicates the metabolite's relative level according to the scale in the upright conner. The intermediates in the pathways are represented as circles, where gray circles specifically indicate phosphate intermediates. Carbohydrate metabolisms were highlighted in yellow color, amino acids biosynthesis pathways were highlighted in pink color, tRNA charging reactions were highlighted in green color, metabolism related with nucleosides were highlighted in blue color. Glc-6P: galactose 6-phosphate; ADP-glu: ADP-α-D-glucose; Glc-1P: galactose 1-phosphate; GlgE-Gly: GlgE-Glycogen; UDP-GlcNAc: UDP-N-acetyl-α-D-glucosamine; GlcNAc: N-acetyl-α-D-glucosamine; G6P: D-glucopyranose 6-phosphate; PPP: pentose phosphate pathway; Ru5P: D-ribulose 5-phosphate; F6P: β-D-fructose-6-phosphate; UDP-Glu: UDP-α-D-glucose; NAD: Nicotinamide adenine dinucleotide; CMP: cytidine-monophosphate; D-threo-ict: D-threo isocitrate; Figure S10. Continued

asp: aspartate; lys: lysine; thr: threonine; ile: isoleucine; met: methionine; asn: asparagine; ala: alanine; ser: serine; L-hse: L-homoserine; D-ala: D-alanine; phe: phenylalanine; val: valine; arg: arginine; glu: glutamate; gln: glutamine; MOB: 3-methyl-2-oxobutanoate; 10-CH2-THF: 5,10-methylenetetrahydrofolate; PyrN: pyrimidine ribonucleotides; PRPP: 5-phospho-α-D-ribose 1-diphosphate; CTP: cytidine triphosphate; IMP: inosine-5'-phosphate; AIR: 5-amino-1-(5-phospho-β-D-ribosyl) imidazole; dATP: deoxyadenosine triphosphate; CoA: Coenzyme A; tRNA: transfer ribonucleic acid; sp: superpathway. All the metabolite levels were measured in biological triplicates and normalized for comparison. The tool Pathway Collages in website METACYC was used to visualize the pathways.[3]

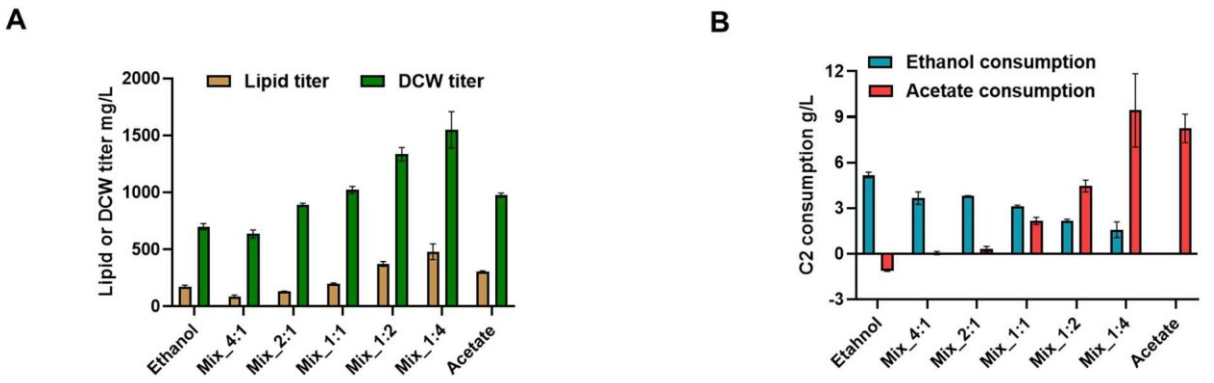

Figure S11. Co-substrate effect of different ratios of ethanol and acetate on lipid production (A) and C2 consumption (B) of WT RHA1

Ethanol: Ethanol as the sole carbon source; Acetate: Acetate as the sole carbon source; Mix: Mixed carbon source of ethanol and acetate. The carbon ratios in the mixed conditions are indicated alongside each annotation. For example, Mix 4:1: Mole ratio of ethanol to acetate is 4:1 in the mixed carbon source. Rhodococcus media with these C2 as sole carbon source was used to grow the RHA1 strain from an initial OD_{600} at about 0.2 for 54 hours, with C2 supplementation rate of 45mmol/L/12 h. All data were collected with biological triplicates, analyzed with GraphPad Prism 9.0.0 and presented as mean ± standard error of mean.

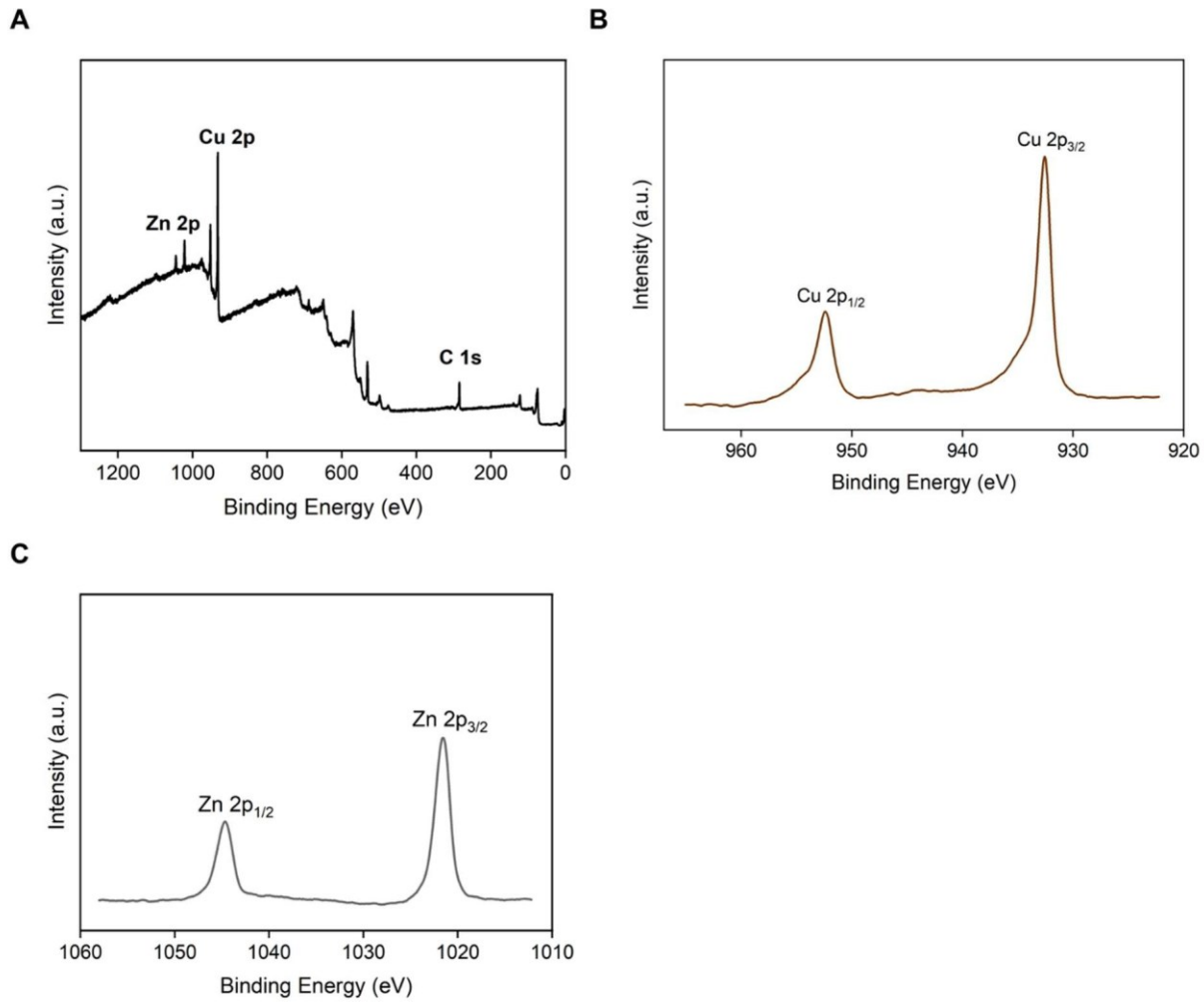

Figure S12. X-ray photoelectron spectroscopy (XPS) analysis for Cu_6Zn_1 catalyst. (A) survey, (B) Cu 2p, and (C) Zn 2p

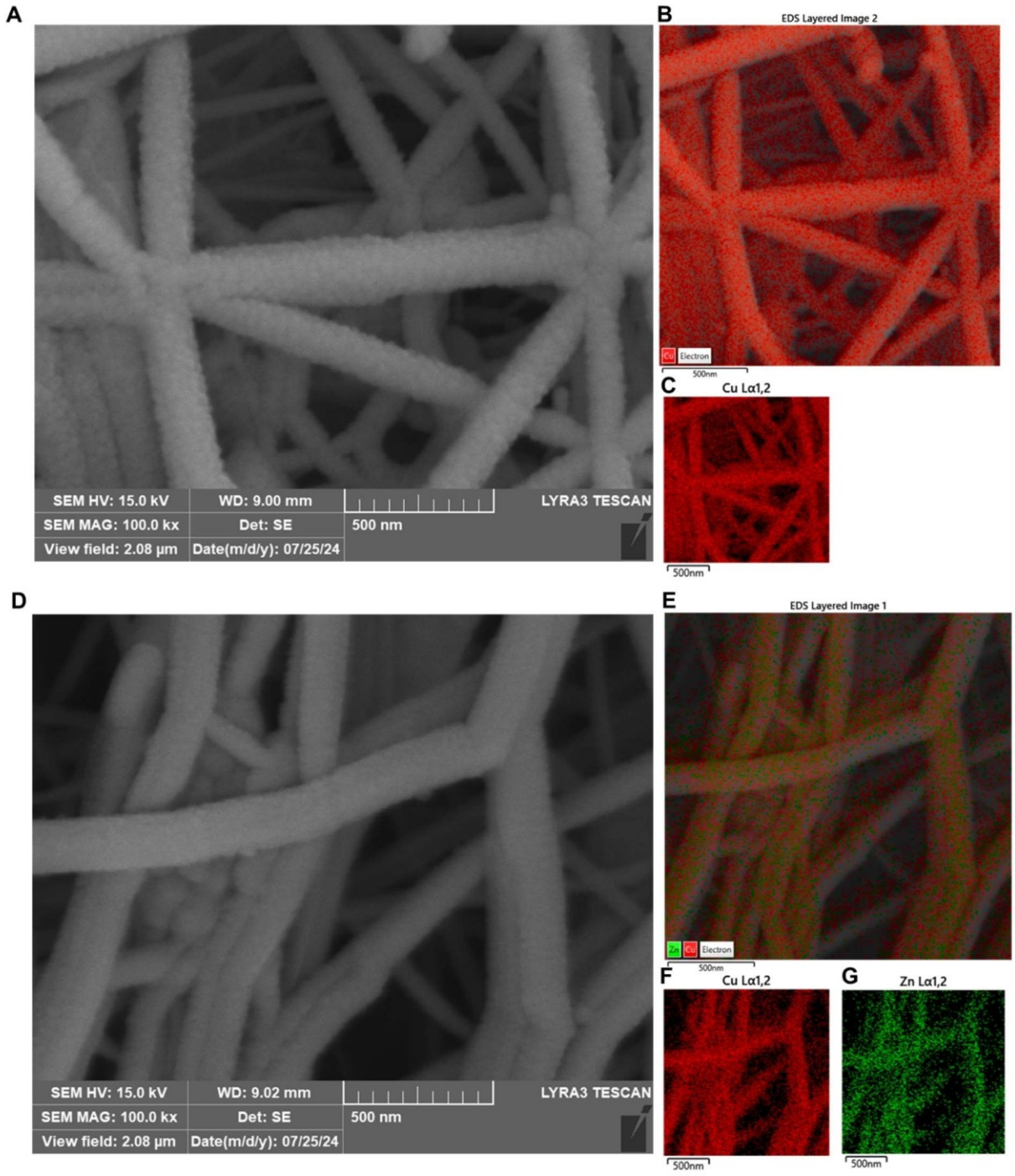

Element	Relative atomic %
Cu	85.56
Zn	14.44

Figure S13. Scanning Electron Microscopy (SEM) and Energy-dispersive X-ray spectroscopy (EDS) elemental mapping of Cu_6Zn_1 catalyst

(A and D) Low-magnification SEM image of the Cu and Cu_6Zn_1 catalyst. (B and E) Overall scan of EDS mapping. (C, F, and G) Images by Cu or Zn elements. Bottom: table of measured relative composition of Cu and Zn elements of Cu_6Zn_1 catalyst.

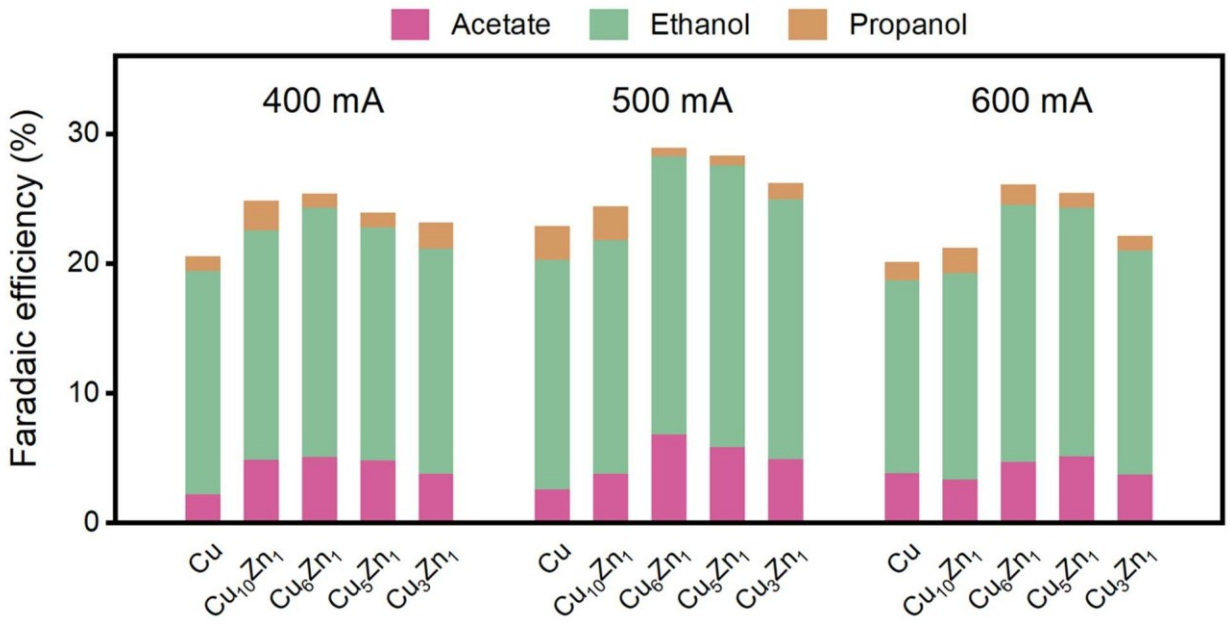

Figure S14. Faradic efficiency of C2+ oxygenates on catalysts with various Cu/Zn atomic ratios at different current densities

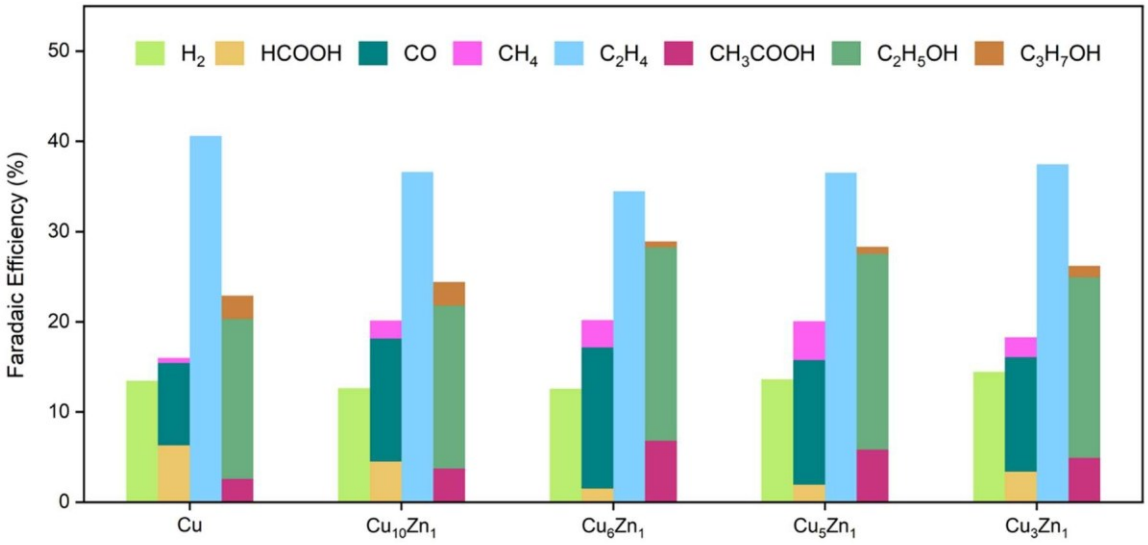

Figure S15. Faradic efficiency of generated products over the catalysts with different Zn loading amounts

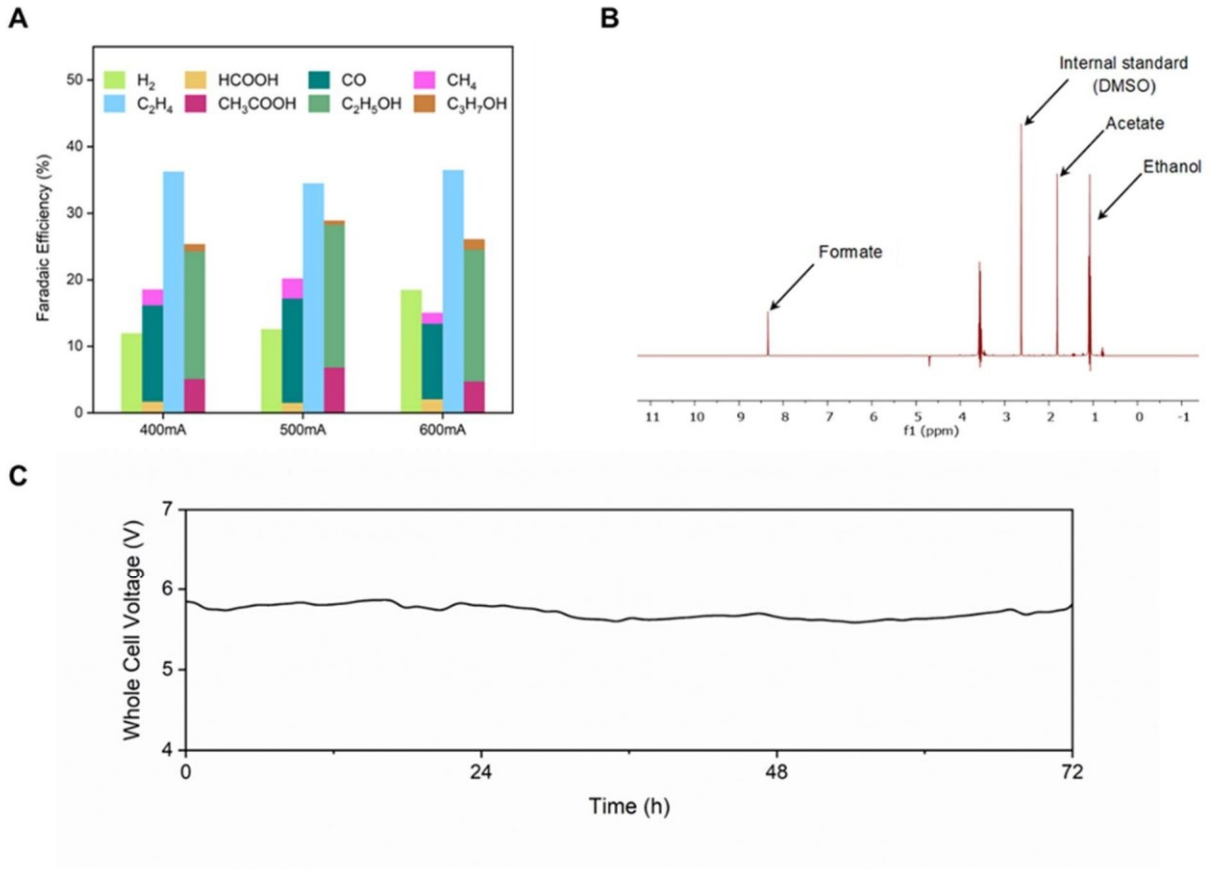

Figure S16. CO_2RR product profile and stability test of Cu_6Zn_1 catalyst
(1) Faradic efficiency of CO_2RR products of Cu_6Zn_1 at various total current densities. Partial current densities of each product, as $J = J \times FE$. (B) The ^{1}H NMR spectra for the liquid products after the reaction. (C) 72-hour stability test with the phosphate buffer used as the electrolyte.

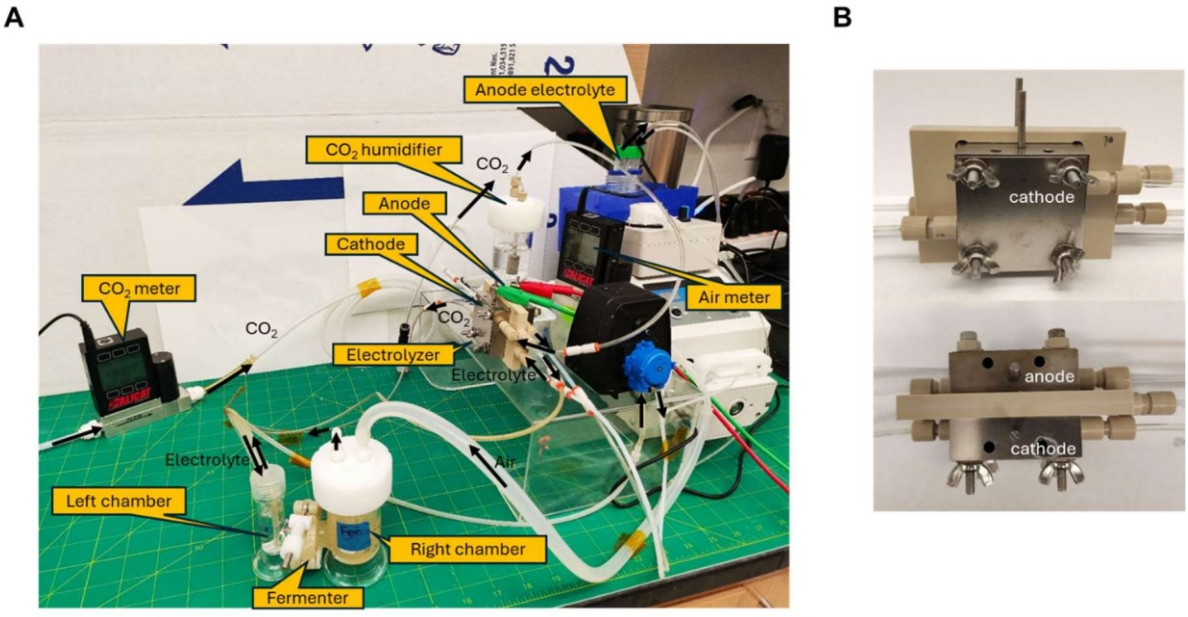

Figure S17. Electro-microbial integration setup (A) and the two-electrode electrolyzer configuration (B)

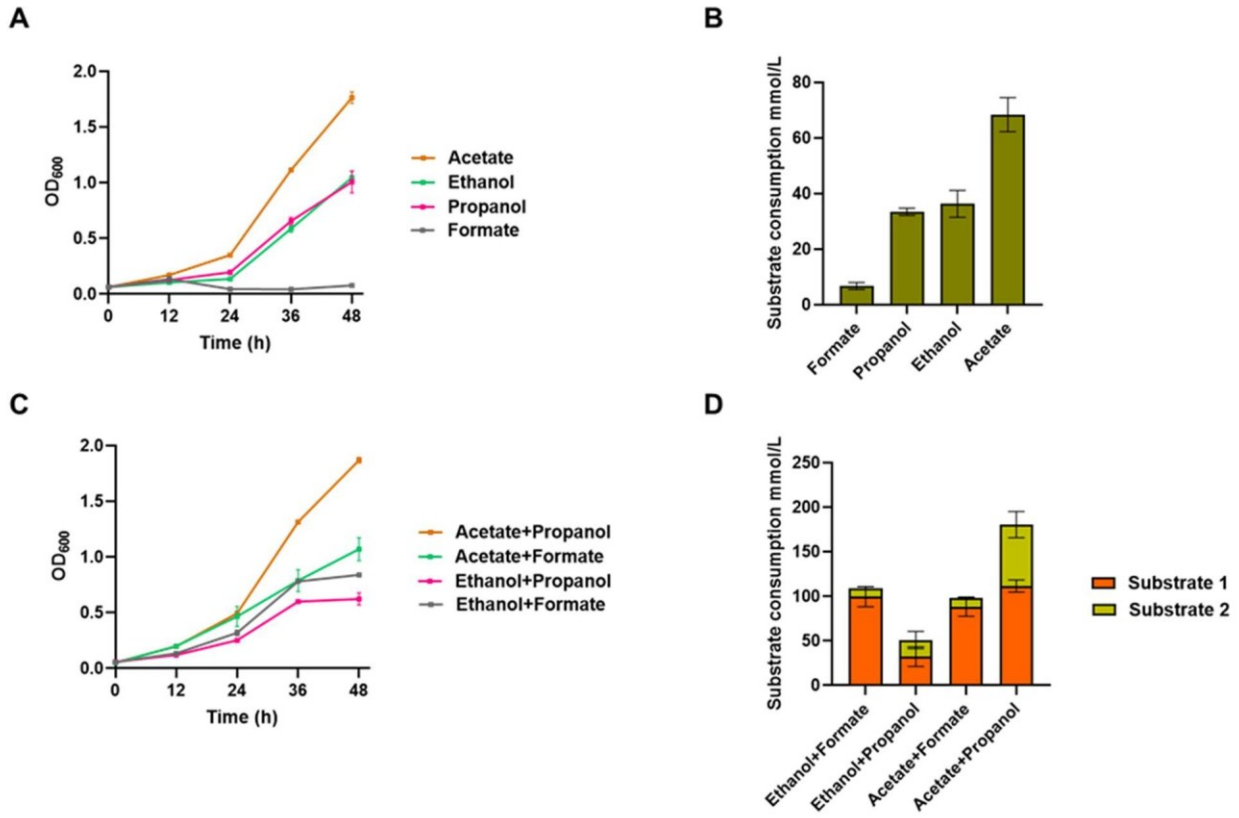

Figure S18. Effect of formate and propanol as carbon sources on cell growth of WT RHA1
(A) Cell growth of RHA1 when using each component of soluble CO_2RR products as sole carbon source. (B) Substrate consumption of RHA1 when growing on each component of soluble CO_2RR products. (C) Cell growth of RHA1 when C2 substrate supplementing with formate or propanol. (D) Substrate consumption of RHA1 when growing on C2 substrate supplementing with formate or propanol. Each substrate is provided at a 45mmol/L per 12 hours. All data were collected with biological triplicates and presented as mean ± standard error of mean.

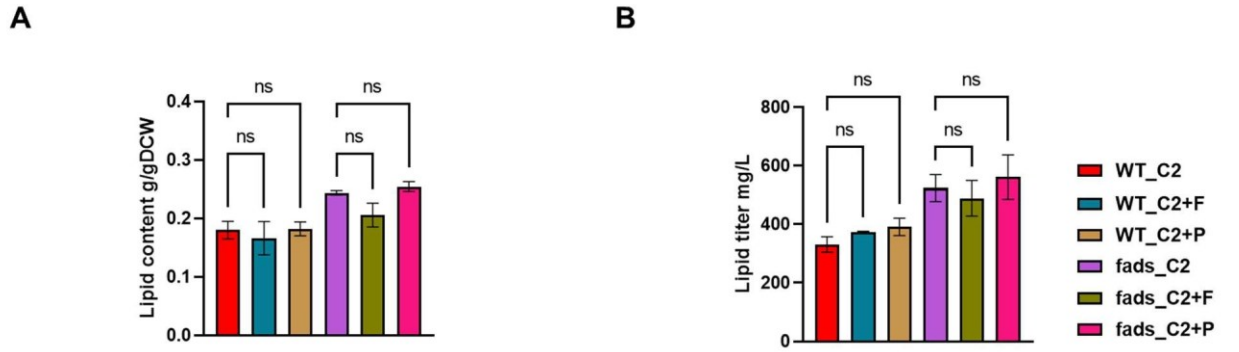

Figure S19. Effect of formate and propanol as carbon source on lipid production of WT RHA1 (A) Lipid content of RHA1 when with C2 supplementing with formate or propanol. (B) Substrate consumption of RHA1 when growing on each component of soluble CO_2RR products. “C2” indicate a mixture of ethanol and acetate, which were supplemented with 60 mmol/L/12 hour and 30 mmol/L/12 hour, respectively. "F" indicates formate, and "P" indicates propanol. They are supplemented at 50 mmol/L and 2.2 mmol/L every 12 hours, based on their ratios in the CO_2RR product profile. All data were collected with biological triplicates, analyzed with GraphPad Prism 9.0.0 and presented as mean ± standard error of mean. Turkey’s multiple comparisons test was used to assess the significance of difference between the two groups. The * denotes a significant difference with $p < 0.05$, ** for $p < 0.01$, *** for $p < 0.001$, and **** for $p < 0.0001$.

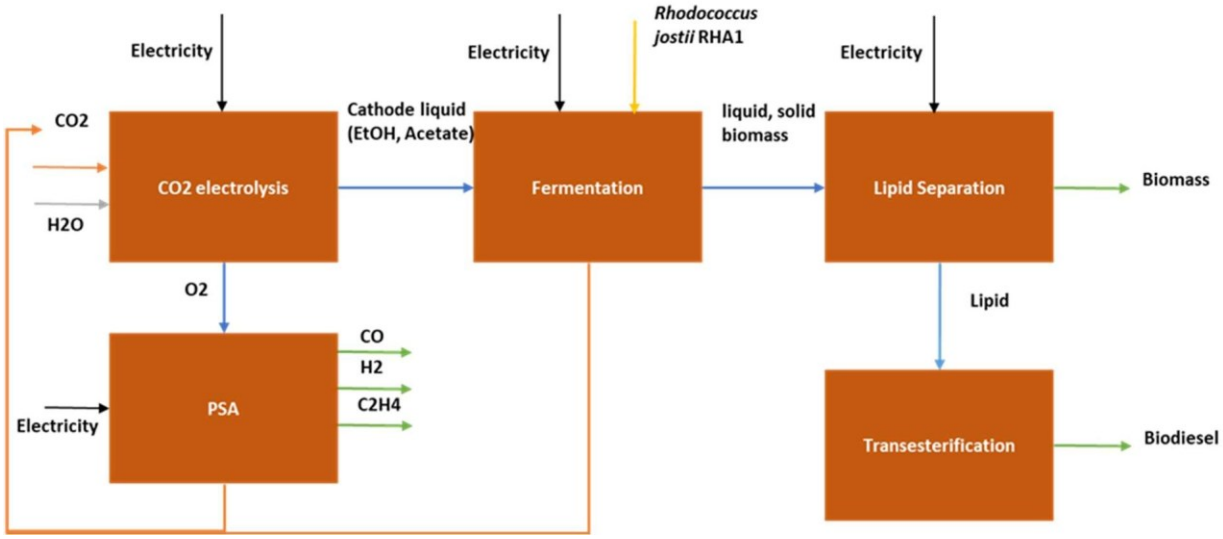

Figure S20. The boundary of the electro-biodiesel system in LCA analysis

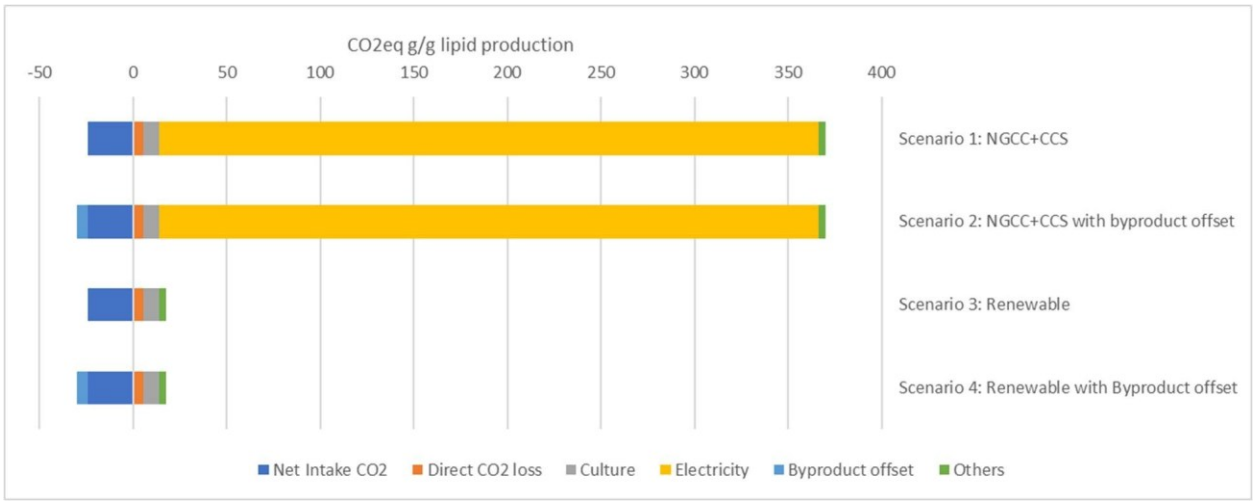

Figure S21. Scenario analysis for CO_2RR-Lipid system

Scenarios 1 and 2 assumed the system used electricity from the U.S. Natural gas combined cycle (NGCC) power plants with Carbon Capture and Storage (CCS) equipment. Scenarios 3 and 4 assume the system is powered by renewable electricity without extra GHG emissions. Scenarios 2 and 4 made an additional assumption that the byproducts from the system can displace conventional products and offset the GHG emissions from conventional sources.

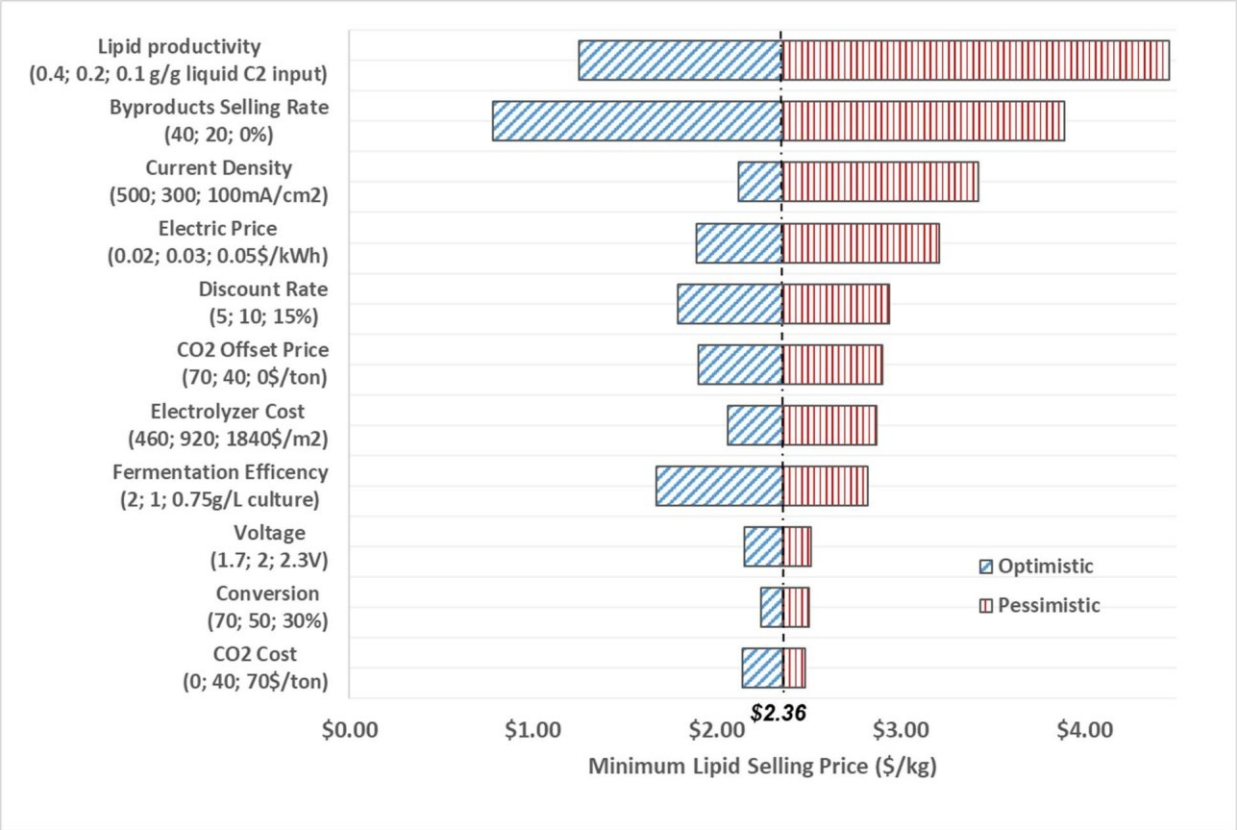

Figure S22. Sensitivity analysis for the minimum selling price of lipids ($/kg) based on the electrobiodiesel system The baseline scenario (vertical line) was calculated using the second number in each label as the input data, which results in a minimal selling price of lipids at $2.36/kg. The optimistic and pessimistic scenario analysis was then made assuming the current analyzed parameter taking the optimistic assumption (the first number in the label) or the pessimistic assumption (the third number in the label), but all other parameters taking the baseline assumptions (the second number in the labels).

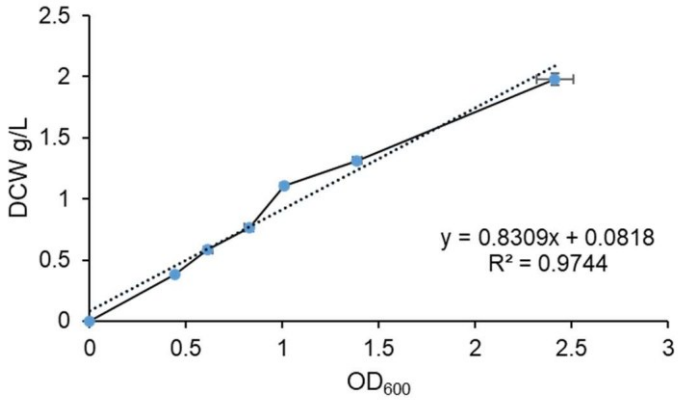

Figure S23. Relationship of OD_{600} and DCW of R. jostii RHA1 strain

Table S1. Comparison between electro-biodiesel and existing biodiesel production platforms

Platforms	Electrobiodiesel		Algal biodiesel		Soybean biodiesel		Palm biodiesel	
Global biodiesel consumption[§] (MJ/year)	3,003,216 × 10^6		3,003,216 × 10^6		3,003,216 × 10^6		3,003,216 × 10^6	
U.S. diesel consumption[Δ] (MJ/year)	8,276,728 × 10^6		8,276,728 × 10^6		8,276,728 × 10^6		8,276,728 × 10^6	
Photovoltaic energy output (MJ/acre/year)	2,913,739		N/A		N/A		N/A	
EE $_{\text{electricity-to-biodiesel}}$[¶]	17.2%		N/A		N/A		N/A	
Energy yield* (MJ/acre/year)	502,319		175,104		11,075.3		49,481	
Land use[#] (million acres)	5.98	16.5	17.2	47.3	271	747	60.7	167.3
Land use percentage[†]	0.30%	0.83%	0.86%	2.4%	14%	37%	3.0%	8.4%

[§] Worldwide biodiesel consumption is about 65.86 million tons in 2023, equivalent to 3,003,216 × 10^6 MJ per year.[4] [Δ] U.S. biodiesel consumption is about 3.7 million barrels per day, which is equivalent to 8,276,728 × 10^6 MJ per year. [¶] Energy efficiency (EE) of electricity-to-diesel of the electro-biodiesel system, calculated by multiplying EE of electricity-to-C2, EE of C2-to-lipid, and EE of lipid-to-biodiesel (See Calculation of energy efficiency for the Electro-biodiesel system). *Values show energy production rate per year per unit area in MJ (See Land use evaluation of different biodiesel platforms). [#] Values denote the theoretical land acres required to sustain the global biodiesel consumption (left column) or U.S. annual diesel consumption (right column). The values are calculated by dividing the energy of global biodiesel consumption or U.S annual diesel consumption by the energy yield of each diesel production platform. [†] Values are calculated by dividing the land use for each diesel production platforms by the total land area of the continental 48 states of the U.S. which is 1,996.7 million acers.

The tables S2-S7 are provided in Excel files in the Supplementary Information. Specifically, the Genome scale model (GSM) of RHA1 is constructed in the KBase platform.[5] The input information of media used to generate the model can be found in Table S2. The reactions and metabolites information for the generated GSM of RHA1 can be found in Table S3. The results of flux balance analysis (FBA) under the carbon uptake rate at 25 mmol/g DCW/h are provided in Table S4. In the FBA results, reactions that exhibit a difference in flux larger than 3 mmol/g DCW h between the ethanol and acetate conditions can be found in Table S5. The identified primary metabolites and lipid species of RHA1 wild-type strain and the engineered strain fads, and their relative peak intensity values are provided in Table S6. The results of differential analysis of the identified primary metabolites and lipid species between different strains and carbon source conditions can be found in Table S7.

Table S8. Inputs and outputs data per 1 gram of lipids

Inputs	Usage	unit
CO_2	422.70	g
Culture Medium (Table S9)	1	L
Electricity	4.63	kWh
Outputs	Production	unit
Lipids	1	g
H_2	0.26	g
CO	3.19	g
CH_4	0.02	g
C_2H_4	2.92	g
biomass	0.76	g
CO_2 (recycled)	398.69	g
CO_2 (direct)	5.54	g

Table S9. Elements of 1 L Culture Medium and Associated CO_2e Emissions

Culture	Concentration	Unit	Usage(g)	Emission factors (g CO_2e/g product)	Total CO_2e Emissions (g)
KH_2PO_4	1.70	g/L	1.70E+00	3.00	5.10
Na_2HPO_4	9.80	g/l	9.80E+00	0.31	3.04
$MgSO_4$	0.10	mg/l	1.00E-04	0.30	0.00
$FeSO_4•7H_2O$	0.95	mg/l	9.50E-04	0.18	0.00
MgO	10.75	mg/l	1.08E-02	0.71	0.01
$CaCO_3$	2.00	mg/l	2.00E-03	0.01	0.00
$ZnSO_4$	1.20	mg/l	1.20E-03	0.82	0.00
$CuSO_4$	0.20	mg/l	2.00E-04	1.00	0.00
$CoSO_4•7H_2O$	0.15	mg/l	1.50E-04	6.36	0.00
H_3BO_4	0.06	mg/l	6.00E-05	0.72	0.00
HCl	51.30	ml/l	5.13E-02	1.20	0.06
				Total	8.21

Note: The emission factors are sourced from the following websites: For KH_2PO_4[6] and $CaCO_3$[7] are both sourced from CarboClound. The emission factors for the rest chemicals are sourced from Winnipeg.[8]

Table S10. Life Cycle Impact Assessment of electro-biodiesel system

Produce 1 g lipid		Greenhouse Gas Emissions (g CO_2e/g lipid)			
		Scenario 1	Scenario 2	Scenario 3	Scenario 4
CO_2 Electrolysis	Intake CO_2	-422.7	-422.7	-422.7	-422.7
	Direct CO2 loss	5.54	5.54	5.54	5.54
	CO_2 in System Recycle	398.69	398.69	398.69	398.69
Fermentation	Culture (details in Table S9)	8.21	8.21	8.21	8.21
Extraction and centrifugation	Chloroform for extraction	3.7	3.7	3.7	3.7
Transesterification	Methanol-HCl and toluene for Transesterification	1.29	1.29	1.29	1.29
Electricity Total	CO_2 electrolysis	188.03	188.03	~0	~0
	PSA	2.65	2.65	~0	~0
	Fermentation	114.47	114.47	~0	~0
	Extraction and Centrifugation	47.3	47.3	~0	~0
Byproducts		3.70	-5.75	3.70	-5.75
Total Greenhouse Gas Emissions (g CO_2e/g lipid)		349.59	343.85	-2.86	-8.61
Total Greenhouse Gas Emissions (g CO_2e/g biodiesel)		350.88	345.14	-1.57	-7.32

Note: the emission factor of chloroform is 4.13 g CO_2e/g chloroform from GREET.[9] According to the current studies, chloroform could be recycled, and 2% loss rate is assumed.[10] Scenarios 1 and 2 assumed the system used electricity from NGCC power plants with CCS equipment. Scenarios 3 and 4 assume the system is powered by renewable electricity without extra GHG emissions. Scenarios 2 and 4 made an additional assumption that the byproducts from the system can displace conventional products and offset the GHG emissions from conventional sources. The sensitivity analysis is based on the following assumptions: 1) CO_2 from bacterial culturing and lipid fermentation can be recycled for the CO_2 electroreduction; 2) Soluble C2 products that are not completely utilized to produce 1 gram lipid can be recycled and utilized by next round; 3) The amount of salts and trace elements in the medium for bacterial culturing and lipid fermentation is not recycled.

Table S11. Byproduct Allocation

Byproduct (1 g)	Alternative Source	Emission Factors
Biomass	1 g biomass from corn stover	0.06
H_2	1 g hydrogen from renewable natural gas	0.64
C_2H_4	1 g ethylene from corn stover	0.63
CO	1 g carbon monoxide from polyethylene terephthalate resin	0.97
CH_4	1 g methane is equivalent to 28 g CO_2 for 100-year global warming potential	28

Note: The emission factor of CH_4 is referenced from the web site source[11]. The rest emission factors are referenced from GREET.[9]

Table S12. Comparison of carbon emissions of different diesel production routes

Production Route	Feedstock	CO_2e Emissions (g/g)	Reference
Fractionation	Petroleum	0.52	GREET
Transesterification	Soybean	0.73	GREET
Transesterification	Soybean/canola/carinata	21-31 g/MJ	[12]
Hydro-processing	Soybean/canola/carinata	22.68-34.1 g/MJ	[12]
Transesterification	Microalgae	0.85-1.46	[13]
Lipid only	Microalgae	2.5-9.9	[14]

Table S13. Plasmids and strains used in this study

Plasmids and strains	Genotype or description	Reference
Plasmids		
PDD120	pConstitutive-Che9c60::Che9c61: pBR322 origin of replication, km^R, Gene-overexpression plasmid.	[15]
PBSNC9031-Pben-FAS	pBenA-FASI: pNC903 origin of replication, Ts^R, E. coliRhodococcus shuttle plasmid for fasI and atf2 overexpression in R. opacus.	[16]
PDD120-dmpF-sthA	pConstitutive-dmpF::sthA: pBR322 origin of replication, km^R, overexpression dmpF and sthA.	This study
PBSNC9031-fasI-atf2dmpF-sthA	pBenA-FASI::pConstitutive-dmpF::sthA: pNC903 origin of replication, Ts^R, E. coli-Rhodococcus shuttle plasmid for overexpression of fasI, atf2, dmpF, and sthA in R. jostii RHA1.	This study
Strains		
E. coli K-12 DH 5α	K12 derivative; F^-, λ-, hsdR(rk^-, mk^-), supE44, thi-1, recA1, endA1, Δ(lacZYA-argF)U169, Φ80dlacZ, ΔM15, deoR, nupG	[17]
R. jostii RHA1	Wild type	[18]
dmpF-sthA	dmpF and sthA overexpression	This study
fasI-atf2	fasI and atf2 overexpression	This study
fasI-atf2-dmpF-sthA (fads)	fasI, atf2, dmpF and sthA overexpression	This study

Table S14. Primers used in this study

Primers	Sequence	Purpose
sthA_F	ATGCCACATTCCTACGATTA	Amplify sthA for overlapping PCR
sthA_R	TTAAAACAGGCGGTTTAAA	Amplify sthA for overlapping PCR
ArtRBS-sthA_F	CCTCTGTTCCCAAGGGGAGAAGCCGAA ACATAAAAAGGAGGTCTTTTATGCCACA TTCCTACGATTA	Amplify sthA and add rbs for overlapping PCR
ArtRBS-sthA_R	TTAAAACAGGCGGTTTAAA	Amplify sthA and add rbs for overlapping PCR
G2-dmpF_F1	attaagaaggagatatacatATGACCAAGGCAAG TGTGGC	Amplify dmpF for overlapping PCR. Gibson assemble for PDD120dmpF-sthA

G2-dmpF_R1	TCTCCCCTTGGGAACAGAGGTCATGCCT CCACGCTCAGGAG	Amplify dmpF for overlapping PCR. Gibson assemble for PDD120dmpF-sthA
G3_F2	TCCTGAGCGTGGAGGCATGACCTCTGTT CCCAAGGGGAG	Gibson assemble for PDD120-dmpF-sthA
G3_R2	cgttgtacttttcggccttctcaaaaaagccggttcaggcc	Gibson assemble for PDD120-dmpF-sthA
G4_Fvec	gcctgaaccggctttttgagaaggccgaaaagtacaacg ac	Gibson assemble for PDD120-dmpF-sthA
G4_Rvec	GCCACACTTGCCTTGGTCATatgtatatctcctt cttaattaagcatgcgga	Gibson assemble for PDD120-dmpF-sthA
PbenA-fasI_F	TACTCCGGGTACCTGTGCGG	amplify fasI for overlapping
PbenA-fasI_R	CTACTTGCAGCCGGGCAGACCC	Amplify fasI for overlapping
rest_F	GAACGACGGATGGGAGTTCTGG	amplify PNSNC9031 vector with atf2 gene for overlapping
rest_R	ACATGTGAGCAAAAGGCCAGCAAAAGG	amplify PNSNC9031 vector with atf2 gene for overlapping
pC-dmpF_F	TGTGCGGGCTCTAAC	Amplify pConstitutivedmpF-sthA for overlapping
sthA_R	TTAAAACAGGCGGTTTAAA	Amplify pConstitutivedmpF-sthA for overlapping
GibInte_fasI_F1	CTGGCCTTTTGCTCACATGTTACTCCGG GTACCTGTGC	Gibson assemble for PBSNC9031-fasI-atf2dmpF-sthA

Table S14. Continued

GibInte_fasI_R1	gacgtgttagagcccgcacaCTACTTGCAGCCG GG	Gibson assemble for PBSNC9031-fasI-atf2dmpF-sthA
GibInte_pC-dmpF_F2	GTCTGCCCGGCTGCAAGTAGtgtgcgggctct aac	Gibson assemble for PBSNC9031-fasI-atf2dmpF-sthA

GibInte_pC-dmpF_R2	AGAACTCCCATCCGTCGTTCTTAAAACA GGCGGTTTAAA	Gibson assemble for PBSNC9031-fasI-atf2dmpF-sthA
GibInte_vec_F	TTTAAACCGCCTGTTTTAAGAACGACGG ATGGGAGTTCT	Gibson assemble for PBSNC9031-fasI-atf2dmpF-sthA
GibInte_vec_R	CCGCACAGGTACCCGGAGTAACATGTG AGCAAAAGGCCAGCA	Gibson assemble for PBSNC9031-fasI-atf2dmpF-sthA

Solar-to-fuel energy efficiency of different biodiesel platforms Data shown in

Figure 1 are based on the following calculation.

The energy conversion efficiency of each process to produce biofuel, electro-fuel, and electro-biofuel is referenced from literature. The operational photosynthetic energy conversion efficiency of for microalgal cultivation is about 1%.[19] Most crops convert sunlight and CO_2 into plant biomass at an energy efficiency of 1% or less.[20] The overall energy conversion efficiency from solar to algal and soybean oils is thus less than 1% (Figure1). The achievable energy conversion efficiency of photovoltaic technology in practical applications can reach 25% of energy efficiency.[21] Selective CO_2 electroreduction to methanol can reach a faradic efficiency at 80%, which is up to 43% of energy conversion efficiency according to the potential difference between cathode and anode.[22] Selective conversion of CO_2 to methane achieved a faradaic efficiency exceeding 70% under industrial current density conditions, resulting in an energy efficiency of approximately 12% with their applied cell potential.[23] The half-cell cathodic energy efficiency of ethanol chemical productions from electrochemical CO_2 reduction can reach about 22%.[24] The advanced CO_2-toacetate electroreduction reached about 40%.[25] The energy efficiency of converting solar energy into C1 or C2 fuels such as methanol, methane, and ethanol thus falls within the range of 3-11% (Figure1). C2 feedstocks such as ethanol and acetate can support an energetic efficiency of 35-55% for microbial cell growth.[26] The estimated energy conversion efficiency of solar-electro-microbial biomass thus falls in the range of 1.9-5.5% (Figure 1).

Land use evaluation of different biodiesel platforms

Data shown in Figure 1 and Table S7 are based on the following calculation.

The U.S. diesel consumption is 3.7 million barrels per day, which is referenced from EIA report[27], equating to 8,276,728,320,000 MJ/year. For the electro-biodiesel production platform, its electricity input is sourced from maturing photovoltaic technology, which requires as low as 5,000 m^2 land per year to generate 1 GWh electric power. It means the power production rate is about 200 kWh/m^2/year, equating 2,913,739 MJ/acre per year.[28] Based on the assumption that land use of electro-biodiesel platform is mainly contributed by photovoltaic panel with the electro-biodiesel system being integrated under solar panel without extra land use, the energy productivity per unit land of the electro-biodiesel can be calculated by multiplying the electric power production rate by energy efficiency (EE) of downstream steps, including 49.2% EE of electricity-toC2, 36.5% EE of C2-to-lipids, and 96.0% EE of lipid-to-biodiesel (See below section Calculation of energy efficiency for the Electro-biodiesel system), resulting in 502,319 MJ/acre per year. To fulfill the annual demand of diesel, it needs 16.5 million acres, which 274 accounts for about 0.83 % of the total land area (1,996.7 million acers) of the continental 48 states of the U.S. (Table S1).

For algal biodiesel approach, the reported achievable annual production is 12,00 gallons/acre/year, according to NERL[29], equating 175,104 MJ/acre/year, which thus requires about 47.3 million acres of land to meet the total diesel production (Table S1).

For the soybean biodiesel approach whose annual production is around 50.6 bushels per acre according to the USDA Crop Production 2023 Summary.[30] Based on a yield of approximately 1.5 gallons of biodiesel produced per bushel of soybean, one acre of land produces estimably 75.9 gallons of soy-diesel per year, which translates into 11,075.3 MJ/acer/year. It thus needs 747 million acres to meet the annual diesel consumption in the USA (Table S1).

The global biodiesel consumption is approximately 65.86 million tons, equating 3,003,216 × 10^6 MJ.[31] It's reported that each hectare of land (2.47 acres) can produce around 2.9 tons of palm oil.[32] Given that 0.991 million tons of palm oil can yield 1.078 billion liters of palm methyl ester[33], one acre of land can produce approximately 1,276.6 liters of palm-diesel annually, translating into 49,481 MJ/acre/year, calculated by using diesel's energy content of 45.6MJ/kg and density of 0.85kg/litter. Hence, it would require 60.7 million acres of land. In comparison, with an electro-biodiesel system capable of producing 502,319 MJ/acre/year, only 5.98 million acres would be needed to meet current global biodiesel consumption, representing less than 10% of the current land usage. More importantly, this land will not come with the deforestation of rain forest and does not need to be arable land.

Cell growth monitoring and pH measurement

For every 12 hours, 200 μL of cell culture were taken from the culture media and transferred into one well of a 96-well plate, and then the absorbance at wavelength 600 nm was measured with path check using a plate reader SpectraMax iD5 (Molecule Device, USA). The reads are referred to as optical density OD_{600} in this work to indicate the cell growth. And the relation between OD_{600} and DCW is shown in Figure S23. For pH measurement, a 1.0 mL

culture medium was taken from a 50 mL culture medium to a 15 mL culture tube for pH measurement using a pH meter (Apera Instruments, USA). All the data are collected with three biological replicates.

ATP measurement

Cellular ATP level is critical factor impacting fatty acid biosynthesis and lipid production in oleaginous microorganism such as Rhodococcus.[34] ATP measurement was performed using the Sigma-Aldrich ATP Assay Kit (MAK135) according to the manufacturer's instructions.[35] Specifically, biological triplicates of 10 mL of RHA1 cells were grown in Rhodococcus media with 45mmol/L ethanol or acetate as sole carbon source in advance. ATP reagent for the assay was prepared according to the kit protocol and 90 μL of the ATP reagent solution was transferred into appropriate wells in in a 96-well plate. RHA1 cells at OD_{600} about 0.2 to 0.3 indicating the cells had passed the lag phase and begun to grow were sampled for cellular ATP measurement. Cells were prepared by dilution with PBS to OD_{600} at around 0.1 and 10 μL of the cell suspension was transferred into appropriate wells. After gently mixing, the plate was incubated at room temperature for 10 min before luminescence measurement by SpectraMax iD5 (Molecule Device, USA). Reading of luminescence (relative light units) was normalized by the dilution factors and cell density (OD_{600}) of the cell sample to compare the relative ATP level between different samples (Figures 2E and 4E).

NAD(P)H level measurement

Given that ethanol and acetate have different energy contents and yield varying amounts of reducing power during their metabolism, we employed a fluorescence-based method to measure the levels of NAD(P)H (NADH and NADPH) between the two C2 conditions (Figure S7D).[36] Specifically, biological triplicates of 10 mL of RHA1 wild-type and engineered cells were grown in Rhodococcus media with 45mmol/L ethanol or acetate as sole carbon source in advance. 200 μL of cells were collected and used for NAD(P)H measurement. SpectraMax iD5 (Molecule Device, USA) was used for fluorescence signal measurement. The 340 nm was used for excitation wavelength, and the fluorescence emission at 460 nm wavelength was measured. Then the Reading of fluorescence was normalized by (OD_{600}) and used to compare NAD(P)H level between samples.

NADPH and NADH measurement

The supply of NADPH and NADH is an important factor to support lipid production in oleaginous Rhodococcus.[34] The selective quantification of NADPH was done using a NADP/NADPH Assay Kit (MAK312, Sigma). Briefly, RHA1 cells grow in the Rhodococcus media with 45mmol/L ethanol or acetate as sole carbon source at log phase (OD_{600} in range between 0.4 and 0.5) was diluted to OD_{600} at around 0.2. Then the cells from three biological replicates were incubated with 80 μL of working reagents with enzymatic probes for specific detection of NADPH. Absorbance for NADPH quantification (OD_{565}) was measured at minute 0 and 30 using a TECAN (Molecule Device, USA) plate reader. The absorbance signal readings were normalized by cell density to allow comparison between samples. The resulting relative absorbance units (RAU) were compared between the WT and engineered strains (Figures 2F and 4D).

Similarly, the selective quantification of NADH was performed using the NAD/NADH Assay Kit (MAK460, Sigma). The cells were lysed and then incubated with 50 μL of working reagents with enzymatic probes for the specific detection of NADH. Fluorescence for NADH quantification (ex = 530 nm / em = 585 nm) was measured at minute 0 and 10 using a TECAN (Molecule Device, USA) plate reader. The fluorescence signal readings were normalized by cell density to allow comparison between samples. The resulting relative fluorescence units (RFU) were compared between the WT and engineered strains (Figures 2G and 4F).
Each sample was analyzed in three biological replicates.

Acetyl-COA measurement

Acetyl-CoA is a crucial intermediate product with a primary role in transporting the acetyl group into the Krebs cycle, where it is oxidized for energy production. The selective quantification of acetyl-CoA was performed using the Acetyl-CoA Colorimetric Assay Kit (E-BC-K652-M, Elabscience®). RHA1 cells grow in the Rhodococcus media with

45mmol/L ethanol or acetate as the sole carbon source and were diluted to OD_{600} at around 0.4. The cells were lysed and then incubated with 230 µL of working reagents with enzymatic probes for the specific detection of acetyl-CoA. Absorbance for acetyl-CoA quantification (OD_{340}) was measured at minute 0 and 1 using a TECAN (Molecule Device, USA) plate reader. The absorbance signal readings were normalized by cell density to allow comparison between samples. Each sample was analyzed in three biological replicates, and all samples were measured immediately or incubated according to different stages of the measurement. The resulting relative absorbance units (RAU) were compared between the WT and engineered strains (Figure 2D).

Lipid extraction, transesterification, and quantification

The RHA1 cells were harvested through centrifugation at 3000 × g for 10 minutes. Following that, the cells underwent two washes with ddH_2O and were subsequently lyophilized for 2 days. Total DCW of each sample was measured with analytic balance (Sartorius, Michigan). Approximately 5-10 mg of the lyophilized cells were dissolved in a mixture of 2 mL methanol-sulfuric acid (v/v=85:15) and 2 mL chloroform. The resulting solution was then incubated at 100°C for four hours, during which acid-catalyzed methyl esterification converted the fatty acids of lipids into their corresponding methyl esters, which were dissolved in chloroform. After cooling, the samples were washed twice with 2 mL of demineralized water until no acid residual remained. The upper layer (water phase) was removed after each wash. The fatty acid methyl esters (FAME) are in the organic layer and can be obtained by evaluating the chloroform by a gentle stream of nitrogen in a fume hood.

For quantification of lipid production, the organic layer was then diluted with chloroform by 20 times and added with internal standard methyl benzoate with a concentration at 21 µg/mL. The final solution was filtered using a 0.2 µm filter before being analyzed by GC-MS (QP2010SE, Shimadzu) with a Zebron ZB35HT Inferno column (30 m × 250 µm ID × 0.25 µm df). Helium was used as the carrier gas with a flow rate of 1.0 mL/min. The column temperature was programmed to start at 50 °C for 3 minutes and ramped to 300 °C at a rate of 10 °C/min. The injector temperature was set to 250 °C. Mass spectra were recorded with a 70 eV electron beam at an ionization current of 40 µA.

The quantification for each component was performed through calculating a response factor (RF) for each component analytical standard. For example, the RF for C16 monomer analytical standard was calculated using the following expression:

$$RF = (A_{C16} \times C_{in}) / (A_{in} \times C_{C16}) = (A_{C16} / A_{in}) / (C_{C16} / C_{in})$$

where A_{C16} is the peak area of C16 (palmitic acid) analytical standard, which was detected as methyl palmitate following transesterification, A_{in} is the peak area of the internal standard methyl benzoate; C_{C16} and C_{in} are the concentrations of the C16 analytical standard and internal standard methyl benzoate, respectively. Based on the peak area and concentration of internal standard, and the peak area of C16, the concentrations of C16 monomer in the 2 mL GC/MS sample were determined. The weight of lyophilized cells used for lipid extraction was then employed to calculate the lipid content in the RHA1 cells.

To analyze the transesterification yield, about 100 mg of palmitic acid (C16), the most abundant fatty acid in the lipid, was accurately weighed and dissolved in the mixture of 2 mL methanol-sulfuric acid (v/v=85:15) and 2 mL chloroform to go through the methyl esterification reaction. After washing the sample twice with demineralized water, the ester product was obtained by evaporating the organic layer in the fume hood overnight. The ester product was accurately weighed, and the reaction yield was calculated using the following formula:

$$\text{Yield} = \frac{(\quad)}{(\quad)} \times 100\%$$

where the theoretical weight of the ester product is the weight of methyl palmitate converted from 100 mg of palmitic acid by 100% methylation, which is 105.5 mg.

Metabolomics analysis of primary metabolism and complex lipids

Biological triplicates of RHA1 WT and fads (overexpression of fasI, atf2, dmpF, and sthA genes) cells cultured in Rhodococcus media with ethanol or acetate as sole carbon source were collected, immediately frozen with liquid N2, and preserved in -80 freezer. The frozen samples were delivered in dry ice condition to the West Coast Metabolomics

Center at University of California Davis to analyze metabolites. All the sample preparation, metabolites extraction and measurement, data acquisition and analysis were conducted at the UC Davis Metabolomics Center. Briefly. Gas chromatography time-of-flight mass spectrometer-mass spectrometry (GC-TOF-MS) in automated liner exchange cold injection system (ALEXCIS) was used to detect primary metabolites. The sample preparation was performed utilizing their established techniques for metabolite profiling[37] and while data acquisition employed the chromatographic parameters described in their previous study.[38] Electrospray ionization quadrupole time of flight mass spectrometer tandem mass spectrometry (ESI QTOF MS/MS) was used to detect the complex lipids extracted from samples. The complex lipid were extracted by using the methyl-tert-butyl ether method.[39] The general data processing workflow involved the use of MS-DIAL [40] for initial processing, followed by blank subtraction in Microsoft Excel and data cleanup using MS-FLO.[41] Peaks were annotated by manually comparing MS/MS spectra and accurate masses of the precursor ion to the spectra provided in the Fiehn laboratory's LipidBlast spectral library.[42]

Bioinformatics analysis and visualization

The peak intensities of all annotated chemicals were normalized based on the sample weights used for the analysis experiment. These normalized values of the identified metabolites were subsequently subjected to statistical analysis using MetaboAnalyst 5.0.[2] Interquartile range (IQR) method and a threshold value of 5% was used for sample filtering. For the primary metabolism, fold change analysis was performed (WT_EtOH vs WT_AA, fads_EtOH vs fads_AA, WT_EtOH vs fads_EtOH, and WT_AA vs fads_AA) on all identified primary metabolites with default parameter setting to find significantly changed metabolites (Figure 3A). To visualize the data, the values of the metabolites were standardized and mapped onto the metabolic pathways based on the R. jostii RHA1 representative genome in BioCyc database (https://biocyc.org/overviewsWeb/celOv.shtml?orgid=GCF_000014565#) (Figure 3A). For the complex lipids, t-test analysis was performed on the identified lipid compounds with significance level of 0.05 to find significantly changed. These lipid compounds were further classified with enrichment analysis using the main class of chemical structures library in the MetaboAnalyst 5.0 platform.[2] The hit numbers of lipid compounds in each category were visualized as back-to-back bar plots with R studio (Figure 3B).

Electrochemical CO_2 reduction

The electrochemical CO_2 reduction reactions (CO_2RR) were performed using the Autolab PGSTAT302N potentiostat/galvanostat (METROHM) in the two-electrode mode. A customized dual-membrane electrolyzer[43] was used to evaluate the reaction performance. The electrolyzer configuration is shown in Figure 6A. On cathode side, a 4 cm^2 Cu/Zn gas diffusion electrode (GDE) with porous PTFE base was employed. 30 standard cubic centimeters per minute (sccm) of humidified CO_2 was fed on its backside to provide CO_2 and water vapor to cathode catalyst. An anion-exchange membrane (AEM, Sustainion X3750 RT, Dioxide Materials) was masked on the cathode to avoid the cations deposition, while allowing liquid products transportation. On the anode side, 4 cm^2 Ni foam was employed for water oxidation using 1 M KOH as the electrolyte. A bipolar membrane (BPM, Fumasep FBM, Fuel Cell Store) was masked on the Ni foam for cation exchange while spacing out the KOH solution from the middle chamber between the AEM and the BPM. A phosphate-based minimal solution (typically, the Rhodococcus growth medium) flew through the middle chamber at a rate of 5 mL min^{-1} to elute the CO_2RR liquid products, while the salt composition in the solution provide conductivity for the whole electrolyzer. The solution was fixed to 20 mL and continuously circulated through the middle chamber to accumulate the liquid products.

Calculation of Faradaic efficiencies (FEs) from product concentration

For all liquid samples, the concentration of soluble CO_2RR products was measured by ^1H NMR using D_2O as the solvent and DMSO as the internal standard. The FEs of a specific product are calculated from its concentration using the following equation[25]:

$$FE = \frac{c \times n \times V \times F}{J \times t}$$

In this equation, c represents the concentration of a specific product, and n represents the number of electrons that one product molecule gets from CO_2 electroreduction. V is the solution volume. F is Faradaic efficiency, which is 96485 C/mol. J is the total current, while t represents the reaction time.

Calculation of energy efficiency for the Electro-biodiesel system

To calculate the energy efficiency from sunlight to final products, we analyzed the whole process and divided it into three stages, which are solar to electricity via photovoltaic technology (stage 1), electricity to CO_2RR liquid products (stage 2), and CO_2RR liquid products to lipid (stage 3) as depicted in Figure 6E.

For stage 1, the energy conversion efficiency of the photovoltaic panel available from the market was approximately 25.0%. This efficiency value was utilized to estimate the overall efficiency of stage 1 in our system.[21] For the energy efficiency of stage 2, we employed the approach introduced by Liu et al., wherein the energy content of the liquid products (energy output) was divided by the total energy input required to produce these liquid products (formate, ethanol, acetate, and propanol)[44] , which were subsequently used for lipid production in the WT and fads strains. The calculation can be expressed as follows:

$$EE = \frac{\Delta \times \times}{\sum(\times)\times \times \times} = \sum EE$$

Where the ΔH (kJ mol^{-1}) is the combustion heat of each liquid product, R (M/s) indicates the production rate of each liquid product, t (s) is the specific amount of time of the CO_2RR, n is number of electron of each liquid product, F is Faradaic coefficient, which is 96,485 C mol^{-1}, The applied voltage equated 2.6 V when using Cu catalyst and 3.6 V when using Cu_6Zn_1 catalyst, which was derived from the average cell voltage after iR compensation and then converted to the values relative to the reversible hydrogen electrode (RHE). The resistances (R) were determined by Electrochemical impedance spectroscopy (EIS) in the frequency ranging from 10^5 to 10^{-1} Hz and the amplitude was set at 10 mV.[43]

In the electrocatalysis step (with the Cu_6Zn_1 catalyst as example), the production rate of each liquid product (R), number of electrons used (n), and their combustion heats (ΔH), and calculated energy efficiency (EE) are listed as follows:

Product	R (mM/L/h)	n	ΔH (kJ mol^{-1})	EE (%)
Formate	14.8±0.8	2	-254.6	5.2±0.5%
Ethanol	17.0±1.1	12	-1367.6	32.5±4.1%
Acetate	8.00±0.10	8	-875.1	9.8±0.6%
Propanol	0.60±0.10	18	-2021.3	1.7±0.4%

Therefore, the energy conversion efficiency of electricity to liquid products were:

EE = 49.2%

This calculation is adopted because it excludes the energy consumption at the anode and internal resistance within the electrochemical system, making it more suitable for comparison with natural photosynthesis-driven compound synthesis processes. By considering the total electric energy consumption of the entire cell, rather than focusing solely on the energy used to produce liquid products, the energy efficiency of the whole electrochemical system for liquid products is[44]:

$$EE = \frac{\sum(\Delta H \times R) \times volume \times t}{Current \times Whole\ cell\ voltage \times t}$$

Where the R (mmol/L/h) is the production rate of each liquid product in electrolyte solution with $volume$ of 20 mL. The current applied is 500 mA, and the whole cell voltage is 6.5 V when using Cu_6Zn_1 catalyst. The energy efficiency of the whole CO_2RR catalysis cell is:

$$EE = 21.7\%$$

For stage 3, CO_2RR liquid products were used as the carbon source for the RHA1 strains to produce lipid. The fads strain was used as an example for calculation here. The energy efficiency was calculated as:

$$EE = \frac{\text{Energy content}}{\text{Energy content}}$$

To accurately evaluate the Energy content during the lipid fermentation process, we assume the R is stable during the CO_2RR process to calculate the $Amount$ from CO_2RR, and we monitored the concentration of liquid products at the starting and end points of the fermentation to calculate the amount of unconsumed products (Product). Therefore, the Energy content is calculated as follows:

$$\text{Energy content} = \sum((\text{R} \times \text{t} \times \text{volume} - \text{Product}) \times (1 - \text{volatility rate}) \times \Delta\text{H}) + \text{C2} \times (1 - \text{volatility rate}) \times \Delta\text{H} = \text{Product} \times \Delta\text{H}$$

Where the R (mM/L/h) indicates the production rate of each liquid product, which is measured and calculated based in volume of 20 mL. The t is the CO_2RR process performed in the integrated system, which are 15 hours. The volatility rate of ethanol and propanol was measured to be 10.2% under conditions of 30 ℃ and 200 rpm shaking, while acetate and formate showed negligible volatility. The ΔH (kJ mol^1) is the combustion heat of each liquid product. The C2 represents the externally added C2 carbon sources, which are 0.75 mmol ethanol and acetate, respectively. The ΔH indicate the combustion heats of ethanol and acetate. The amount of unconsumed products (Product), production rate of each liquid product (R), and their combustion heats (ΔH) are listed as follows:

Product	R (mM/L/h)	Product (mmol)	Product (mmol)	ΔH (kJ mol^{-1})
Formate	14.8±0.8	1.35±0.70	3.07±0.70	-254.6
Ethanol	17.0±1.1	1.51±0.28	3.89±0.25	-1367.6
Acetate	8.00±0.10	1.67±0.19	1.48±0.19	-875.1
Propanol	0.60±0.10	0.075±0.025	0.096±0.022	-2021.3

Therefore,

$$\text{Energy content} = 7.59\ kJ$$

The $Energy\ content$ can be calculated as follows:

$$\text{Energy content} = \text{Titer} \times \text{volume} \times \Delta\text{H} = 2.77\ kJ$$

where the Titer (mg/L)is the averaged lipid titer produced by the fads strain in the electro-biodiesel system, equals to 1840.2±3.3 mg/L (Figure 6C), the is the volume is fads culture volume to lipid production in the electro-biodiesel system, which is 40 mL, the ΔH (kJ/g) the combustion heat of microbial lipids, which is 37.6 kJ/g.[45]

Therefore,

$$EE = \frac{\text{Energy content}}{\text{Energy content}} \times 100\% = 36.5 \pm 1.5\%$$

Therefore, the overall solar-to-lipid energy efficiency (Figure 6E) is:

$$EE = 25\% \times 49.2\% \times 36.5\% = 4.5\%$$

For stage 4, microbial lipids are methylated to produce FAME, the final biodiesel product.

The energy content of the final product is referenced to microalgae FAME, which has a calorific value of up to 39.2 MJ/kg.[46] The energy content of microbial lipids is about 37.6 MJ/kg.[45] Methanol, required for the methyl esterification process, has an energy content of about 22.7 MJ/kg. Considering that complete transesterification of one mole of triglycerides (e.g. TG C16:0/C16:1/C18:0, molecular weight 832 g/mol) consume three moles of methanol, generates one mole of glycerol and three moles of FAME (FAME C17, FAME C17, and FAME C19), then transesterification of 1 kg of lipid will consume about 0.12 kg methanol and generate about 1kg FAME, thus,

$$EE = \frac{\text{Energy content of FAME}}{\text{Energy content of lipid and methanol}} \times \text{Yield} = 96.0 \pm 0.2\%$$

where the Yield is experimentally determined from the transesterification process of palmitic acid (C16), which is the major component of fatty acid in the lipid obtained from RHA1 cells.
Specifically, the input C16 for methyl esterification obtained FAME and the yield of transesterification are as follows:

Sample number	Input C16 (mg)	Theoretical FAME obtains (mg)	Obtained FAME (mg)	$\text{Yield}_{\text{transesterification}}$
1	105.0	110.7	109.1	98.5%
2	107.9	113.8	112.4	98.8%
3	102.6	108.2	107.2	99.1%

Overall,

$$\text{EE}_{\text{Solar to electro-biodiesel}} = \text{EE}_{\text{Solar to lipid}} \times \text{EE}_{\text{transesterification}} = 4.3\%$$

SUPPLEMENTAL REFERENCES

1 Xiao, Y., Ruan, Z., Liu, Z., Wu, S. G., Varman, A. M., Liu, Y. and Tang, Y. J. (2013). Engineering Escherichia coli to convert acetic acid to free fatty acids. Biochem. Eng. J. 76, 60-69.

2 Pang, Z., Chong, J., Zhou, G., de Lima Morais, D. A., Chang, L., Barrette, M., Gauthier, C., Jacques, P.-É., Li, S. and Xia, J. (2021). MetaboAnalyst 5.0: narrowing the gap between raw spectra and functional insights. Nucleic Acids Res. 49, W388-W396.

3 SRI International. Pathway Collages. https://metacyc.org/pathway-collage-info.

4 Statista. Biodiesel consumption worldwide from 2004 to 2023, with a forecast until 2030. https://www.statista.com/statistics/1440983/worldwide-consumption-ofbiodiesel/#:~:text=In%202023%2C%20worldwide%20biodiesel%20consumption,million%20metric%20tons%20in%202030.

5 Arkin, A. P., Cottingham, R. W., Henry, C. S., Harris, N. L., Stevens, R. L., Maslov, S., Dehal, P., Ware, D., Perez, F., Canon, S., Sneddon, M. W., Henderson, M. L., Riehl, W. J., Murphy-Olson, D., Chan, S. Y., Kamimura, R. T., Kumari, S., Drake, M. M., Brettin, T. S., Glass, E. M., Chivian, D., Gunter, D., Weston, D. J., Allen, B. H., Baumohl, J., Best, A. A., Bowen, B., Brenner, S. E., Bun, C. C., Chandonia, J.-M., Chia, J.-M., Colasanti, R., Conrad, N., Davis, J. J., Davison, B. H., DeJongh, M., Devoid, S., Dietrich, E., Dubchak, I., Edirisinghe, J. N., Fang, G., Faria, J. P., Frybarger, P. M., Gerlach, W., Gerstein, M., Greiner, A., Gurtowski, J., Haun, H. L., He, F., Jain, R., Joachimiak, M. P., Keegan, K. P., Kondo, S., Kumar, V., Land, M. L., Meyer, F., Mills, M., Novichkov, P. S., Oh, T., Olsen, G. J., Olson, R., Parrello, B., Pasternak, S., Pearson, E., Poon, S. S., Price, G. A., Ramakrishnan, S., Ranjan, P., Ronald, P. C., Schatz, M. C., Seaver, S. M. D., Shukla, M., Sutormin, R. A., Syed, M. H., Thomason, J., Tintle, N. L., Wang, D., Xia, F., Yoo, H., Yoo, S. and Yu, D. (2018). KBase: The United States Department of Energy Systems Biology Knowledgebase. Nat. Biotechnol. 36, 566-569.

6 CarbonCloud. Potassium phosphate E340. https://apps.carboncloud.com/climatehub/productreports/id/71624889280.
7 CarbonCloud. Limestone (CaCO3). https://apps.carboncloud.com/climatehub/productreports/id/43838269287.
8 Winnipeg. Emission factors in kg CO_2-equivalent per unit. https://legacy.winnipeg.ca/finance/findata/matmgt/documents/2012/682-2012/682-2012_appendix_h-wstp_south_end_plant_process_selection_report/appendix%207.pdf.
9 Center for Transportation Research Energy Systems Division. Argonne GREET Model. https://greet.anl.gov/.
10 Vea, E. B., Fabbri, S., Spierling, S. and Owsianiak, M. (2021). Inclusion of multiple climate tipping as a new impact category in life cycle assessment of polyhydroxyalkanoate (PHA)-based plastics. Sci. Total Environ. 788, 147544.
11 Intergovernmental Panel on Climate Change. CLIMATE CHANGE 2023 Synthesis Report. https://www.ipcc.ch/report/ar6/syr/downloads/report/IPCC_AR6_SYR_SPM.pdf.
12 Xu, H., Ou, L., Li, Y., Hawkins, T. R. and Wang, M. (2022). Life Cycle Greenhouse Gas Emissions of Biodiesel and Renewable Diesel Production in the United States. Environ. Sci. Technol. 56, 7512-7521.
13 Saranya, G. and Ramachandra, T. V. (2020). Life cycle assessment of biodiesel from estuarine microalgae. Energy Convers. Manag.: X 8, 100065.
14 Parsons, S., Allen, M. J., Abeln, F., McManus, M. and Chuck, C. J. (2019). Sustainability and life cycle assessment (LCA) of macroalgae-derived single cell oils. J. Clean. Prod. 232, 1272-1281.
15 DeLorenzo, D. M., Rottinghaus, A. G., Henson, W. R. and Moon, T. S. (2018). Molecular Toolkit for Gene Expression Control and Genome Modification in Rhodococcus opacus PD630. ACS Synth. Biol. 7, 727-738.
16 Xie, S., Sun, S., Lin, F., Li, M., Pu, Y., Cheng, Y., Xu, B., Liu, Z., da Costa Sousa, L., Dale, B. E., Ragauskas, A. J., Dai, S. Y. and Yuan, J. S. (2019). Mechanism-Guided Design of Highly Efficient Protein Secretion and Lipid Conversion for Biomanufacturing and Biorefining. Adv. Sci. (Weinh) 6, 1801980.
17 Soundararajan, M., von Bunau, R. and Oelschlaeger, T. A. (2019). K5 Capsule and Lipopolysaccharide Are Important in Resistance to T4 Phage Attack in Probiotic E. coli Strain Nissle 1917. Front. Microbiol. 10, 2783.
18 McLeod, M. P., Warren, R. L., Hsiao, W. W. L., Araki, N., Myhre, M., Fernandes, C., Miyazawa, D., Wong, W., Lillquist, A. L., Wang, D., Dosanjh, M., Hara, H., Petrescu, A., Morin, R. D., Yang, G., Stott, J. M., Schein, J. E., Shin, H., Smailus, D., Siddiqui, A. S., Marra, M. A., Jones, S. J. M., Holt, R., Brinkman, F. S. L., Miyauchi, K., Fukuda, M., Davies, J. E., Mohn, W. W. and Eltis, L. D. (2006). The complete genome of Rhodococcus sp. RHA1 provides insights into a catabolic powerhouse. Proc. Natl. Acad. Sci. USA 103, 15582-15587.
19 Ooms, M. D., Dinh, C. T., Sargent, E. H. and Sinton, D. (2016). Photon management for augmented photosynthesis. Nat. Commun. 7, 12699.
20 Blankenship, R. E., Tiede, D. M., Barber, J., Brudvig, G. W., Fleming, G., Ghirardi, M., Gunner, M. R., Junge, W., Kramer, D. M., Melis, A., Moore, T. A., Moser, C. C., Nocera, D. G., Nozik, A. J., Ort, D. R., Parson, W. W., Prince, R. C. and Sayre, R. T. (2011). Comparing Photosynthetic and Photovoltaic Efficiencies and Recognizing the Potential for Improvement. Science 332, 805809.
21 Ahmad, L., Khordehgah, N., Malinauskaite, J. and Jouhara, H. (2020). Recent advances and applications of solar photovoltaics and thermal technologies. Energy 207.
22 Zhang, G., Wang, T., Zhang, M., Li, L., Cheng, D., Zhen, S., Wang, Y., Qin, J., Zhao, Z.-J. and Gong, J. (2022). Selective CO_2 electroreduction to methanol via enhanced oxygen bonding. Nat. Commun. 13, 7768.
23 Obasanjo, C. A., Gao, G., Crane, J., Golovanova, V., García de Arquer, F. P. and Dinh, C.-T. (2023). High-rate and selective conversion of CO_2 from aqueous solutions to hydrocarbons. Nat. Commun. 14, 3176.
24 Wang, P., Yang, H., Tang, C., Wu, Y., Zheng, Y., Cheng, T., Davey, K., Huang, X. and Qiao, S.Z. (2022). Boosting electrocatalytic CO_2–to–ethanol production via asymmetric C–C coupling. Nat. Commun. 13, 3754.
25 Hann, E. C., Overa, S., Harland-Dunaway, M., Narvaez, A. F., Le, D. N., Orozco-Cárdenas, M. L., Jiao, F. and Jinkerson, R. E. (2022). A hybrid inorganic–biological artificial photosynthesis system for energy-efficient food production. Nat. Food 3, 461-471.
26 Claassens, N. J., Cotton, C. A. R., Kopljar, D. and Bar-Even, A. (2019). Making quantitative sense of electromicrobial production. Nat. Catal. 2, 437-447.

27 U.S. Energy Information Administration. SHORT-TERM ENERGY OUTLOOK. https://www.eia.gov/outlooks/steo/report/BTL/2023/06-dieselmacro/article.php.
28 National Renewable Energy Laboratory. How much land will PV need to supply our electricity? https://www.nrel.gov/docs/fy04osti/35097.pdf.
29 National Renewable Energy Laboratory. The Potential for Biofuels from Algae. https://www.nrel.gov/docs/fy08osti/42414.pdf.
30 United States Department of Agriculture. Crop Production 2023 Summary. https://downloads.usda.library.cornell.edu/usdaesmis/files/k3569432s/ns065v292/8910md644/cropan24.pdf. 31 USDA Foreign Agricultural Service. Production - Palm Oil. https://fas.usda.gov/data/production/commodity/4243000
32 Our World in Data. Palm Oil. https://ourworldindata.org/palm-oil.
33 USDA Agricultural Service. (2023). Biofuels Annual. chromeextension://efaidnbmnnnibpcajpcglclefindmkaj/https://apps.fas.usda.gov/newgainapi/api/Report/DownloadReportByFileName?fileName=Biofuels%20Annual_Kuala%20Lumpur_Malaysia_MY202 3-0012.pdf
34 Alvarez, H. M., Herrero, O. M., Silva, R. A., Hernandez, M. A., Lanfranconi, M. P. and Villalba, M. S. (2019). Insights into the Metabolism of Oleaginous Rhodococcus spp. . Appl. Environ. Microbiol. 85, e00498-00419.
35 Niemann, B., Haufs-Brusberg, S., Puetz, L., Feickert, M., Jaeckstein, M. Y., Hoffmann, A., Zurkovic, J., Heine, M., Trautmann, E.-M., Müller, C. E., Tönjes, A., Schlein, C., Jafari, A., Eltzschig, H. K., Gnad, T., Blüher, M., Krahmer, N., Kovacs, P., Heeren, J. and Pfeifer, A. (2022). Apoptotic brown adipocytes enhance energy expenditure via extracellular inosine. Nature 609, 361-368.
36 Wang, X., Liu, W., Xin, C., Zheng, Y., Cheng, Y., Sun, S., Li, R., Zhu, X.-G., Dai, S. Y., Rentzepis, P. M. and Yuan, J. S. (2016). Enhanced limonene production in cyanobacteria reveals photosynthesis limitations. Proc. Natl. Acad. Sci. USA113, 14225-14230.
37 Fiehn, O. and Kind, T. in Metabolomics: Methods and Protocols (ed Wolfram Weckwerth) 3-17 (Humana Press, 2007).
38 Fiehn, O., Wohlgemuth, G., Scholz, M., Kind, T., Lee, D. Y., Lu, Y., Moon, S. and Nikolau, B. (2008). Quality control for plant metabolomics: reporting MSI-compliant studies. Plant J. 53, 691704.
39 Matyash, V., Liebisch, G., Kurzchalia, T. V., Shevchenko, A. and Schwudke, D. (2008). Lipid extraction by methyl-tert-butyl ether for high-throughput lipidomics. J Lipid Res. 49, 1137-1146.
40 Tsugawa, H., Cajka, T., Kind, T., Ma, Y., Higgins, B., Ikeda, K., Kanazawa, M., VanderGheynst, J., Fiehn, O. and Arita, M. (2015). MS-DIAL: data-independent MS/MS deconvolution for comprehensive metabolome analysis. Nat. Methods 12, 523-526.
41 DeFelice, B. C., Mehta, S. S., Samra, S., Čajka, T., Wancewicz, B., Fahrmann, J. F. and Fiehn, O. (2017). Mass Spectral Feature List Optimizer (MS-FLO): A Tool To Minimize False Positive Peak Reports in Untargeted Liquid Chromatography–Mass Spectroscopy (LC-MS) Data Processing. Anal. Chem. 89, 3250-3255.
42 Kind, T., Liu, K.-H., Lee, D. Y., DeFelice, B., Meissen, J. K. and Fiehn, O. (2013). LipidBlast in silico tandem mass spectrometry database for lipid identification. Nat. Methods 10, 755-758.
43 Zhang, P., Chen, K., Xu, B., Li, J., Hu, C., Yuan, J. S. and Dai, S. Y. (2022). Chem-Bio interface design for rapid conversion of CO_2 to bioplastics in an integrated system. Chem 8, 3363-3381.
44 Liu, C., Colón, B. C., Ziesack, M., Silver, P. A. and Nocera, D. G. (2016). Water splitting– biosynthetic system with CO_2 reduction efficiencies exceeding photosynthesis. Science 352, 1210-1213.
45 Khoo, K. S., Ahmad, I., Chew, K. W., Iwamoto, K., Bhatnagar, A. and Show, P. L. (2023). Enhanced microalgal lipid production for biofuel using different strategies including genetic modification of microalgae: A review. Progress in Energy and Combustion Science 96, 101071.
46 Hossain, F. M., Rainey, T. J., Ristovski, Z. and Brown, R. J. (2018). Performance and exhaust emissions of diesel engines using microalgae FAME and the prospects for microalgae HTL biocrude. Renew. Sustain. Energy Rev. 82, 4269-4278.